university of groningen
faculty of science and engineering
industrial engineering and management

Passivity-based trajectory tracking of the Philips Experimental Robot Arm

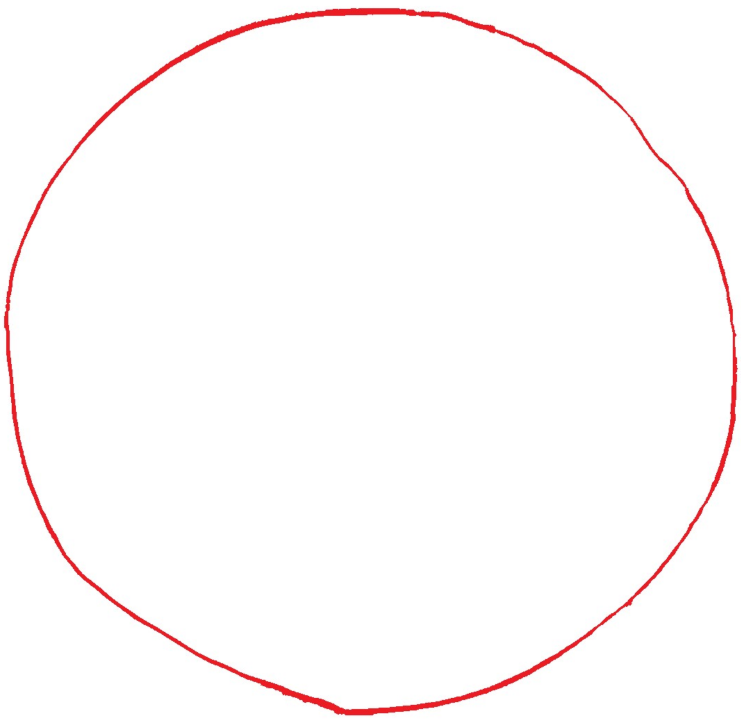

Master's thesis Industrial Engineering and Management

March 13, 2020

Author: BSc. J.L. van der Veen

First supervisor: Prof. Dr. Ir. J.M.A. Scherpen

Daily supervisor: Dr. L.P. Borja Rosales

Second assessor: Dr. M. Muñoz-Arias

Abstract

In this work, a method for trajectory tracking of robotic arms is designed and implemented on the Philips Experimental Robot Arm, a robotic arm intended for research applications. To demonstrate the method, several experiments are conducted, where the arm is led to draw a desired shape on a canvas. To this end, a passivity-based control law for trajectory tracking of fully actuated mechanical systems is proposed. The system is modeled in the port-Hamiltonian framework for mechanical systems. The closed-loop system is proven to be globally asymptotically stable by Lyapunov's second method and La Salle's invariance principle. The proposed control strategy is naturally saturated and requires only position measurements, omitting the need for velocity measurements by extension of the system. This control law is compared against a non-saturated equivalent to show differences in performance.

For the task of drawing, three degrees of freedom are required to let the end-effector of the arm follow the desired path. To deal with sensor offsets and position errors, a force-based drawing enhancement heuristic approach is proposed. This heuristic approach enables a successful drawing application for the PERA. An additional two degrees of freedom in the wrist are considered to control the orientation of the end effector. The implementation of these joints is successful, but at the cost of the performance of the heuristic approach.

Acknowledgements

Most of all, I want to express my gratitude to my daily supervisor Dr. Pablo Borja for his guidance throughout my thesis. His availability for questions and willingness to help me with any issues that arose, have been of incredible value during my project.

Moreover, I want to thank my first supervisor Prof. Dr. Ir. Jacquelien Scherpen, for giving me the opportunity to work on this project and for the help and ideas she provided during our meetings.

In addition, I want to thank my second assessor Dr. Mauricio Muñoz Arias, for his involvement in the project and his willingness to share his knowledge with me.

Furthermore, I want to thank Martin Stokroos and Simon Busman, who have provided me with whatever technical support which was needed, and Sietse Achterop, for his help with and knowledge of the programming of the PERA.

Many thanks go to Floris van den Bos, for introducing me to the PERA and sharing his findings with me, and to Dr. Daniel Dirksz, for his interest in my project and his help with the design of trajectories during his short visit to the university.

Finally, I want to express my thankfulness to my friends and family, for being supportive and interested throughout my project.

Contents

List of Figures

List of Tables

Notation

Mathematical notation

$\mathbb{R}$	Field of real numbers.
$\mathbb{R}_+$	Field of nonnegative real numbers
$\mathbb{R}^n$	n-dimensional Euclidean space
$\mathbb{R}^{n\times m}$	The set of all $n \times m$-dimensional matrices with all real elements
x_i	The i-th element of the vector $x \in \mathbb{R}^n$
$\mathbf{0}_n$	Column vector of dimension n with all elements equal to zero.
$\mathbf{0}_{n\times m}$	Matrix of dimension $n \times m$ with all elements equal to zero.
x_0	Initial condition for the element $x(t)$, such that $x_0 := x(t_0)$
I_n	The identity matrix of dimension $n \times n$.
$(\cdot)^{-1}$	Matrix inverse operator.
$(\cdot)^\top$	Matrix transpose operator.
$(\cdot)^{-\top}$	Operator denoting the transpose of the inverse of a matrix or vice versa, i.e. $(\cdot)^{-\top} = ((\cdot)^\top)^{-1} = ((\cdot)^{-1})^\top$.
e_i	The i-th Euclidean basis vector.
A_i	The i-th column of matrix A.
A_{ij}	The ij-th element of matrix A.
$\max\{x\}$	The maximum value attained by the parameter x.
$\mathrm{diag}\{\cdot\}$	Diagonal matrix of the input arguments.
$\mathrm{mean}\{\cdot\}$	The mean value of a parameter.
$\mathrm{argmin}\{\cdot\}$	The argument of the minimum of a function.
$F(x)$	A function $F : \mathbb{R}^n \to \mathbb{R}^s$ of the arguments $x \in \mathbb{R}^n$.
F_*	The function $F(x) : \mathbb{R}^n \to \mathbb{R}^s$ evaluated at $x = x^*$, i.e. $F_* := F(x_*)$.
$\nabla F(x)$	The gradient operator of a function $F : \mathbb{R}^n \to \mathbb{R}$, i.e. $\nabla F(x) := \left(\frac{\partial F(x)}{\partial x}\right)^\top$.
$\nabla^2 F(x)$	The Hessian operator of a function $F : \mathbb{R}^n \to \mathbb{R}$, i.e. $\nabla^2 F(x) := \left(\frac{\partial^2 F(x)}{\partial x^2}\right)$.
$C^1(\Omega, \mathbb{R})$	Class containing all functions $\Omega \to \mathbb{R}$ which are continuously differentiable on Ω.
$[f, g](x)$	The Lie bracket of $f(x)$ and $g(x)$, i.e. $[f, g](x) := \frac{\partial g}{\partial x}(x)f(x) - \frac{\partial f}{\partial x}(x)g(x)$.

All vectors are column vectors, unless indicated otherwise. For reasons of clarity and space constraints, arguments of functions and mappings are sometimes omitted.

Acronyms

AS	Asymptotically Stable
CoM	Center Of Mass
DH	Denavit-Hartenberg
DoF	Degrees Of Freedom
GAS	Globally Asymptotically Stable
PBC	Passivity-Based Control
PERA	Philips Experimental Robot Arm
pH	Port-Hamiltonian
PD	Proportional and Derivative
PID	Proportional-Integral-Derivative
PLvCC	Partial Linearization via Coordinate Changes
RoM	Range Of Motion
SMA	Simple Moving Average
SPR	Set Point Regulation

Chapter 1

Introduction

In the last few decades, robots have become an important part of modern day industry and society. Initially developed for the production industry, scientific research has allowed the applications of robotics to diverge. Therefore, applications in for example healthcare, home automation (domotics), and military operations, are becoming increasingly common (Harmo et al., 2005; Lin, Bekey, and Abney, 2008; Okamura, Mataric, and Christensen, 2010). Due to the widening of the application fields of robotics, the required operations are becoming more and more complex. Therefore, there is a great interest in the development of robust, high precision controllers to regulate the actuation of robotic joints.

In this work, the focus is on the design and implementation of a control law for the Philips Experimental Robot Arm (PERA). This is a robotic arm, developed by Philips Applied Technologies, which closely resembles the functions of a human arm (Rijs et al., 2014). The aim of the project is to design a control law, such that the end-effector follows a desired trajectory. To demonstrate this, we aim to let the PERA draw on a canvas. In the project, several implementation issues are addressed, like the absence of velocity sensors in the PERA, the saturation of the joint motors and errors in sensor measurements and canvas placement.

The port-Hamiltonian (pH) framework is used to model the PERA, and a passivity-based control (PBC) approach is adopted to successfully achieve trajectory tracking. In this chapter, the mechanical system under study is introduced. Then, an introduction to the pH framework for modeling of mechanical systems is provided. Moreover, the scope of this project is presented, along with the further outline of the thesis.

1.1 The PERA

The PERA is a fully actuated robotic arm with seven degrees of freedom (DoF). The system has been developed for research purposes by Philips Applied Technologies (Rijs et al., 2014), where the main objective is to mimic the motion of a human arm. The arm consists of a shoulder, elbow, wrist and gripper, and is equipped with force and position sensors in each joint, which can be used for control purposes. In the past decade, the PERA in the University of Groningen has been the subject of a large number of studies (Mendels, 2011; Bögel, 2012; Bol, 2012; de Jong, 2013; Siemonsma, 2014; Koops, 2014; Leeuwerik, 2015; Muñoz-Arias, 2015; van den Bos, 2019). In particular, this work continues the line of research studied in van den Bos (2019), where the main goal was to achieve set point regulation (SPR). Due to the lines of research, the structure of this thesis somewhat similar to that of the work mentioned, especially in the preliminaries, experimental setup and control design (Chapters 2-4).

This thesis deals with two limitations of the PERA, i.e. the absence of velocity sensors and the saturation limits on the current sent to the motors, which are needed to prevent damage on the DC motors. Hence, following the ideas exposed in van den Bos (2019), this thesis aims to design a control law for the PERA, which is saturated and does not require velocity measurements. A detailed description of the PERA is given in Chapter 3.

1.2 Port-Hamiltonian framework for mechanical systems

To design a control law for mechanical systems like the PERA, the first step is to derive an analytical model of the system. For the modeling of mechanical systems, several approaches exist (van der Schaft, 2004). In this thesis, the system of the PERA is modeled in the pH framework, first mentioned in (Maschke and van der Schaft, 1992). In this framework, the total energy of the system is modeled in the Hamiltonian function, which is based on the law of conservation of energy (Serway and Jewett, 2018). By use of the Hamiltonian function, a dynamical model of the mechanical system can be constructed.

The energy-based setting of the pH framework allows for passivity-based control of the system. In passive systems, the emphasis is on the energy exchange of the system with the environment (Ortega et al., 2013). The property of passivity of a system implies that the system cannot produce any energy by itself. Therefore, the energy supplied to a passive system is greater than the energy that is stored. The difference in energy is dissipated from the system. In this work, the property of passivity is used to stabilize the system on he desired trajectories.

Using the pH approach has several advantages compared to other approaches, such as the classical Lagrangian, Newtonian and Euler-Lagrange approaches. These advantages are listed below.

- The framework has a clear physical interpretation (Duindam et al., 2009).
- Interconnections and dissipation of energy can be clearly identified (Duindam et al., 2009).
- Most pH systems are passive (also the PERA), allowing PBC (van der Schaft, 2000).
- The Hamiltonian can be taken as a candidate Lyapunov function, which allows stability analysis by Lyapunov's direct method (van der Schaft, 2000).
- The pH framework allows extension of the dynamics of the mechanical system (van der Schaft, 2000; Duindam et al., 2009).

In recent years, PBC of pH systems has been used to propose saturated control laws for mechanical systems which do not require velocity measurements (Dirksz, Scherpen, and Ortega, 2008; Wesselink, 2018; Wesselink, Borja, and Scherpen, 2018; Veltman, 2019; van den Bos, 2019). This thesis will continue this line of work by applying new control laws for trajectory tracking of the PERA.

1.3 Scope

The main goal of this work is to develop a drawing routine for the PERA. The PERA is commanded to let the gripper follow a desired trajectory on a canvas, such that the marker attached to the gripper of the PERA draws the desired shape. In the experiments, the first basic shape attempted to draw is a circle.

To attain the goal of developing a drawing routine, a PBC strategy for trajectory tracking is proposed. The control law is saturated and does not require velocity measurements. Furthermore, the closed-loop system can be proven to be globally asymptotically stable by Lyapunov's second method and LaSalle's invariance principle. Since the concept of the control law is relatively new, the tuning of the controller gains is thoroughly investigated. To narrow the scope of this project, three DoF of the PERA are considered; shoulder pitch, shoulder yaw and elbow pitch. When the goal of trajectory tracking is attained, the drawing routine is enhanced by dealing with steady-state errors and sensor offsets. This enhancement is achieved by adapting the desired trajectory of the shoulder pitch joint, such that a constant force is exerted on the canvas. The adaption of the desired joint trajectory is based on the measurements of the force sensors in the wrist of the PERA. Moreover, the wrist pitch and yaw are included in the system, to control the orientation of the end effector with respect to the canvas.

1.4 Outline of the thesis

This thesis is structured as follows.

- In Chapter 2 the theoretical background for the scientific contributions in this work are presented. The concepts of stability and passivity are discussed, and the pH framework is discussed, along with its properties. Moreover, the modeling of the PERA is discussed.
- Chapter 3 discusses the experimental setup of the PERA. The model of the inertia matrix and potential energy of the mechanical system is presented and further information on the PERA is provided.
- The contents of Chapter 4 are devoted to the control design. The dynamics of the system as presented in the pH framework are given and a canonical transformation is applied in order to obtain an error system. The remainder of this chapter deals with the proposal of control strategies to stabilize the error system.
- The work of Chapter 5 is devoted to the results obtained in simulations and experiments. The desired trajectories are defined, and the control law proposed is thoroughly tested in simulations and experiments. The results are compared to those of another, non-saturated control law. Furthermore, a heuristic to enhance the quality of the drawings produced by the PERA is proposed and the orientation of the end-effector is considered.
- Finally, in Chapter 6, concluding remarks are presented. Moreover, several options for future research in the line of this work are suggested.

Chapter 2

Preliminaries

This chapter provides the required background for the contributions presented in this thesis. The preliminaries entail the established theoretical concepts and scientific principles that are used as a basis on which this work continues.

First, the concepts of stability and passivity are discussed. Then, the pH representation of mechanical systems is considered and linked to the concepts discussed earlier. Furthermore, PBC is discussed. Finally, the theory required for the mathematical modeling of n-DoF mechanical systems is provided.

2.1 Stability

In words, an equilibrium is stable if, when the initial states of the system are sufficiently close to the equilibrium, the states of the system remain in a certain region around the equilibrium (Aström and Murray, 2010). Different forms of stability exist, of which the most important ones are defined in this chapter. In this thesis, the focus is on stability in the sense of Lyapunov. Mathematical definitions of equilibria and stability, based on the definitions in Khalil (2002), van der Schaft (2000), and Aström and Murray (2010), are given in Definitions 2.1 and 2.2.

Consider a non-linear system of the form $f : \mathbb{R}^n \to \mathbb{R}^s$

$$\dot{x} = f\left(x(t, x_0)\right). \tag{2.1}$$

Definition 2.1 (**Equilibrium** (Khalil, 2002))**.** The point $x_* \in \mathbb{R}^n$ is an equilibrium of the system (2.1) if and only if $f_* = \mathbf{0}_n$.

Definition 2.2 (**Stability** (Khalil, 2002))**.** An equilibrium of a system of the form (2.1) is called

i. stable, if $\forall \varepsilon > 0 \quad \exists \delta > 0$ such that

$$\|x_0 - x_*\| < \delta \implies \|x\left(t, x_0\right) - x_*\| < \epsilon \quad \forall t \geq t_0. \tag{2.2}$$

ii. locally asymptotically stable (AS), if it is stable and $\exists \delta_1 > 0$ such that

$$\|x_0 - x_*\| < \delta_1 \implies \lim_{t \to \infty} x\left(t, x_0\right) = x_*. \tag{2.3}$$

iii. globally asymptotically stable (GAS), if it is stable and

$$\lim_{t \to \infty} x\left(t, x_0\right) = x_* \quad \forall x_0 \in \mathbb{R}^n. \tag{2.4}$$

iv. unstable, if it is not stable, i.e. $\exists \varepsilon > 0$ such that $\forall \delta > 0 \quad \exists x_0, t_1$ for which

$$\|x_0 - x_*\| < \delta \implies \|x\left(t, x_0\right) - x_*\| \geq \epsilon. \tag{2.5}$$

In the following subsections, Lyapunov's first and second method, as well as LaSalle's invariance principle are discussed. These tools can be used to prove (asymptotic) stability of non-linear systems.

2.1.1 Lyapunov's Second Method

Lyapunov's second method, also referred to as Lyapunov's direct method, was first presented by the Russian mathematician, mechanician and physicist Aleksandr Mikhailovich Lyapunov in 1892 (Lyapunov, 1992). The method utilizes the auxiliary function of the system $V(x)$, which is called the Lyapunov function, to prove stability of the system. Theorem 2.1 defines the method according to the definitions by van der Schaft (2000), Khalil (2002), and Aström and Murray (2010).

Theorem 2.1 (**Lyapunov's Second Method** (Khalil, 2002))**.** Consider a system of the form (2.1), with an equilibrium in x_*. If there is a neighborhood Ω of x_*, and a function $V(x) : \Omega \to \mathbb{R}$ such that on Ω

i. $V(x)$ is continuously differentiable, i.e. $V(x) \in C^1(\Omega, \mathbb{R})$,

ii. $V(x)$ is positive definite with respect to x_*, i.e. $V(x_*) = 0$ and $V(x) > 0, \quad \forall x \in \Omega \backslash x_*$,

iii. $\dot{V}(x)$ is negative semi-definite with respect to x_*, i.e. $\dot{V}(x) \leq 0 \quad \forall x \in \Omega$,

then $V(x)$ is a Lyapunov function and x_* is a stable equilibrium for (2.1). If in addition

iv. $\dot{V}(x)$ is negative definite relative to x_*, i.e. $\dot{V}(x) < 0 \quad \forall x \in \Omega \backslash x_*$,

then $V(x)$ is a strong Lyapunov function and x_* is a locally AS equilibrium for (2.1). If moreover

v. The neighborhood Ω is the set of real numbers, i.e. $\Omega = \mathbb{R}$,

vi. $V(x)$ is radially unbounded, i.e. $V(x) \to \infty$ as $\|x\| \to \infty$,

then the stability properties of system (2.1) are global.

Remark. The Lyapunov function is positive definite (condition ii of Theorem 2.1) if the gradient of the Lyapunov function evaluated at the equilibrium returns a zero vector and the Hessian of the Lyapunov function is positive definite, i.e.

$$\begin{aligned} [\nabla V]_* &= \mathbf{0}_n \\ \left[\nabla^2 V\right] &> 0. \end{aligned} \tag{2.6}$$

For a proof of Theorem 2.1, the reader is referred to (Khalil, 2002).

2.1.2 LaSalle's Invariance Principle

In many cases, Lyapunov's second method is sufficient to prove stability of the (closed-loop) non-linear system under study. Asymptotic stability, however, can be difficult to prove with Lyapunov's second method, as the time derivative of the Lyapunov function is not always negative definite with respect to the equilibrium (condition iv of Theorem 2.1). In this case, LaSalle's invariance principle can be used as a tool to prove asymptotic stability.

LaSalle's invariance principle, also known as the Krasovskii-Lasalle's invariance principle or Barbashin-Krasovskii-Lasalle's invariance principle (Hancock and Papachristodoulou, 2012), can be used to prove asymptotic stability of non-linear systems when Lyapunov's second method can only ensure stability (LaSalle, 1960; Krasovskii, 1963). The invariance principle is given in Theorem 2.2 after the definition of an invariant set is provided in Definition 2.3. The definition and theorem are based on the ones found in the work of van der Schaft (2000), Khalil (2002), and Aström and Murray (2010).

Definition 2.3 (**Positively invariant Set** (Khalil, 2002))**.** A set $\mathbb{S}$ is called an invariant set for system (2.1) if the states $x(t, x_0)$, with initial condition x_0 in $\mathbb{S}$, remain in $\mathbb{S}$ for all $t > 0$, i.e.

$$x_0 \in \mathbb{S} \implies x(t, x_0) \in \mathbb{S} \quad \forall t \geq 0. \tag{2.7}$$

In other words, if x starts in $\mathbb{S}$, it remains in $\mathbb{S}$ for all time.

Theorem 2.2 (**LaSalle's Invariance Principle** (Khalil, 2002))**.** Consider a system of the form (2.1) with equilibrium x_* and Lyapunov function $V(x)$, with $x \in \mathbb{R}^n$, on some neighborhood Ω of the equilibrium. This set Ω contains an positively invariant neighborhood $\mathbb{K}$ of x_*. For every initial condition $x_0 \in \mathbb{K}$, as $t \to \infty$ the states $x(t, x_0)$ converge to the positively invariant and nonempty subset

$$\mathbb{G} := \left\{ x_* \in \mathbb{K} \;\middle|\; \dot{V}(x) = 0 \quad \forall t \geq 0 \right\}. \tag{2.8}$$

In particular, if $\mathbb{G}$ contains no invariant sets other than $x = x_*$, then x_* is an AS equilibrium. If moreover $\mathbb{K} \equiv \mathbb{R}^n$, then x_* is a GAS equilibrium.

For the proof of Theorem 2.2, the reader is referred to the work of LaSalle (1960) and Krasovskii (1963).

2.1.3 Lyapunov's First Method

The so-called Lyapunov's first method, utilizes the linearization of the system around the equilibrium to prove stability of the equilibrium. The method is defined in Theorem 2.3.

Theorem 2.3 (**Lyapunov's First Method** (Khalil, 2002))**.** Consider a system of the form (2.1), with the equilibrium x_*. The linearization of the system around the equilibrium is given by

$$\dot{x} = A(x - x_*), \tag{2.9}$$

with

$$A = \frac{\partial f}{\partial x}(x_*). \tag{2.10}$$

Then,

i. If the real part of all eigenvalues is strictly negative, the equilibrium x_* is locally AS.

ii. If at least one eigenvalue has a positive real part, the equilibrium x_* is unstable.

iii. If the real part of at least one eigenvalue is equal to zero, while the real part of all other eigenvalues is strictly negative, no conclusion can be drawn about the stability of the equilibrium x_*.

For a proof of Theorem 2.3, the reader is referred to (Khalil, 2002).

2.2 Passive systems

The concept of passivity is defined in Definition 2.4. This definition is based on the formulations in van der Schaft (2000). For further elaboration on this subject the reader is referred to this work.

Consider a non-linear system of the form

$$\begin{aligned} \dot{x} &= f(x, u) \\ y &= h(x, u), \end{aligned} \tag{2.11}$$

with states $x = (x_1, \dots, x_n)^\top$, the system inputs $u \in U$ and the system outputs $y \in Y$. The linear spaces U and Y are assumed to be n-dimensional, i.e. the system is fully actuated.

Definition 2.4 (**Passivity** (van der Schaft, 2000))**.** Consider a system of the form (2.11). The supply rate of the system is defined as

$$s : U \times Y \to \mathbb{R}. \tag{2.12}$$

The system is said to be passive if there exists a storage function $S : \mathbb{R}^n \to \mathbb{R}_+$, such that for all $x_0 \in \mathbb{R}^n$, all $t_1 \geq t_0$ and all input functions $u(\cdot)$

$$S\left(x\left(t_1\right)\right) \leq S\left(x_0\right) + \int_{t_0}^{t_1} s(t) dt. \tag{2.13}$$

This inequality is called the dissipation inequality. For passive systems, the dissipation inequality can be rewritten as the power inequality

$$\dot{S}\left(x\left(t\right)\right) \leq u^\top y. \tag{2.14}$$

If the system is passive, y denotes the passive output of the system.

If (2.13) and (2.14) hold with equality for all x_0 and all $u(\cdot)$, the system (2.11) is conservative.

2.3 Port-Hamiltonian representation of mechanical systems

In this project, the pH framework is used for the mathematical modeling of the PERA (Maschke and van der Schaft, 1992). For mechanical systems, the states in the pH framework are given by the generalized positions $q \in \mathbb{R}^n$ and momenta $p \in \mathbb{R}^n$ of the system. The dynamics of a mechanical system in the pH framework are described by (van der Schaft, 2000)

$$\begin{aligned} \begin{bmatrix} \dot{q} \\ \dot{p} \end{bmatrix} &= \begin{bmatrix} \mathbf{0}_{n\times n} & I_{n\times n} \\ -I_{n\times n} & -D(q) \end{bmatrix} \begin{bmatrix} \frac{\partial H}{\partial q}(q,p) \\ \frac{\partial H}{\partial p}(q,p) \end{bmatrix} + \begin{bmatrix} \mathbf{0}_{n\times m} \\ G \end{bmatrix} u \\ y &= G^\top \frac{\partial H}{\partial p}(q,p), \end{aligned} \tag{2.15}$$

where $D(q) \in \mathbb{R}^{n\times n}$ is the damping matrix such that $D(q) = D(q)^\top \geq 0$, $G \in \mathbb{R}^{n\times m}$ is the full rank input matrix and $u, y \in \mathbb{R}^m$ with $m \leq n$ are the input and output vectors, respectively. The Hamiltonian function $H(q,p)$, which is equal to the total energy of the system, is given by

$$H(q,p) = \frac{1}{2} p^\top M^{-1}(q) p + V(q), \tag{2.16}$$

where $M(q) \in \mathbb{R}^{n\times n}$ the inertia matrix of the mechanical system and $V(q) \in \mathbb{R}$ the potential energy of the mechanical system.

Using (2.15) and (2.16), the system can be expressed as

$$\begin{aligned} \dot{q} &= p^\top M^{-1}(q) \\ \dot{p} &= -\tfrac{1}{2} \sum_{i=1}^{n} e_i p^\top \tfrac{\partial M^{-1}(q)}{\partial q_i} p - \tfrac{\partial V}{\partial q} + Gu \\ y &= G^\top \dot{q}. \end{aligned} \tag{2.17}$$

2.3.1 Passivity of port-Hamiltonian systems

The representation of a mechanical system in the pH framework can be used to prove passivity of the system, since the Hamiltonian equation is a natural storage function for the system. Due to the pH structure, the power inequality (2.14) is always satisfied. In particular, from the pH representation of mechanical systems (2.15), we have.

$$\begin{aligned}\dot{H} &= \left(\frac{\partial H}{\partial q}\right)^\top \dot{q} + \left(\frac{\partial H}{\partial p}\right)^\top \dot{p} \\ &= \left(\frac{\partial H}{\partial q}\right)^\top \frac{\partial H}{\partial p} + \left(\frac{\partial H}{\partial p}\right)^\top \left(-\frac{\partial H}{\partial q} - D\frac{\partial H}{\partial p} + Gu\right) \\ &= \underbrace{\left(\frac{\partial H}{\partial q}\right)^\top \frac{\partial H}{\partial p} - \left(\frac{\partial H}{\partial p}\right)^\top \frac{\partial H}{\partial q}}_{=0} - \underbrace{\left(\frac{\partial H}{\partial p}\right)^\top D\frac{\partial H}{\partial p}}_{>0} + \underbrace{\left(\frac{\partial H}{\partial p}\right)^\top G}_{=y^\top} u \\ &= -\left(\frac{\partial H}{\partial p}\right)^\top D\frac{\partial H}{\partial p} + y^\top u \leq y^\top u\end{aligned} \tag{2.18}$$

Thus, the pH system is passive with respect to the passive output y. In the case that the system's natural damping is ignored, we get

$$\dot{H} = y^\top u, \tag{2.19}$$

indicating that the system is conservative.

2.3.2 Partial linearization via coordinate changes

Canonical transforms can be applied to pH systems for different proposes, e.g., Fujimoto and Sugie (2001) and Viola et al. (2007). This section particularly focuses on the Partial Linearization via Coordinate Changes (PLvCC) as proposed in Venkatraman et al. (2010).

Define the matrix $\Psi \in \mathbb{R}^{n\times n}$ as the lower Cholesky factorization of $M^{-1}(q)$, i.e. (Dereniowski and Kubale, 2003),

$$M^{-1}(q) = \Psi(q)\Psi^\top(q). \tag{2.20}$$

Consider the new coordinate $\mathtt{P} = \Psi^\top(q)p$. Then, from (2.15) it follows that

$$\begin{aligned}\begin{bmatrix}\dot{q}\\ \dot{\mathtt{P}}\end{bmatrix} &= \begin{bmatrix}\mathbf{0}_{n\times n} & \Psi(q)\\ -\Psi^\top(q) & J(q,p)-D(q)\end{bmatrix}\begin{bmatrix}\frac{\partial \bar{H}}{\partial q}(q,\mathtt{P})\\ \frac{\partial \bar{H}}{\partial \mathtt{P}}(q,\mathtt{P})\end{bmatrix} + \begin{bmatrix}\mathbf{0}_{n\times n}\\ \Psi^\top(q)G\end{bmatrix}u \\ y &= G^\top\Psi(q)\frac{\partial \bar{H}}{\partial \mathtt{P}}(q,\mathtt{P}) = G^\top\dot{q},\end{aligned} \tag{2.21}$$

with the Hamiltonian

$$\bar{H}(q,\mathtt{P}) = \frac{1}{2}\mathtt{P}^\top\mathtt{P} + V(q), \tag{2.22}$$

where $J(q,p) \in \mathbb{R}^{n\times n}$ is a skew-symmetric matrix representing the gyroscopic forces in the system (Romero, Ortega, and Sarras, 2014). The elements of this matrix are defined as

$$J_{ij}(q,p) = -p^\top\left[\Psi_i, \Psi_j\right]. \tag{2.23}$$

In Venkatraman et al. (2010), several conditions ensuring $J = \mathbf{0}_{n\times n}$ are provided.

2.4 Passivity-Based Control

The principle of passivity allows the design of control laws through the method of PBC, first introduced by Ortega and Spong (1989). The main principle of PBC, is to define the input such that the closed-loop system is rendered passive with respect to a desired storage function which has a minimum in the desired equilibrium (Ortega et al., 2013). As a result, the equilibrium can be proven to be stable.

There are two main approaches for PBC. In the "classical" approach, the desired storage function is defined beforehand, with a minimum at the desired equilibrium. In this thesis, the desired storage function is equal to the desired Hamiltonian function. Then, the controller is designed, such that the closed-loop system is passive and Lyapunov's second method can be used to prove stability of the system. This process is referred to as energy shaping. In classical PBC, damping is often injected to ensure AS. In the second PBC approach, the desired structure of the closed-loop system is selected, after which the possible energy functions are considered (Ortega et al., 2002). To this end, a control law of the form

$$\tilde{u} = k(x) + \hat{u} \tag{2.24}$$

is applied to the system, transforming the system into the desired structure. The next step is then to design $\hat{u}$ such that the closed-loop system can be proven to be AS.

2.5 Mechanical system modeling

Following from the definition of the Hamiltonian function of n-DoF mechanical systems in (2.16), the inertia matrix and potential energy function of the system are needed for the mathematical modeling of the system. Therefore, this section provides the necessary tools to determine the inertia matrix and the potential energy function.

2.5.1 Denavit-Hartenberg convention

A well known method which allows mathematical modeling of robotic arms is the Denavit-Hartenberg (DH) convention, first introduced by Denavit and Hartenberg (1955). In this thesis, the convention is followed as described by Craig (2009). The DH convention requires the placement of frames (the X, Y and Z-axis) for each joint. For a detailed description of how to place the frames, see Craig (2009), Spong and Vidyasagar (2008), and Siciliano and Khatib (2016). From the frames, four parameters can be determined to describe each link. The four parameters are defined as follows:

$$\begin{aligned}
a_i &= \text{the distance from } Z_i \text{ to } Z_{i+1}\text{, measured along } X_i \\
\alpha_i &= \text{the angle from } Z_i \text{ to } Z_{i+1}\text{, measured about } X_i \\
d_i &= \text{the distance from } X_{i-1} \text{ to } X_i\text{, measured along } Z_i \\
\theta_i &= \text{the angle from } X_{i-1} \text{ to } X_i\text{, measured about } Z_i
\end{aligned} \tag{2.25}$$

In (2.25), the subscript i denotes the i-th ink or joint number. The convention is visualized for two arbitrary links in Figure 2.1.

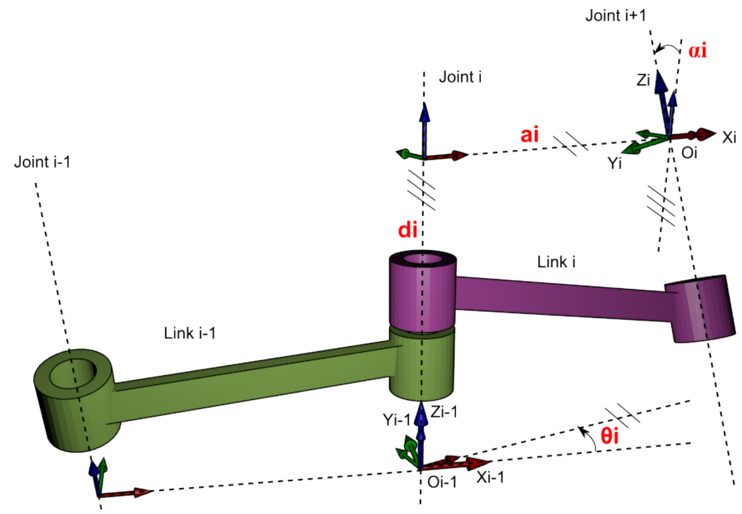

Figure 2.1: Frames and DH parameters for two arbitrary links - by Elhami and Dashti (2016)

2.5.2 Transformation matrix

Using the DH parameters, the transformation from frame $i-1$ to frame i can be defined as a rotation about X (α_{i-1}), a translation about X (a_{i-1}), a rotation about Z (θ_i) and a translation about Z (d_i). The resulting general transformation matrix is (Craig, 2009)

$$ {}^{i-1}_{i}T = \begin{bmatrix} \cos(\theta_i) & -\sin(\theta_i) & 0 & a_{i-1} \\ \sin(\theta_i)\cos(\alpha_{i-1}) & \cos(\theta_i)\cos(\alpha_{i-1}) & -\sin(\alpha_{i-1}) & -\sin(\alpha_{i-1})d_i \\ \sin(\theta_i)\sin(\alpha_{i-1}) & \cos(\theta_i)\sin(\alpha_{i-1}) & \cos(\alpha_{i-1}) & \cos(\alpha_{i-1})d_i \\ 0 & 0 & 0 & 1 \end{bmatrix}. \tag{2.26} $$

Using (2.26), the homogeneous transformation matrix from the base frame to the i^{th} frame is defined as

$$ \begin{aligned} {}^{0}_{i}T &= {}^{0}_{1}T\, {}^{1}_{2}T \ldots {}^{i-1}_{i}T \\ &= \begin{bmatrix} \mathcal{R}_i & o_i \\ \mathbf{0}_{1\times 3} & 1 \end{bmatrix}, \end{aligned} \tag{2.27} $$

where $\mathcal{R}_i \in \mathbb{R}^{3\times 3}$ represents the rotation matrix from the base frame to the i^{th} frame and $o_i \in \mathbb{R}^3$ is the position vector from the base frame to the i^{th} frame.

2.5.3 Jacobian

The Jacobian matrix should be defined for each link. The Jacobian matrix defines the mapping from the velocities and forces in joint space to the velocities and forces in Cartesian space, respectively (Craig, 2009). The columns of the Jacobian matrix are given by (Spong and Vidyasagar, 2008)

$$ \mathcal{J}_i = \begin{bmatrix} \mathcal{J}_{v_i} \\ \mathcal{J}_{\omega_i} \end{bmatrix} = \begin{bmatrix} z_{i-1} \times (o_n - o_{i-1}) \\ z_{i-1} \end{bmatrix}, \tag{2.28} $$

where $\mathcal{J}_{v_i} \in \mathbb{R}^3$ denotes the i^{th} column of the linear Jacobian matrix, $\mathcal{J}_{\omega_i} \in \mathbb{R}^3$ denotes the i^{th} column of the angular Jacobian matrix, $z_{i-1} \in \mathbb{R}^3$ denotes the third column of the rotation matrix $\mathcal{R}_i$ and $o_n, o_{i-1} \in \mathbb{R}^{3\times 3}$ denote the position vector from the base frame to the $\{i-1\}^{th}$ frame and the final frame, respectively.

In the Jacobian matrix for the i^{th} link, the first i columns are defined by (2.28). The remaining columns of the Jacobian matrix of the same link are equal to zero, such that the Jacobian matrix of link i, $\bar{\mathcal{J}}_i \in \mathbb{R}^{6\times n}$. Therefore, we have the linear and angular Jacobian matrices of link i, $\bar{\mathcal{J}}_{v_i}, \bar{\mathcal{J}}_{\omega_i} \in \mathbb{R}^{3\times n}$.

2.5.4 Principal moment of inertia

The final component that is needed before the inertia matrix can be computed, is the principal moment of inertia about the Z-axis, which is part of the inertia tensor (Spong and Vidyasagar, 2008). Simplifying the links of the robotic arm such that each link can be represented as a cuboid with constant density, the principal moment of inertia of link i about the Z-axis follows from its definition as

$$\mathcal{I}_i = \frac{m_i}{12}(x_i^2 + y_i^2), \tag{2.29}$$

where $m_i \in \mathbb{R}$ is the mass of link i and $x_i, y_i \in \mathbb{R}$ represent the size of the link in the direction of the X-axis and Y-axis, respectively.

2.5.5 Inertia matrix

Using the rotation matrices, Jacobian matrices and the principal moments of inertia, the inertia matrix of the system is obtained by (Spong and Vidyasagar, 2008)

$$M(q) = \sum_{i=1}^{n} \left[m_i \bar{\mathcal{J}}_{v_i}(q)^\top \bar{\mathcal{J}}_{v_i}(q) + \bar{\mathcal{J}}_{\omega_i}(q)^\top \mathcal{R}_i(q) \mathcal{I}_i \mathcal{R}_i(q)^\top \bar{\mathcal{J}}_{\omega_i}(q) \right]. \tag{2.30}$$

Note that the argument q is inserted here, representing the angular positions of the joints of the PERA.

2.5.6 Potential energy

For the PERA, the total potential energy of the system is equal to the gravitational potential energy of the system. The potential energy can be split up into the potential energy per link of the PERA. The potential energy of link i is given by

$$V_i(q) = m_i g h_i + V_{ref,i}, \tag{2.31}$$

where $m_i \in \mathbb{R}$ is the mass of link i, $g = 9.81 \ [\frac{m}{s^2}]$ is the acceleration due to gravity, $h_i \in \mathbb{R}$ is the height of the center of mass (CoM) of the i^{th} link and $V_{ref,i} \in \mathbb{R}$ is a constant such that the minimum of V_i is at zero.

The relative height of the i-th joint with respect to the base frame is given by the position of the axis of rotation of the i-th joint on the Z-axis, i.e.

$$H_i = e_3 o_i \tag{2.32}$$

By observation of the PERA and verification by experiments (see Chapter 5), it was determined that the CoM of each link is located at approximately one third of the link's length. Therefore, the height of the CoM of link i is defined as

$$h_i = \frac{2}{3} H_{i-1} + \frac{1}{3} H_i. \tag{2.33}$$

The total potential energy of the system is given by the sum of the potential energy of all links, i.e.,

$$V(q) = \sum_{i=1}^{n} V_i(q). \tag{2.34}$$

Chapter 3

Experimental setup

In this thesis, experiments are conducted with the PERA, where a model-based control approach is implemented. Therefore, the first step in the control design is to develop a suitable mathematical model of the system. To this end, this chapter provides all required information on the current setup of the PERA at the University of Groningen.

The kinematics of the PERA are described in Section 3.1. Next, the model of the PERA is reduced to the three DoF that are used in this thesis and the DH parameters are obtained in Section 3.2. Then, the inertia matrix and potential energy of the PERA are derived in Section 3.3 and 3.4, after which the end-effector is described in Section 3.5. The hardware of the motors is discussed in Section 3.6 and finally, this chapter concludes with a description of the sensors in the PERA in Section 3.7.

3.1 Kinematics

The PERA is a robotic arm with seven DoF, excluding the end-effector, which can bee seen as the eighth DoF. The arm is developed to resemble a human arm (Rijs et al., 2014). To this end, the joints of the arm are located in the shoulder (3 DoF), elbow (2 DoF), and wrist (2 DoF) of the arm. The robotic arm is mounted to a frame representing the human upper body.

Figure 3.1 provides a graphical representation of the arm, where the letters R, P and Y denote a joints roll, pitch and yaw, while the subscripts S, E and W denote the corresponding joint (shoulder, elbow and wrist, respectively).

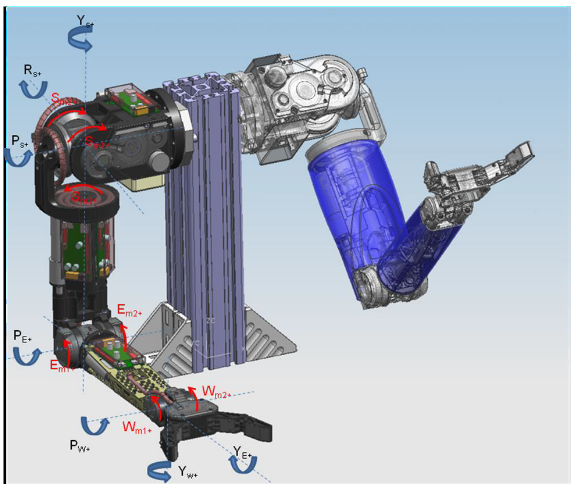

Figure 3.1: Kinematics of the PERA - by Rijs et al. (2014)

The range of motion (RoM) of each joint is limited by mechanical end stops inside the arm. The RoM of the joints is given in Table 3.1, with Figure 3.1 as the zero-position. For visual descriptions of the RoM of the joints, the reader is referred to the manual of the PERA (Rijs et al., 2014). The characteristics of the links between joints are given in Table 3.2. Note that the shoulder joints, elbow joints and wrist joints are considered to be one joint of multiple (two or three) DoF. To accommodate this in the modeling of the PERA, these joints can be expressed as two or three, connected by links of zero length (Spong and Vidyasagar, 2008). Thus, three links of non-zero length allow the connection of all joints and the gripper to the base frame. These links resemble the human upper arm, lower arm and hand.

Joint	**Min.**	**Max.**
R_S	$0°$	$+90°$
P_S	$-90°$	$+90°$
Y_S	$-90°$	$+90°$
P_E	$-90°$	$+55°$
Y_E	$-105°$	$+105°$
P_W	$-57°$	$+57°$
Y_W	$-45°$	$+45°$
Gripper	$0°$	$+45°$

Table 3.1: Restrictions on the joint angles of the PERA (Rijs et al., 2014; van den Bos, 2019)

Link	**Length** $[m]$	**Mass** $[kg]$
Upper arm	0.32 (L_1)	2.9 (m_1)
Lower arm	0.28	0.8
Hand	0.20	0.2

Table 3.2: Specifications of the links of the PERA (Rijs et al., 2014)

3.2 Denavit-Hartenberg parameters

In the past, the spatial dynamics of the PERA have been described by Bol (2012), Koops (2014), Muñoz-Arias (2015), and van den Bos (2019). In this thesis, however, only the shoulder pitch, shoulder yaw and elbow pitch are considered. From now on, the position of these joints will be referred to as q_1, q_2 and q_3, respectively. Furthermore, the end effector is considered as a fourth DoF. A schematic representation of the PERA with the joints in this thesis is provided in Figure 3.2. Note that, since the wrist joints are not used, the lower arm and hand now become one link ($L_2 = 0.48$ $[m]$, $m_2 = 1.0$ $[kg]$).

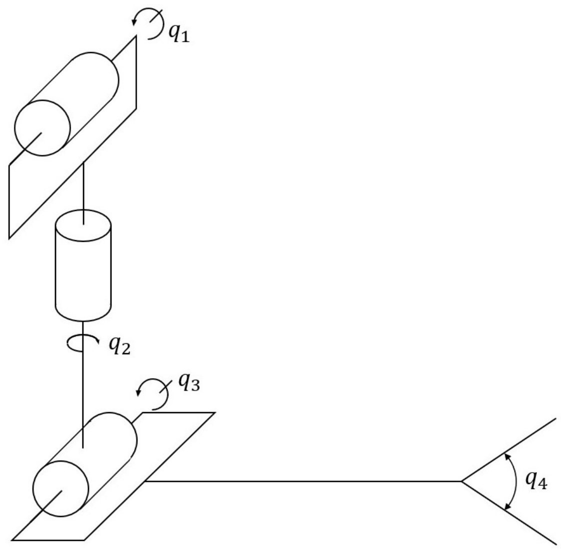

Figure 3.2: Schematic representation of the PERA

The DH parameters for the configuration of the PERA in Figure 3.2 are obtained by the convention as described in Chapter 2. The results are in Table 3.3.

To verify the validity of the DH parameters, a graphical model of the PERA was constructed in MATLAB®, using the Robotic Toolbox developed by Corke et al. (1996). The resulting model is depicted in Figure 3.3. This result verifies that the DH parameters are correct. The constructed

i	α_{i-1}	a_{i-1}	d_i	θ_i
1	$\frac{\pi}{2}$	0	0	q_1
2	$-\frac{\pi}{2}$	0	-0.32	q_2
3	$\frac{\pi}{2}$	0	0	$q_3 - \frac{\pi}{2}$
4	0	-0.48	0	0

Table 3.3: Denavit-Hartenberg link parameters

MATLAB® model is constructed such that joint rotations in the model are true to the rotations of the physical PERA. Furthermore, the zero position of the model is equal to that of the PERA.

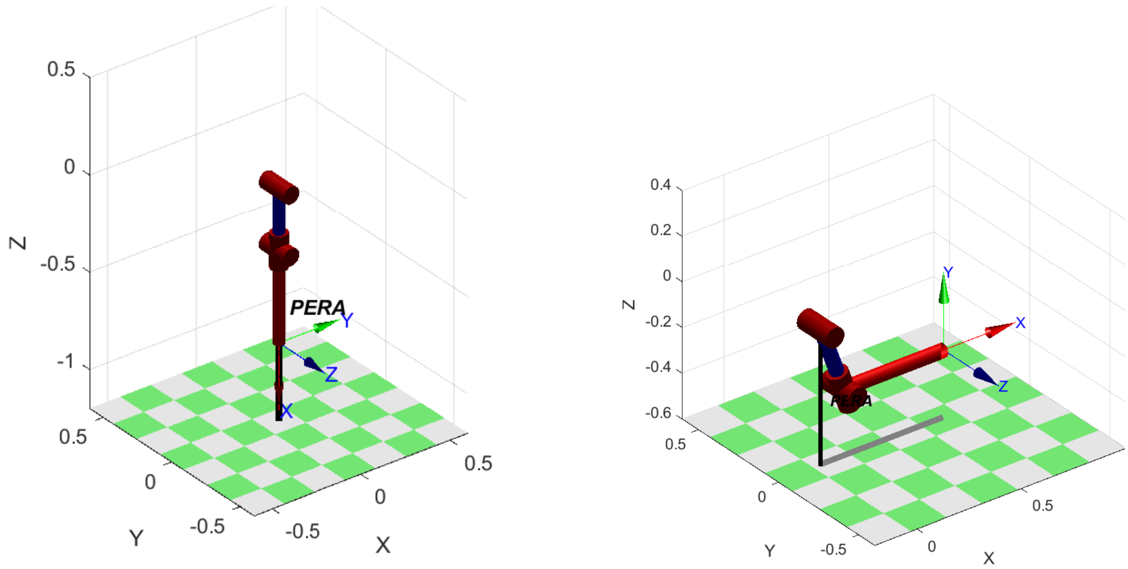

(a) $q_1 = 0°$, $q_2 = 0°$, $q_3 = 0°$

(b) $q_1 = 20°$, $q_2 = 0°$, $q_3 = 70°$

Figure 3.3: Graphical model of the PERA

3.3 Inertia matrix

Following the method described in Chapter 2, the inertia matrix of the PERA was obtained from the DH parameters in Table 3.3. Following (2.30), the inertia matrix is given by

$$M(q) = \begin{bmatrix} \mathcal{I}_1 + \mathcal{I}_2 + \mathcal{I}_3 + (m_1 + m_2)L_1^2 \sin^2(q_1) & 0 & \mathcal{I}_3 \cos(q_1) \\ 0 & \mathcal{I}_2 + \mathcal{I}_3 + m_2 L_1^2 & 0 \\ \mathcal{I}_3 \cos(q_1) & 0 & \mathcal{I}_3 \end{bmatrix}. \tag{3.1}$$

Filling in the values for I_1, I_2, I_3, m_1, m_2, L_1 and L_2 yields

$$M(q) = \begin{bmatrix} 0.05 + 0.40 \sin^2(q_1) & 0 & 0.02 \cos(q_1) \\ 0 & 0.42 & 0 \\ 0.02 \cos(q_1) & 0 & 0.02 \end{bmatrix}. \tag{3.2}$$

3.4 Potential energy

Using (2.34), the potential energy is computed as

$$V(q) = -\left(\frac{1}{3}m_1 + m_2\right) gL_1 \cos(q_1) + \frac{1}{3}m_2 gL_2 \big[\cos(q_2)\sin(q_1)\sin(q_3) - \cos(q_1)\cos(q_3)\big], \quad (3.3)$$

with the partial derivative of the potential energy with respect to q,

$$\frac{\partial V}{\partial q}(q) = \begin{bmatrix} \left(\frac{1}{3}m_1 + m_2\right) gL_1 \sin(q_1) + \frac{1}{3}m_2 gL_2 \big[\cos(q_2)\cos(q_1)\sin(q_3) + \sin(q_1)\cos(q_3)\big] \\ -\frac{1}{3}m_2 gL_2 \big[\sin(q_2)\sin(q_1)\sin(q_3)\big] \\ \frac{1}{3}m_2 gL_2 \big[\cos(q_2)\sin(q_1)\cos(q_3) + \cos(q_1)\sin(q_3)\big] \end{bmatrix}. \quad (3.4)$$

Inserting the values for m_1, m_2, g, L_1 and L_2 yields

$$V(q) = -6.17\cos(q_1) + 1.57\big[\cos(q_2)\sin(q_1)\cos(q_3) - \cos(q_1)\cos(q_3)\big], \quad (3.5)$$

with the partial derivative with respect to q,

$$\frac{\partial V}{\partial q}(q) = \begin{bmatrix} 6.17\sin(q_1) + 1.57\big[\cos(q_2)\cos(q_1)\sin(q_3) + \sin(q_1)\cos(q_3)\big] \\ -1.57\big[\sin(q_2)\sin(q_1)\sin(q_3)\big] \\ 1.57\big[\cos(q_2)\sin(q_1)\cos(q_3) + \cos(q_1)\sin(q_3)\big] \end{bmatrix}. \quad (3.6)$$

3.5 End-Effector

The PERA is equipped with a two-finger gripper as end-effector, allowing the arm to grasp objects. The outline of the gripper is given in Figure 3.4. The grippers' symmetrical fingers can be opened or closed simultaneously by an actuating Maxon motor, which is located inside the red rectangle in Figure 3.4. the rational motion of the motor is transformed into a translational motion by the screw, which is located inside the orange rectangle in Figure 3.4. The screw is connected to the fingers by cables (yellow lines in Figure 3.4). A linear spring is located between the fingers, such that a force is exerted when the distance between the fingers is less than four centimeters. This ensures that the fingers' positions are symmetric when grasping an object. For a more elaborate description of the gripper and its dynamics, the reader is referred to the theses of de Jong (2013), Siemonsma (2014), and van den Bos (2019).

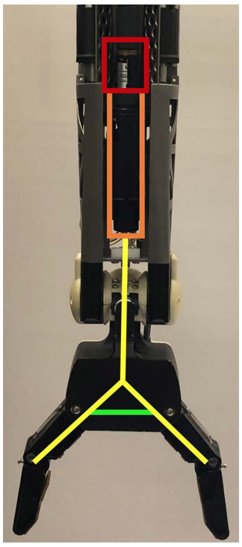

Figure 3.4: Picture of the gripper of the PERA - by van den Bos (2019)

3.6 Joint actuation

For the design and tuning of a control law, knowledge of the actuation of the joints of the PERA is required. Therefore, this section elaborates on the motors, gearing and boards which actuate the rotational joints of the PERA. First, the actuation of the motors via boards is discussed, after which the working principles of the differential drives in the PERA are explained. Next, relevant parameters of the motors and gearing are provided. Then, these parameters are used to determine appropriate saturation limits of the control law. Furthermore, this chapter concludes with the original control law which is implemented on the PERA.

3.6.1 Boards

The communication between the PC and the PERA runs through four RT-motion USB motion control boards. Each board puts through the sensor and actuation signals for two motors. The boards are accessed by the PC via a USB connection. Table 3.4 shows which joints and motors are connected to which board.

The control signal from the PC is sent to the motors via the corresponding boards. Since it is not possible to send a current to the motors directly, a input signal in counts is sent to the boards. This input signal is translated to the desired current by a non-linear amplifier. The behaviour of the non-linear amplifier differs per board. This is depicted in Figure 3.5.

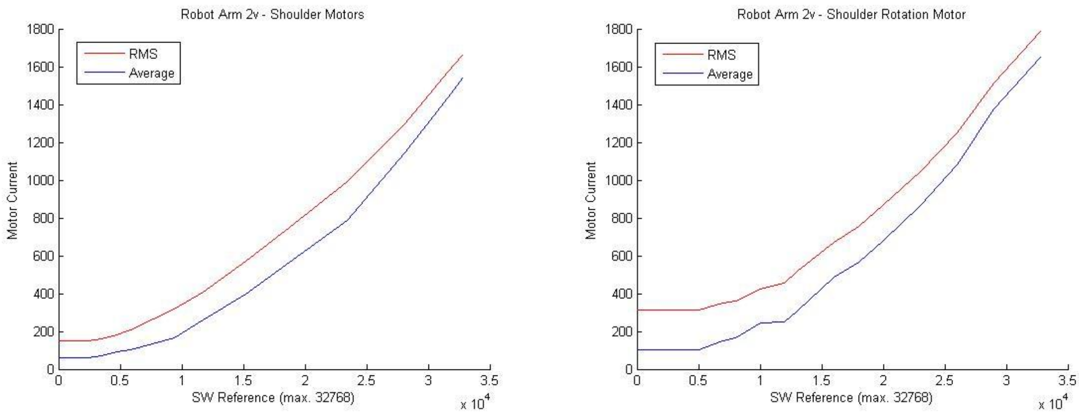

(a) Shoulder motors 1 and 2 (board 1)

(b) Shoulder motor 3 (board 3)

Furthermore, the signals from sensors in the PERA are sent to the PC through the boards. The present sensors and their signals are discussed in Section 3.7. For a detailed overview of the wiring of the PERA, the reader is referred to Appendix A.

Board number	**Joint 1**	**Joint 2**	**Motor 1**	**Motor 2**
1	R_S	P_S	S_1	S_2
2	P_E	Y_E	E_1	E_2
3	Y_S	Gripper	S_3	G
4	P_W	Y_W	W_1	W_2

Table 3.4: Board numbers and corresponding joints

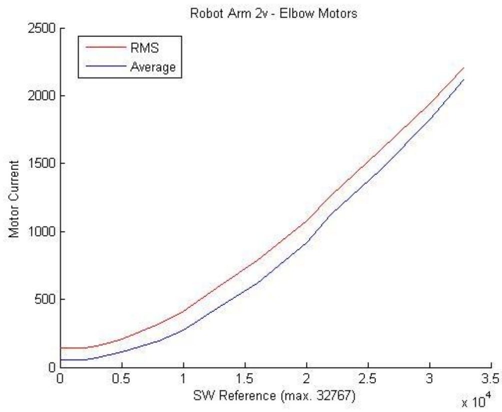

(c) Elbow motors 1 and 2 (board 2)

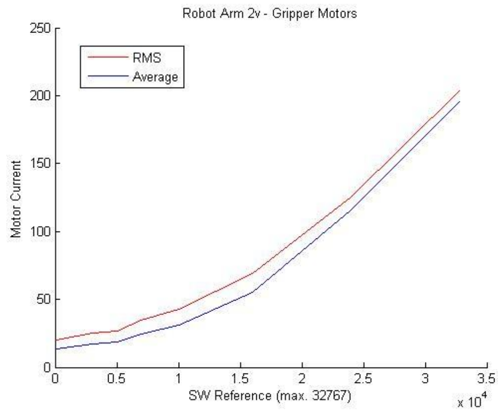

(d) Gripper motor (board 3)

Figure 3.5: Behaviour of non-linear amplifiers - by Rijs et al. (2014)

3.6.2 Differential drives

Boards 1, 2 and 3 in the previous section connect the PC to the differential drives in the shoulder, elbow and wrist, respectively. These differential drives are actuated by two motors, such that that the dynamics of the differential drive are described by

$$\begin{aligned} \varphi_{out,1} &= \frac{1}{2}(\varphi_{motor,1} + \varphi_{motor,2}) \\ \varphi_{out,2} &= \frac{1}{2}(\varphi_{motor,1} - \varphi_{motor,2}) \\ T_{out,1} &= T_{motor,1} + T_{motor,2} \\ T_{out,2} &= T_{motor,1} - T_{motor,2}, \end{aligned} \tag{3.7}$$

where φ denotes the angle of rotation, T denotes the torque exerted and the subscripts $out1$ and $out2$ refer to the first[1] and orthogonal second[2] DoF actuated by the differential drive, respectively, while the subscripts $motor1$ and $motor2$ refer to the orange gears in Figure 3.6.

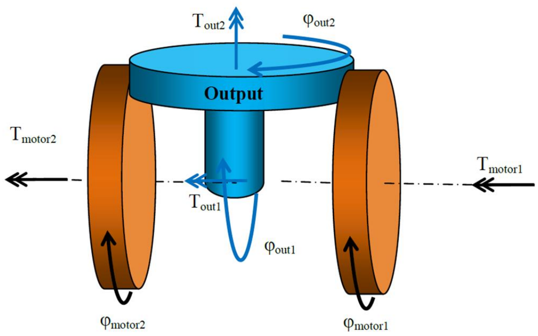

Figure 3.6: Schematic outline of the differential drives in the PERA - by Rijs et al. (2014)

Since the joints considered in this project are the shoulder pitch, shoulder yaw and elbow pitch, the differential drives of the shoulder and elbow are used to actuate one DoF each. For the shoulder, the shoulder pitch (P_S) is the second DoF of the differential drive and therefore, the first DoF (R_S) does not move from the zero position ($\varphi_{out1} = T_{out1} = 0$). This allows the rewriting of (3.7)

[1] R_S, P_E and P_W
[2] P_S, Y_E and Y_W

as

$$\begin{aligned} \varphi_{S_1} &= -\varphi_{S_2} \\ T_{S_1} &= -T_{S_2}, \end{aligned} \tag{3.8}$$

where the subscripts S_1 and S_2 denote the first and second motor in the shoulder. Similarly, the differential drive at the elbow actuates only the first DoF (P_E), such that the dynamics of the differential drive become

$$\begin{aligned} \varphi_{E_1} &= \varphi_{E_2} \\ T_{E_1} &= T_{E_2}, \end{aligned} \tag{3.9}$$

where the subscripts E_1 and E_2 refer to the motors in the elbow of the PERA. From (3.8) and (3.9), it follows that for the joints in this thesis that are actuated by a differential drive, both motors of the drive deliver half of the required torque on the joint. To accommodate this fact, a factor k_d was added to the conversion of joint torque to motor current, see Section 3.6.4. The values of k_d for different joints are defined in Table 3.5.

Joint	$\mathbf{k_d}$
S_1	2
S_2	-2
S_3	1
E_1	2
E_2	2

Table 3.5: Values of the factor k_d

3.6.3 Motor and gearing parameters

The joints of the PERA are actuated by eight DC motors, produced by Maxon Group (Rijs et al., 2014). An image of such a motor is depicted in Figure 3.7. The parameters of the motors and

Figure 3.7: DC motor of the PERA (S_1 and S_2) - by Maxon Group (n.d.)

gearing differ from joint to joint. Therefore, relevant information on these matters is provided in Table 3.6. Gearing ratios are the total gearing ratios in the PERA, as defined in Rijs et al. (2014). Other parameter values are taken from the data-sheets of the parts. The reader is referred to Appendix B for the complete data-sheets.

[3]Since the gripper is not a rotational joint, the gearing ratio given is that of the gearing part.

Motor(s)	Motor part no.	Gearing part no.	Torque constant (k_m)	Gearing ratio (G_r)	Gearing efficiency (η)	Nominal voltage
S_1 and S_2	268216	166940	53.8 $[\frac{mN \cdot m}{A}]$	550	0.70	48 $[V]$
S_3	268214	166940	25.9 $[\frac{mN \cdot m}{A}]$	371.25	0.70	24 $[V]$
E_1 and E_2	118752	166938	23.4 $[\frac{mN \cdot m}{A}]$	348	0.75	24 $[V]$
G	118641	110314	16.0 $[\frac{mN \cdot m}{A}]$	17 [3]	0.83	24 $[V]$

Table 3.6: Motor and gearing part numbers and parameters

3.6.4 Saturation limits

The controller proposed in this thesis determines the required torque on each joint. However, the input to the motors is a current sent by the boards. Therefore, the desired torque is converted to the desired current, which is in turn converted to a signal in counts, such that the motors receive the desired current from the boards.

First, the desired torque on the joint is translated to the desired current from the motor. This transformation is given by

$$u_{\text{current},i} = \frac{1000 \cdot 1000 \cdot u_{\text{torque},i}}{G_r \cdot \eta \cdot k_m \cdot k_d}, \tag{3.10}$$

where the values of parameters are given in Tables 3.5 and 3.6 and the subscript i denotes the joint. The two factors 1000 are added to transform the units such that the desired torque is transformed from $N \cdot m$ to $mN \cdot m$ and the desired current is transformed from A to mA.

Next, the value of the desired current for each motor is translated to a signal in counts. The relation of the signal in counts and the current sent to the motor was previously given in Figure 3.5. As discussed in (Koops, 2014), the best approach to compute the desired signal in counts is to approximate the average graphs in Figure 3.5 by a second order polynomial. The limits of the gripper motor are defined such that

$$-28000 \leq u_{\text{counts}} \leq 28000, \tag{3.11}$$

while the limits of all other motors are such that

$$-16000 \leq u_{\text{counts}} \leq 16000. \tag{3.12}$$

These symmetrical saturations have been introduced in (Bol, 2012), to protect the motors of the PERA from high currents which could damage the motors. The polynomial approximations are fitted to the non-linear amplifier values within these limits. The following second order polynomial approximations are found using the `polyfit` function in MATLAB®.

$$\begin{aligned} u_{\text{counts},S_1,S_2} &= -0.05u^2_{\text{current},S_1,S_2} + 57.532u_{\text{current},S_1,S_2} + 198.72 \\ u_{\text{counts},S_3} &= -0.0486u^2_{\text{current},S_3} + 57.525u_{\text{current},S_3} - 545.36 \\ u_{\text{counts},E_1,E_2} &= -0.0088u^2_{\text{current},E_1,E_2} + 26.01u_{\text{current},E_1,E_2} + 3080.7 \\ u_{\text{counts},G} &= -0.7652u^2_{\text{current},G} + 292.19u_{\text{current},G} + 846.19 \end{aligned} \tag{3.13}$$

The non-linear relationships are plotted in Figures 3.8 and 3.9.

From the relationships given in (3.10), (3.11), (3.12) and (3.13) and the parameter values given in Tables 3.5 and 3.6, the saturation limits on the torque can now be computed. These limits are

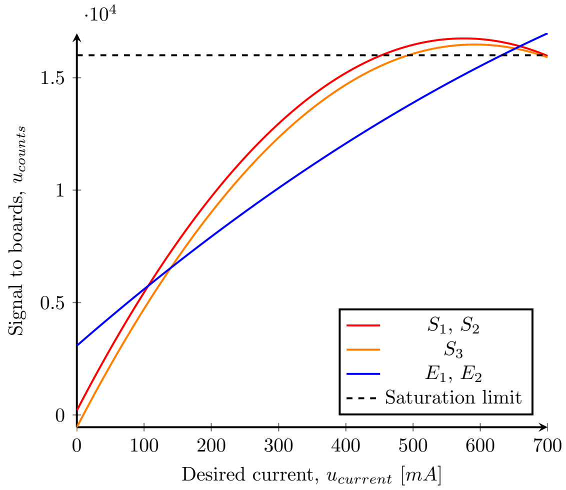

Figure 3.8: Relationship between the desired current and the signal in counts (joint motors)

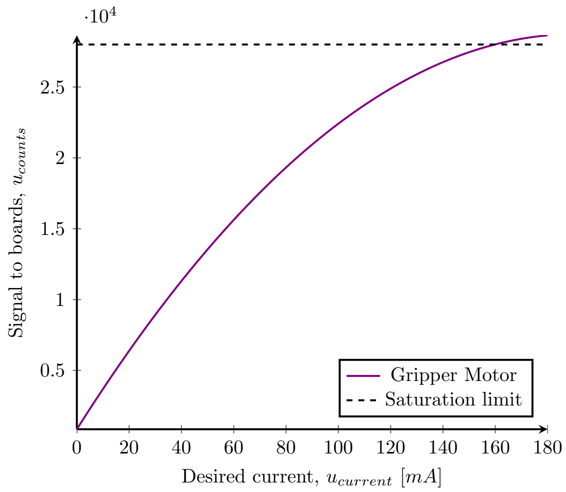

Figure 3.9: Relationship between the desired current and the signal in counts (gripper motor)

defined as

$$\begin{aligned} -18.77 \leq u_1 \leq 18.77 \\ -3.32 \leq u_2 \leq 3.32 \\ -7.72 \leq u_3 \leq 7.72. \end{aligned} \tag{3.14}$$

By designing the control law according to the limits in (3.14), it is ascertained that the signal to the boards will never exceed the limits in (3.11) and (3.12).

3.7 Sensors

To finalize this chapter, the sensors of the PERA are discussed. Sensors allow the measurement of the states of the PERA. These measurements can subsequently be used to control the robotic arm by a control law. Each joint of the PERA is equipped with a force sensor (Osram SFH 9202) and two types of positions sensors.

3.7.1 Force sensors

Each DoF of the PERA contains a compliant element, which is attached to the load side of the gearing, such that the deformation of the element is not influenced by the gearing friction.

By approximation, the deformation of the compliant element is proportional to the load force. Therefore, the magnitude of the force can be determined from the deformation, which is measured by an optical sensor (Rijs et al., 2014).

In this thesis, only the force sensors in the wrist of the PERA are used. The force sensors of the joints of the PERA measure the combination of the motor force, gravitational force and other external forces on the joint. Moreover, the force sensor in the gripper measures not only these forces, but also the force induced by the spring in the gripper. For a more detailed description of the force dynamics in the gripper, the reader is referred to the works of Bol (2012) and Siemonsma (2014). The force measured by sensors can be simplified to (van den Bos, 2019)

$$F_{sensor} = F_{int} + F_{ext}, \tag{3.15}$$

where F_{int} denotes the force on the joint generated by the motor and F_{ext} denotes the gravitational force on the motor and, in the case of the gripper, the spring force on the joint.

The signal from the force sensor in the gripper is saturated, such that (Siemonsma, 2014)

$$0 \leq F_{sensor} \leq 200. \tag{3.16}$$

The signals from the other force sensors are presumably saturated as well, but this is not investigated in this thesis. Note that the signal from the force sensors is given in counts, not in Newtons or Newton-meters.

3.7.2 Position sensors

In the PERA, each joint is equipped with two types of position sensors; Hall angle sensors and motor encoders. The Hall sensors measure the magnitude of the magnetic field to determine the absolute position of the joint. The Hall angle sensors on the PERA are developed by AustriaMicrosystems (AMS)(Rijs et al., 2014); the elbow is equipped with 10-bit Hall angle sensors (AS5040), resulting in a resolution of 0.352°, and the other joints are equipped with 12-bit Hall angle sensors (AS5145), resulting in a resolution of 0.088°. The major downside of Hall angle sensors is that they are very susceptible to external magnetic fields. For more information on the Hall angle sensors of the PERA, the reader is referred to the work of Bol (2012) and the data-sheets of the sensors (Appendix B).

In this thesis, the motor encoders are used to measure the position of joints. The encoders are designed and produced by Maxon group. The encoders are located on the motor axis, such that the relative position of the motor is measured and translated into a signal in counts. The part numbers and translation constants of encoders in the PERA are given in Table 3.7. Note that the column 'Degrees per Count' gives the conversion factor from encoder counts on the motor to the position of the joint (or in the case of a differential drive, final gear) in degrees. These conversion factors are taken from the existing PERA controller code. Furthermore, the part numbers of the encoders were found on the parts of the PERA, except for the encoder of the gripper, which has no visible part number.

Joint	Motor(s)	Part No.	Degrees per Count
q_1	S_1, S_2	225783	$6.45 \cdot 10^{-4}$
q_2	S_3	225783	$9.45 \cdot 10^{-4}$
q_3	E_1, E_2	225778	$4.54/4.38 \cdot 10^{-4}$
	W_1, W_2	228177	$2.43/-2.72 \cdot 10^{-3}$
	G	323052	$6.00 \cdot 10^{-4}$

Table 3.7: Encoder part numbers and translation constants

The major downside of using the encoder sensors is the offset in the measurements. Every time the PERA is activated, the encoders are recalibrated by determining and compensating for the offset. However, the determination of this offset is not perfect and returns a different value every time the PERA is activated. Therefore, the zero positions of the joints in one experiment may slightly differ from the zero positions in the next experiment.

3.8 Original control law

For the sake of completeness, the original control strategy of the PERA is discussed here. In the original control files, the desired torque on the joints of the PERA is defined by a simple PID control law. This control law is applied to the error of the joint positions with respect to the desired positions. When the system is started, the desired positions are set to the current positions. Via a terminal window, the desired positions can be altered, such that the joint moves to the desired position. The PID tuning of the original control file is given in Table 3.8. As can be observed, the integral gains are all equal to zero, such that the control laws of the joints are actually PD controllers. Moreover, the gripper is controlled with a simple proportional controller. In the experiments conducted in this thesis, the joints which are not considered are kept at the initial position by these PD controllers.

Joint	**P**	**I**	**D**
R_S	4	0	0.5
P_S	4	0	0.5
Y_S	40	0	0.5
P_E	10	0	1
Y_E	10	0	1
P_W	10	0	0.8
Y_W	10	0	0.8
Gripper	30	0	0

Table 3.8: PID tuning of the original controller of the joints of the PERA

Chapter 4

Control design

The goal of this chapter is to propose a controller for the PERA and prove stability of the closed-loop system. The PERA does not have any velocity sensors and derivation of the velocity from the position sensors was deemed insufficiently accurate by Bol (2012). Therefore, the control law to be proposed cannot make use of the velocities of the joints. The control laws proposed in this chapter are a continuation on the works of Wesselink (2018), Wesselink, Borja, and Scherpen (2018), and van den Bos (2019).

First, the mathematical modeling of the PERA is discussed. The desired system dynamics are defined and by comparison of the actual system dynamics to the desired system dynamics, the error dynamics are found. Next, the error dynamics are re-expressed in the pH framework and three control laws are proposed to stabilize the error dynamics in the desired equilibrium. The last controller proposed is used in the experiments, as discussed in the next chapter. Finally, the chapter concludes with a section on the complete control of the joints and gripper of the PERA.

4.1 Mathematical modeling

Several steps need to be taken to allow stabilization of the joints of the PERA on the desired trajectory. First, the PERA is modeled in the pH framework. It should be noted that the natural damping of the system is not considered, because it is unknown. Then, to determine the desired steady-state control input, the desired system is obtained. Furthermore, the error dynamics of the PERA are defined, allowing control strategies for the system to be proposed.

4.1.1 System dynamics

As discussed earlier, the PERA is a fully actuated system and three joints are considered in this thesis, i.e. $m = n = 3$. Therefore, the input matrix G is defined as the identity matrix, i.e. $G = I_3$. Moreover, the elements of the input vector u denote the torque exerted by the motors on their respective joints. Therefore, following, (2.15), the dynamics of the PERA in the pH framework are described by

$$\begin{aligned} \begin{bmatrix} \dot{q} \\ \dot{p} \end{bmatrix} &= \begin{bmatrix} \mathbf{0}_{3\times 3} & I_3 \\ -I_3 & \mathbf{0}_{3\times 3} \end{bmatrix} \begin{bmatrix} \frac{\partial H}{\partial q}(q,p) \\ \frac{\partial H}{\partial p}(q,p) \end{bmatrix} + \begin{bmatrix} \mathbf{0}_{3\times 3} \\ I_3 \end{bmatrix} u \\ y &= \frac{\partial H}{\partial p}(q,p), \end{aligned} \tag{4.1}$$

with the general Hamiltonian function, as given in (2.16).

Next, the PLvCC transform proposed by Venkatraman et al. (2010), as discussed in Subsection 2.3.2, is applied to the PERA, such that the inertia matrix becomes constant in the new coordinates, while the pH structure of the system is preserved. This is done to simplify the system, which allows for the control strategies proposed. As a result, we have the dynamics of the PERA in the new coordinates as

$$\begin{aligned}\begin{bmatrix} \dot{q} \\ \dot{\mathtt{P}} \end{bmatrix} &= \begin{bmatrix} \mathbf{0}_{3\times 3} & \Psi(q) \\ -\Psi^\top(q) & J(q,p) \end{bmatrix} \begin{bmatrix} \frac{\partial \bar{H}}{\partial q}(q,\mathtt{P}) \\ \frac{\partial \bar{H}}{\partial \mathtt{P}}(q,\mathtt{P}) \end{bmatrix} + \begin{bmatrix} \mathbf{0}_{3\times 3} \\ \Psi^\top(q) \end{bmatrix} u \\ y &= \Psi(q)\frac{\partial \bar{H}}{\partial \mathtt{P}}(q,\mathtt{P}) = \dot{q},\end{aligned} \tag{4.2}$$

with the Hamiltonian (2.22)

$$\bar{H}(q,\mathtt{P}) = \frac{1}{2}\mathtt{P}^\top \mathtt{P} + V(q), \tag{4.3}$$

where the potential enegry $V(q)$ is given by (3.3) and

$$\Psi(q) = \begin{bmatrix} \frac{6.0\times 10^{10}}{\sqrt{1.5\times 10^{21}\sin^2(q_1)+1.1\times 10^{20}}} & 0 & 0 \\ 0 & 1.5 & 0 \\ \frac{-6.0\times 10^{10}\cos(q_1)}{\sqrt{1.6\times 10^{21}-1.5\times 10^{21}\cos^2(q_1)}} & 0 & 7.2 \end{bmatrix}; \quad J(q,p) = \mathbf{0}_{3\times 3}, \tag{4.4}$$

which follows form (2.20) and (2.23). It is verified that

$$\Psi(q)\Psi^\top(q) = M^{-1}(q), \tag{4.5}$$

with $M(q)$ as in (3.2). Note that the matrix $\Psi(q)$ is full rank.

4.1.2 Desired system dynamics

The desired dynamics of the system are used as a reference for the actual system. The desired dynamics should satisfy the actual dynamics (4.2) (Aström and Murray, 2010), i.e. the desired trajectory can be followed. The desired dynamics of the system depend fully on the desired trajectory. Following (4.2), the desired dynamics of the system, i.e. the system dynamics for the desired states, are described by

$$\begin{aligned}\begin{bmatrix} \dot{q}_d \\ \dot{\mathtt{P}}_d \end{bmatrix} &= \begin{bmatrix} \mathbf{0}_{3\times 3} & \Psi(q) \\ -\Psi^\top(q) & \mathbf{0}_{3\times 3} \end{bmatrix} \begin{bmatrix} \frac{\partial \bar{H}_d}{\partial q_d}(q_d,\mathtt{P}_d) \\ \frac{\partial \bar{H}_d}{\partial \mathtt{P}_d}(q_d,\mathtt{P}_d) \end{bmatrix} + \begin{bmatrix} \mathbf{0}_{3\times 3} \\ \Psi^\top(q) \end{bmatrix} u_d \\ y_d &= \Psi(q_d)\frac{\partial \bar{H}}{\partial \mathtt{P}}(q_d,\mathtt{P}_d) = \dot{q}_d,\end{aligned} \tag{4.6}$$

with the Hamiltonian

$$\bar{H}_d(q_d,\mathtt{P}_d) = \frac{1}{2}\mathtt{P}_d^\top \mathtt{P}_d + V(q_d). \tag{4.7}$$

Assuming that the positions converge to the desired trajectory, i.e.,

$$\lim_{t\to\infty} q(t) = q_d(t), \tag{4.8}$$

the desired steady-state input is defined as

$$u_d = \frac{\partial V}{\partial q}(q_d) + \Psi^{-\top}(q_d)\frac{d\Psi^{-1}(q_d)\dot{q}_d}{dt} \tag{4.9}$$

to satisfy the system dynamics.

4.1.3 Error dynamics

The dynamics of the state errors are found by comparing the actual system dynamics to the desired system dynamics. The error dynamics of the system are given by

$$\begin{aligned}\begin{bmatrix} \dot{\tilde{q}} \\ \dot{\widetilde{\mathtt{P}}} \end{bmatrix} &= \begin{bmatrix} \mathbf{0}_{3\times 3} & \Psi(q) \\ -\Psi^\top(q) & \mathbf{0}_{3\times 3} \end{bmatrix} \begin{bmatrix} \frac{\partial V}{\partial q}(q) - \frac{\partial V}{\partial q}(q_d) \\ \widetilde{\mathtt{P}} \end{bmatrix} + \begin{bmatrix} \mathbf{0}_{3\times 3} \\ \Psi^\top(q) \end{bmatrix} \tilde{u} \\ \tilde{y} &= \dot{q} - \dot{q}_d = \dot{\tilde{q}},\end{aligned} \tag{4.10}$$

where $\tilde{q} = q - q_d$ denotes the position error of the joints, $\widetilde{\mathtt{P}} = \mathtt{P} - \mathtt{P}_d$ denotes the error of the canonical transform of generalized momenta and $\tilde{u} = u - u_d$ denotes the control input which should eradicate the state errors on the desired trajectory.

4.1.4 Error dynamics in the port-Hamiltonian Framework

To express the system in (4.10) in the pH structure again, PBC is applied. Based on (2.24), $\tilde{u}$ is defined as

$$\tilde{u} = \frac{\partial V}{\partial q}(q) - \frac{\partial V}{\partial q}(q_d) + \hat{u}, \tag{4.11}$$

such that the error dynamics are represented by

$$\begin{aligned}\begin{bmatrix} \dot{\tilde{q}} \\ \dot{\widetilde{\mathtt{P}}} \end{bmatrix} &= \begin{bmatrix} \mathbf{0}_{3\times 3} & \Psi(q) \\ -\Psi^\top(q) & \mathbf{0}_{3\times 3} \end{bmatrix} \begin{bmatrix} \frac{\partial \widetilde{H}}{\partial \tilde{q}}(\widetilde{\mathtt{P}}) \\ \frac{\partial \widetilde{H}}{\partial \widetilde{\mathtt{P}}}(\widetilde{\mathtt{P}}) \end{bmatrix} + \begin{bmatrix} \mathbf{0}_{3\times 3} \\ \Psi^\top(q) \end{bmatrix} \hat{u} \\ \tilde{y} &= \Psi(q)\frac{\partial \widetilde{H}}{\partial \widetilde{\mathtt{P}}}(\widetilde{\mathtt{P}}) = \dot{\tilde{q}},\end{aligned} \tag{4.12}$$

with the Hamiltonian

$$\widetilde{H}(\widetilde{\mathtt{P}}) = \frac{1}{2}\widetilde{\mathtt{P}}^\top \widetilde{\mathtt{P}}. \tag{4.13}$$

As discussed in Chapter 2, this system is passive and lossless, as it is expressed in the pH framework without damping. The passivity of the system is useful for the following control designs, since PBC for pH systems allows addressing complex problems in a structured way (Muñoz-Arias, 2015).

4.2 Trajectory tracking control

The aim of the control laws proposed in this section is to asymptotically stabilize the PERA on a desired trajectory. The control input on this desired trajectory is given by (4.9). However, due to disturbances and inaccuracies in the modeling, state errors can arise. To eradicate these errors, three control laws defining $\hat{u}$ are proposed in the coming subsections. The main purpose of the control laws is to asymptotically stabilize the error dynamics (4.12) to zero in the equilibrium, such that the states converge to the desired trajectory.

4.2.1 Passivity-Based Control

Here, a PBC strategy which GAS the origin of the error system is proposed. Damping is injected into the closed-loop system via the $K_d\dot{\tilde{q}}$ term in the control law. The control law proposed is structured as a PD-PBC law, since the control law consist of a term proportional to the position error (K_p) and a term proportional to the derivative of this error (K_d).

Theorem 4.1. Consider the error dynamics in (4.12). The control law

$$\hat{u} = -K_p\tilde{q} - K_d\dot{\tilde{q}}, \tag{4.14}$$

with $K_p,\ K_d \in \mathbb{R}^{3\times3},\ K_p = K_p^\top > 0$ and $K_d = K_d^\top > 0$, asymptotically stabilizes the system globally with the equilibrium $[\tilde{q}, \widetilde{\mathrm{P}}]^\top = (\mathbf{0}_3, \mathbf{0}_3)$.

Proof. Since

$$\dot{\tilde{q}} = \Psi(q)\widetilde{\mathrm{P}}, \tag{4.15}$$

the control law in (4.14) transforms system (4.12) into

$$\begin{aligned}\begin{bmatrix} \dot{\tilde{q}} \\ \dot{\widetilde{\mathrm{P}}} \end{bmatrix} &= \begin{bmatrix} \mathbf{0}_{3\times3} & \Psi(q) \\ -\Psi^\top(q) & -\Psi^\top(q)K_d\Psi(q) \end{bmatrix} \begin{bmatrix} \frac{\partial \widetilde{H}_d}{\partial \tilde{q}}(\tilde{q}, \widetilde{\mathrm{P}}) \\ \frac{\partial \widetilde{H}}{\partial \widetilde{\mathrm{P}}}(\tilde{q}, \widetilde{\mathrm{P}}) \end{bmatrix} \\ \tilde{y} &= \Psi(q)\frac{\partial \widetilde{H}}{\partial \widetilde{\mathrm{P}}}(\widetilde{\mathrm{P}}) = \dot{\tilde{q}}, \end{aligned} \tag{4.16}$$

with the Hamiltonian

$$\widetilde{H}_d(\tilde{q}, \widetilde{\mathrm{P}}) = \frac{1}{2}\widetilde{\mathrm{P}}^\top\widetilde{\mathrm{P}} + \frac{1}{2}\tilde{q}^\top K_p\tilde{q}. \tag{4.17}$$

The desired equilibrium of the system is $[\tilde{q}, \widetilde{\mathrm{P}}]_*^\top = (\mathbf{0}_3, \mathbf{0}_3)$. Then, the partial derivative of the Hamiltonian with respect to the states, evaluated at the desired equilibrium, is given by

$$\left[\nabla\widetilde{H}_d\right]_* = \begin{bmatrix} \frac{\partial \widetilde{H}_d}{\partial \tilde{q}}(\tilde{q}, \widetilde{\mathrm{P}}) \\ \frac{\partial \widetilde{H}_d}{\partial \widetilde{\mathrm{P}}}(\tilde{q}, \widetilde{\mathrm{P}}) \end{bmatrix}_* = \begin{bmatrix} K_p\tilde{q} \\ \widetilde{\mathrm{P}} \end{bmatrix}_* = \begin{bmatrix} \mathbf{0}_3 \\ \mathbf{0}_3 \end{bmatrix}, \tag{4.18}$$

while evaluation of the Hessian matrix yields

$$\left[\nabla^2\widetilde{H}_d\right] = \begin{bmatrix} \frac{\partial^2 \widetilde{H}_d}{\partial \tilde{q}^2} & \frac{\partial^2 \widetilde{H}_d}{\partial \tilde{q}\partial \widetilde{\mathrm{P}}} \\ \frac{\partial^2 \widetilde{H}_d}{\partial \widetilde{\mathrm{P}}\partial \tilde{q}} & \frac{\partial^2 \widetilde{H}_d}{\partial \widetilde{\mathrm{P}}^2} \end{bmatrix} = \begin{bmatrix} K_p & \mathbf{0}_{3\times3} \\ \mathbf{0}_{3\times3} & I_3 \end{bmatrix}, \tag{4.19}$$

which is positive definite and independent of the states. This implies that the closed-loop Hamiltonian has a minimum in the origin, i.e. $\operatorname{argmin}\left\{\widetilde{H}_d(\tilde{q}, \widetilde{\mathrm{P}})\right\} = \mathbf{0}_6$. Hence, and following from (2.6), the Hamiltonian is positive definite with respect to the equilibrium. On the other hand, the time derivative of the Hamiltonian function (4.17) is given by

$$\dot{\widetilde{H}}_d(\tilde{q}, \widetilde{\mathrm{P}}) = -\left(\frac{\partial \widetilde{H}_d}{\partial \widetilde{\mathrm{P}}}(\tilde{q}, \widetilde{\mathrm{P}})\right)^\top \Psi^\top(q)K_d\Psi(q)\left(\frac{\partial \widetilde{H}_d}{\partial \widetilde{\mathrm{P}}}(\tilde{q}, \widetilde{\mathrm{P}})\right) = -\dot{\tilde{q}}^\top K_d\dot{\tilde{q}} \le 0. \tag{4.20}$$

Hence, the desired equilibrium is stable in the sense of Lyapunov with the Lyapunov function $\widetilde{H}_d$. Asymptotic stability, however, cannot be proven with Lyapunov's second method, as the time derivative of the Lyapunov function is not negative definite relative to the equilibrium (condition iv of Theorem 2.1). Therefore, it is necessary to conduct another stability analysis; in this case, LaSalle's invariance principle is applied to prove asymptotic stability of the closed-loop system.

Let

$$\Omega := \left\{\tilde{q}, \widetilde{\mathrm{P}} \in \mathbb{R}^3 \mid \dot{\widetilde{H}}_d = 0\right\}. \tag{4.21}$$

Following from LaSalle's invariance principle, if a point can stay identically in Ω, it is a AS equilibrium of the system. Furthermore, since $\widetilde{H}_d$ is radially unbounded, the stability properties of the system are global. Recalling that the matrices K_d and $\Psi(q)$ are full rank, it follows from (4.20) that if $\dot{\widetilde{H}}_d = 0$,

$$\dot{\tilde{q}} \equiv \mathbf{0}_3 \Leftrightarrow \Psi\widetilde{\mathtt{P}} \equiv \mathbf{0}_3 \Leftrightarrow \widetilde{\mathtt{P}} \equiv \mathbf{0}_3.$$

Hence,

$$\widetilde{\mathtt{P}} \equiv \mathbf{0}_3 \implies \dot{\widetilde{\mathtt{P}}} \equiv \mathbf{0}_3 \Leftrightarrow -\Psi^\top K_p \tilde{q} - \cancelto{\mathbf{0}_3}{\Psi^\top(q) K_d \Psi(q)\widetilde{\mathtt{P}}} \equiv \mathbf{0}_3 \Leftrightarrow \Psi^\top K_p \tilde{q} \equiv \mathbf{0}_3 \Leftrightarrow \tilde{q} \equiv \mathbf{0}_3.$$

Therefore, $\dot{\widetilde{H}}_d \equiv 0$, if and only if,

$$\begin{aligned} \tilde{q} &\equiv \mathbf{0}_3 \\ \widetilde{\mathtt{P}} &\equiv \mathbf{0}_3. \end{aligned} \tag{4.22}$$

By LaSalle's invariance principle, the system is GAS with the equilibrium $[\tilde{q}, \widetilde{\mathtt{P}}]^\top = (\mathbf{0}_3, \mathbf{0}_3)$. QED

4.2.2 Control without velocity measurements

As discussed in Chapter 2, the PERA is not equipped with velocity sensors. Hence, in this subsection, the control law proposed in Theorem 4.1 is adapted to overcome this issue. The next theorem proposes a control law which allows stabilization of the system without the necessity of velocity measurements. In the method used here, proposed in Dirksz, Scherpen, and Ortega (2008), the dynamics of the system are extended by the introduction of a new, virtual state $x_c \in \mathbb{R}^3$, which is linearly related to the position errors. This state is used to inject damping into the closed-loop system (Wesselink, Borja, and Scherpen, 2018). As opposed to the method of Dirksz, Scherpen, and Ortega (2008), the control law proposed does not require any partial differential equations to be solved.

Theorem 4.2. Consider the error dynamics in (4.12). Define the dynamics of the new state x_c as

$$\dot{x}_c = -R_c\left(K_I z + K_c x_c\right), \tag{4.23}$$

with $z = \tilde{q} + x_c$, $R_c,\ K_I,\ K_c \in \mathbb{R}^{3\times 3}$, $R_c = R_c^\top > 0$, $K_I = K_I^\top > 0$ and $K_c = K_c^\top > 0$. Then, the control law

$$\hat{u} = -K_I z \tag{4.24}$$

renders the error system GAS with the equilibrium $[\tilde{q}, \widetilde{\mathtt{P}}, x_c]^\top = (\mathbf{0}_3, \mathbf{0}_3, \mathbf{0}_3)$.

Proof. The definitions in (4.23) and (4.24) transform system (4.12) into

$$\begin{aligned} \begin{bmatrix} \dot{\tilde{q}} \\ \dot{\widetilde{\mathtt{P}}} \\ \dot{x}_c \end{bmatrix} &= \begin{bmatrix} \mathbf{0}_{3\times3} & \Psi(q) & \mathbf{0}_{3\times3} \\ -\Psi^\top(q) & \mathbf{0}_{3\times3} & \mathbf{0}_{3\times3} \\ \mathbf{0}_{3\times3} & \mathbf{0}_{3\times3} & -R_c \end{bmatrix} \begin{bmatrix} \frac{\partial \widetilde{H}_d}{\partial \tilde{q}}(\tilde{q}, \widetilde{\mathtt{P}}, x_c) \\ \frac{\partial \widetilde{H}_d}{\partial \widetilde{\mathtt{P}}}(\tilde{q}, \widetilde{\mathtt{P}}, x_c) \\ \frac{\partial \widetilde{H}_d}{\partial x_c}(\tilde{q}, \widetilde{\mathtt{P}}, x_c) \end{bmatrix} \\ \tilde{y} &= \Psi(q)\frac{\partial \widetilde{H}_d}{\partial \widetilde{\mathtt{P}}}(\tilde{q}, \widetilde{\mathtt{P}}, x_c) = \dot{\tilde{q}}, \end{aligned} \tag{4.25}$$

with the Hamiltonian

$$\widetilde{H}_d(\tilde{q}, \widetilde{\mathsf{P}}, x_c) = \frac{1}{2} z^\top K_I z + \frac{1}{2} \mathsf{P}^\top \mathsf{P} + \frac{1}{2} x_c^\top K_c x_c. \tag{4.26}$$

The desired equilibrium of the system is $[\tilde{q}, \widetilde{\mathsf{P}}, x_c]_*^\top = (\mathbf{0}_3, \mathbf{0}_3, \mathbf{0}_3)$. Then, the partial derivative of the Hamiltonian with respect to the states, evaluated at the desired equilibrium, is given by

$$\left[\nabla \widetilde{H}_d\right]_* = \begin{bmatrix} \frac{\partial \widetilde{H}_d}{\partial \tilde{q}}(\tilde{q}, \widetilde{\mathsf{P}}, x_c) \\ \frac{\partial \widetilde{H}_d}{\partial \widetilde{\mathsf{P}}}(\tilde{q}, \widetilde{\mathsf{P}}, x_c) \\ \frac{\partial \widetilde{H}_d}{\partial x_c}(\tilde{q}, \widetilde{\mathsf{P}}, x_c) \end{bmatrix}_* = \begin{bmatrix} K_I z \\ \widetilde{\mathsf{P}} \\ K_I z + K_c x_c \end{bmatrix}_* = \begin{bmatrix} \mathbf{0}_3 \\ \mathbf{0}_3 \\ \mathbf{0}_3 \end{bmatrix}, \tag{4.27}$$

while evaluation of the Hessian matrix yields

$$\left[\nabla^2 \widetilde{H}_d\right] = \begin{bmatrix} \frac{\partial^2 \widetilde{H}_d}{\partial \tilde{q}^2} & \frac{\partial^2 \widetilde{H}_d}{\partial \tilde{q} \partial \widetilde{\mathsf{P}}} & \frac{\partial^2 \widetilde{H}_d}{\partial \tilde{q} \partial x_c} \\ \frac{\partial^2 \widetilde{H}_d}{\partial \widetilde{\mathsf{P}} \partial \tilde{q}} & \frac{\partial^2 \widetilde{H}_d}{\partial \widetilde{\mathsf{P}}^2} & \frac{\partial^2 \widetilde{H}_d}{\partial \widetilde{\mathsf{P}} \partial x_c} \\ \frac{\partial^2 \widetilde{H}_d}{\partial x_c \partial \tilde{q}} & \frac{\partial^2 \widetilde{H}_d}{\partial x_c \partial \widetilde{\mathsf{P}}} & \frac{\partial^2 \widetilde{H}_d}{\partial x_c^2} \end{bmatrix} = \begin{bmatrix} K_I & \mathbf{0}_{3\times3} & K_I \\ \mathbf{0}_{3\times3} & I_3 & \mathbf{0}_{3\times3} \\ K_I & \mathbf{0}_{3\times3} & K_I + K_c \end{bmatrix}, \tag{4.28}$$

which is positive definite and independent of the states. This implies that the closed-loop Hamiltonian has a minimum in the origin, i.e. $\operatorname{argmin}\left\{\widetilde{H}_d(\tilde{q}, \widetilde{\mathsf{P}})\right\} = \mathbf{0}_6$. Hence, and following from (2.6), the Hamiltonian is positive definite with respect to the equilibrium. Furthermore, the time derivative of the Hamiltonian function (4.26) is given by

$$\dot{\widetilde{H}}_d(\tilde{q}, \widetilde{\mathsf{P}}, x_c) = -\left(\frac{\partial \widetilde{H}_d}{\partial x_c}(\tilde{q}, \widetilde{\mathsf{P}}, x_c)\right)^\top R_c \left(\frac{\partial \widetilde{H}_d}{\partial x_c}(\tilde{q}, \widetilde{\mathsf{P}}, x_c)\right) \leq 0. \tag{4.29}$$

Therefore, the desired equilibrium is stable in the sense of Lyapunov with the Lyapunov function $\widetilde{H}_d$. Asymptotic stability, however, cannot be proven with Lyapunov's second method, as the time derivative of the Lyapunov function is not negative definite relative to the equilibrium (condition iv of Theorem 2.1). Therefore, it is necessary to conduct another stability analysis; again, LaSalle's invariance principle is applied to prove asymptotic stability of the closed-loop system.

Let

$$\Omega := \left\{\tilde{q}, \widetilde{\mathsf{P}}, x_c \in \mathbb{R}^3 \;\middle|\; \dot{\widetilde{H}}_d = 0\right\}. \tag{4.30}$$

Following from LaSalle's invariance principle, if a point can stay identically in Ω, it is a AS equilibrium of the system. moreover, since $\widetilde{H}_d$ is radially unbounded, the stability properties of the system are global. Recalling that the matrices K_I, K_c, R_c and $\Psi(q)$ are full rank, it follows from (4.29) that if $\dot{\widetilde{H}}_d = 0$,

$$\frac{\partial \widetilde{H}_d}{\partial x_c} \equiv \mathbf{0}_3.$$

Following from the dynamics of x_c, this implies that

$$\dot{x}_c \equiv \mathbf{0}_3 \implies \frac{d}{dt}(K_I z + K_c x_c) = K_I \dot{z} + K_c \cancelto{\mathbf{0}_3}{\dot{x}_c} \equiv \mathbf{0}_3 \Leftrightarrow \dot{z} \equiv \mathbf{0}_3.$$

From the definition of z, it follows that

$$\dot{z} \equiv \dot{\tilde{q}} + \cancelto{\mathbf{0}_3}{\dot{x}_c} \Leftrightarrow \dot{\tilde{q}} \equiv \mathbf{0}_3 \Leftrightarrow \Psi(q)\widetilde{\mathtt{P}} \equiv \mathbf{0}_3 \Leftrightarrow \widetilde{\mathtt{P}} \equiv \mathbf{0}_3.$$

Therefore,

$$\widetilde{\mathtt{P}} \equiv \mathbf{0}_3 \implies \dot{\widetilde{\mathtt{P}}} \equiv \mathbf{0}_3 \Leftrightarrow -\Psi(q)^\top K_I z \equiv \mathbf{0}_3 \Leftrightarrow z \equiv \mathbf{0}_3.$$

In the dynamics of x_c, this renders

$$\dot{x}_c = R_c\left(\cancelto{\mathbf{0}_3}{K_I z} + K_c x_c\right) \equiv \mathbf{0}_3 \Leftrightarrow x_c \equiv \mathbf{0}_3,$$

which, by the definition of z, implies

$$z = \tilde{q} + \cancelto{\mathbf{0}_3}{x_c} \equiv \mathbf{0}_3 \Leftrightarrow \tilde{q} \equiv \mathbf{0}_3.$$

Therefore, $\dot{\tilde{H}}_d \equiv 0$, if and only if,

$$\begin{aligned} \tilde{q} &\equiv \mathbf{0}_3 \\ \widetilde{\mathtt{P}} &\equiv \mathbf{0}_3 \\ x_c &\equiv \mathbf{0}_3. \end{aligned} \tag{4.31}$$

By LaSalle's invariance principle, the system is GAS with the equilibrium $[\tilde{q}, \widetilde{\mathtt{P}}]^\top = (\mathbf{0}_3, \mathbf{0}_3, \mathbf{0}_3)$. QED

4.2.3 Saturated control without velocity measurements

In the original controller code of the PERA, the input signal from the PD control strategy is saturated at the limits provided in (3.11) and (3.12). However, input signal saturation is known to be a source of performance degeneration (Ma and Yang, 2008). Therefore, the control law in Theorem 4.2 was adapted such that it becomes saturated itself. Based on the work of van den Bos (2019), it is expected that this control law performs better than the one proposed in Theorem 4.2. The resulting saturated control law which renders the error dynamics stable in the zero equilibrium is proposed in the following theorem.

Theorem 4.3. Consider the error dynamics in (4.12). Define a new state $x_c \in \mathbb{R}^3$ with the dynamics

$$\dot{x}_c = -R_c\left(\sum_{i=1}^{3} e_i \alpha_i \tanh(\beta_i z_i) + K_c x_c\right), \tag{4.32}$$

with $z = \tilde{q} + x_c$, $R_c,\ K_c \in \mathbb{R}^{3\times 3}$, $R_c = R_c^\top > 0$, $K_c = K_c^\top > 0$ and $\alpha_i, \beta_i > 0$. Then the saturated control law

$$\hat{u} = -\sum_{i=1}^{3} e_i \alpha_i \tanh(\beta_i z_i) \tag{4.33}$$

renders the error system GAS with the equilibrium in $[\tilde{q}, \widetilde{\mathtt{P}}, x_c]^\top = (\mathbf{0}_3, \mathbf{0}_3, \mathbf{0}_3)$.

Proof. The definitions in (4.32) and (4.33) transform system (4.12) into the closed-loop system

$$\begin{bmatrix} \dot{\tilde{q}} \\ \dot{\widetilde{\mathtt{P}}} \\ \dot{x}_c \end{bmatrix} = \begin{bmatrix} \mathbf{0}_{3\times 3} & \Psi(q) & \mathbf{0}_{3\times 3} \\ -\Psi^\top(q) & \mathbf{0}_{3\times 3} & \mathbf{0}_{3\times 3} \\ \mathbf{0}_{3\times 3} & \mathbf{0}_{3\times 3} & -R_c \end{bmatrix} \begin{bmatrix} \frac{\partial \widetilde{H}_d}{\partial \tilde{q}}(\tilde{q}, \widetilde{\mathtt{P}}, x_c) \\ \frac{\partial \widetilde{H}_d}{\partial \widetilde{\mathtt{P}}}(\tilde{q}, \widetilde{\mathtt{P}}, x_c) \\ \frac{\partial \widetilde{H}_d}{\partial x_c}(\tilde{q}, \widetilde{\mathtt{P}}, x_c) \end{bmatrix} \tag{4.34}$$

$$\tilde{y} = \Psi(q) \frac{\partial \widetilde{H}_d}{\partial \widetilde{\mathtt{P}}}(\tilde{q}, \widetilde{\mathtt{P}}, x_c) = \dot{\tilde{q}},$$

with the Hamiltonian

$$\widetilde{H}_d(\tilde{q}, \widetilde{\mathtt{P}}, x_c) = \sum_{i=1}^{3} \frac{a_i}{\beta_i} \ln\left(\cosh\left(\beta_i z_i\right)\right) + \frac{1}{2} \mathtt{P}^\top \mathtt{P} + \frac{1}{2} x_c^\top K_c x_c. \tag{4.35}$$

The desired equilibrium of the system is $[\tilde{q}, \widetilde{\mathtt{P}}, x_c]_*^\top = (\mathbf{0}_3, \mathbf{0}_3, \mathbf{0}_3)$. Then, the partial derivative of the Hamiltonian with respect to the states, evaluated at the desired equilibrium, is given by

$$\left[\nabla \widetilde{H}_d\right]_* = \begin{bmatrix} \frac{\partial \widetilde{H}_d}{\partial \tilde{q}}(\tilde{q}, \widetilde{\mathtt{P}}, x_c) \\ \frac{\partial \widetilde{H}_d}{\partial \widetilde{\mathtt{P}}}(\tilde{q}, \widetilde{\mathtt{P}}, x_c) \\ \frac{\partial \widetilde{H}_d}{\partial x_c}(\tilde{q}, \widetilde{\mathtt{P}}, x_c) \end{bmatrix}_* = \begin{bmatrix} \sum_{i=1}^{3} e_i \alpha_i \tanh\left(\beta_i z_i\right) \\ \widetilde{\mathtt{P}} \\ \sum_{i=1}^{3} e_i \alpha_i \tanh\left(\beta_i z_i\right) + K_c x_c \end{bmatrix}_* = \begin{bmatrix} \mathbf{0}_3 \\ \mathbf{0}_3 \\ \mathbf{0}_3 \end{bmatrix}, \tag{4.36}$$

while evaluation of the Hessian matrix yields

$$\nabla^2 \widetilde{H}_d = \begin{bmatrix} \sum_{i=1}^{3} e_i e_i^\top \alpha_i \beta_i \left[1 - \tanh^2\left(\beta_i z_i\right)\right] & \mathbf{0}_{3\times 3} & \sum_{i=1}^{3} e_i e_i^\top \alpha_i \beta_i \left[1 - \tanh^2\left(\beta_i z_i\right)\right] \\ \mathbf{0}_{3\times 3} & I_3 & \mathbf{0}_{3\times 3} \\ \sum_{i=1}^{3} e_i e_i^\top \alpha_i \beta_i \left[1 - \tanh^2\left(\beta_i z_i\right)\right] & \mathbf{0}_{3\times 3} & \sum_{i=1}^{3} e_i e_i^\top \alpha_i \beta_i \left[1 - \tanh^2\left(\beta_i z_i\right)\right] + K_c \end{bmatrix}, \tag{4.37}$$

such that, at the desired equilibrium, the Hessian becomes

$$\left[\nabla^2 \widetilde{H}_d\right]_* = \begin{bmatrix} \sum_{i=1}^{3} e_i e_i^\top \alpha_i \beta_i & \mathbf{0}_{3\times 3} & \sum_{i=1}^{3} e_i e_i^\top \alpha_i \beta_i \\ \mathbf{0}_{3\times 3} & I_3 & \mathbf{0}_{3\times 3} \\ \sum_{i=1}^{3} e_i e_i^\top \alpha_i \beta_i & \mathbf{0}_{3\times 3} & \sum_{i=1}^{3} e_i e_i^\top \alpha_i \beta_i + K_c \end{bmatrix}. \tag{4.38}$$

Following from (4.37) and (4.38), the Hessian matrix is positive definite and has its maximum located in the desired equilibrium. This implies that the closed-loop Hamiltonian has a minimum in the origin, i.e. argmin $\left\{\widetilde{H}_d(\tilde{q}, \widetilde{\mathtt{P}})\right\} = \mathbf{0}_6$. Therefore, and following from (2.6), the Hamiltonian is positive definite with respect to the equilibrium. Moreover, the time derivative of the Hamiltonian function (4.35) is given by

$$\dot{\widetilde{H}}_d(\tilde{q}, \widetilde{\mathtt{P}}, x_c) = -\left(\frac{\partial \widetilde{H}_d}{\partial x_c}(\tilde{q}, \widetilde{\mathtt{P}}, x_c)\right)^\top R_c \left(\frac{\partial \widetilde{H}_d}{\partial x_c}(\tilde{q}, \widetilde{\mathtt{P}}, x_c)\right) \leq 0. \tag{4.39}$$

Hence, the desired equilibrium is stable in the sense of Lyapunov with the Lyapunov function $\widetilde{H}_d$. Asymptotic stability, however, cannot be proven with Lyapunov's second method, as the time derivative of the Lyapunov function is not negative definite relative to the equilibrium (condition iv of Theorem 2.1). Hence, it is necessary to conduct another stability analysis. Once more, LaSalle's invariance principle is applied to prove asymptotic stability of the closed-loop system.

Let

$$\Omega := \left\{ \tilde{q}, \widetilde{\mathtt{P}}, x_c \in \mathbb{R}^3 \;\middle|\; \dot{\widetilde{H}}_d = 0 \right\}. \tag{4.40}$$

Following from LaSalle's invariance principle, if a point can stay identically in Ω, it is a AS equilibrium of the system. Moreover, since $\widetilde{H}_d$ is radially unbounded, the stability properties of the system are global. Recalling that the matrices K_c, R_c and $\Psi(q)$ are full rank, it follows from (4.39) that if $\dot{\widetilde{H}}_d = 0$,

$$\frac{\partial \widetilde{H}_d}{\partial x_c} \equiv \mathbf{0}_3.$$

Following from the dynamics of x_c, this implies that

$$\begin{aligned} \dot{x}_c \equiv \mathbf{0}_3 \implies & \frac{d}{dt}\left(\sum_{i=1}^{3} e_i \alpha_i \tanh\left(\beta_i z_i\right) + K_c x_c \right) \\ &= \underbrace{\left(\sum_{i=1}^{3} e_i e_i^\top \alpha_i \beta_i \left[1 - \tanh^2\left(\beta_i z_i\right)\right] \right)}_{>0} \dot{z} + K_c \cancelto{\mathbf{0}_3}{\dot{x}_c} \equiv \mathbf{0}_3 \Leftrightarrow \dot{z} \equiv \mathbf{0}_3. \end{aligned}$$

From the definition of z, it follows that

$$\dot{z} \equiv \dot{\tilde{q}} + \cancelto{\mathbf{0}_3}{\dot{x}_c} \Leftrightarrow \dot{\tilde{q}} \equiv \mathbf{0}_3 \Leftrightarrow \Psi(q)\widetilde{\mathtt{P}} \equiv \mathbf{0}_3 \Leftrightarrow \widetilde{\mathtt{P}} \equiv \mathbf{0}_3.$$

Therefore,

$$\widetilde{\mathtt{P}} \equiv \mathbf{0}_3 \implies \dot{\widetilde{\mathtt{P}}} \equiv \mathbf{0}_3 \Leftrightarrow -\Psi(q)^\top \sum_{i=1}^{3} e_i \alpha_i \tanh\left(\beta_i z_i\right) \equiv \mathbf{0}_3 \Leftrightarrow z \equiv \mathbf{0}_3.$$

In the dynamics of x_c, this renders

$$\dot{x}_c = R_c \left(\cancelto{\mathbf{0}_3}{\sum_{i=1}^{3} e_i \alpha_i \tanh\left(\beta_i z_i\right)} + K_c x_c \right) \equiv \mathbf{0}_3 \Leftrightarrow x_c \equiv \mathbf{0}_3,$$

which, by the definition of z, implies

$$z = \tilde{q} + \cancelto{\mathbf{0}_3}{x_c} = \mathbf{0}_3 \Leftrightarrow \tilde{q} \equiv \mathbf{0}_3.$$

Therefore, $\dot{\widetilde{H}}_d \equiv 0$, if and only if,

$$\begin{aligned} \tilde{q} &\equiv \mathbf{0}_3 \\ \widetilde{\mathtt{P}} &\equiv \mathbf{0}_3 \\ x_c &\equiv \mathbf{0}_3. \end{aligned} \tag{4.41}$$

By LaSalle's invariance principle, the system is GAS with the equilibrium $[\tilde{q}, \widetilde{\mathtt{P}}]^\top = (\mathbf{0}_3, \mathbf{0}_3, \mathbf{0}_3)$. QED

4.3 PERA control

4.3.1 Joint control

In the experiments, the control law proposed in Theorem 4.3 is used to stabilize the error dynamics of the trajectory. The total torque that should be exerted on the joints follows from the definition of $\tilde{u}$, (4.9), (4.11) and (4.33) and is given by

$$u = \frac{\partial V}{\partial q}(q) + \Psi^{-\top}(q_d)\frac{d\Psi^{-1}(q_d)\dot{q}_d}{dt} - \sum_{i=1}^{3} e_i \alpha_i \tanh\left(\beta_i z_i\right). \tag{4.42}$$

The control law above can be physically interpreted as follows. The gradient of the potential energy with respect to the joint positions compensates for the gravitational forces acting on the PERA. The second term can be seen as the desired torques on the joints if there are no gravitational forces acting on the joints and there are no errors in the joint positions. The final term in (4.42) eliminates the state errors in the system.

The values of α should be designed such that the control input abides by the saturation limits in (3.14). The maximum allowable values of α depend on the maximum and minimum of the first two terms of (4.42).

In the code for the PERA, the desired torque is found with control law (4.42), which is then transformed into a signal in counts as in (3.10) and (3.13). In the next chapter, this control strategy is tested on the PERA.

4.3.2 Gripper control

For the application of the trajectory tracking control in the coming chapter, the gripper is required to hold the marker tight. Therefore, the input to the gripper motor is set to the a constant positive signal, i.e.

$$u_{counts,G} = 18000. \tag{4.43}$$

Setting the input to the gripper motor to this level ensures that the marker is held tight, while the maximum continuous current over the motor is not exceeded (see Appendix B).

Chapter 5

Results and discussion

This chapter aims to validate the controllers developed in Chapter 4, and discuss the corresponding results. First, the desired trajectory is defined, such that the end-effector of the PERA follows the path of a circle in the Cartesian space. Second, the control law proposed in Theorem 4.3 is applied to the mathematical model of the PERA in simulations, with the desired trajectory which was defined beforehand. From the simulations, the control strategy is taken and step by step implemented into the physical PERA. When the performance of the control strategy is deemed sufficiently successful, the strategy is compared with the non-saturated version proposed in Theorem 4.2. Next, the controllers are implemented to perform a 'drawing routine'. Furthermore, other trajectories are applied to the control law, to verify the performance of the control law on other trajectories. Moreover, a heuristic approach is proposed to enhance the quality of the drawings produced by the PERA. Finally, the chapter concludes with the extension of the system to five DoF, allowing control over the orientation of the marker with respect to the canvas.

5.1 Desired trajectory

The controller proposed in Theorem 4.3 is validated by letting the end-effector of the PERA follow the path of a circle. The final application of this experiment is to let the gripper hold a marker, such that the PERA can draw a circle on a canvas which is placed upright and in front of the PERA (normal to the X-axis in the Cartesian space). To this end, we let the first joint remain in the zero position, while the second and third joints follow a sine and cosine trajectory relative to the position shown in Figure 3.2, respectively. As a result, the desired trajectory becomes

$$q_d = \begin{bmatrix} q_{d,1} \\ q_{d,2} \\ q_{d,3} \end{bmatrix} = \begin{bmatrix} 0 \\ \arcsin\left(\frac{r}{L_2}\right)\sin\left(\frac{2\pi}{T}t\right) \\ \frac{\pi}{2} - \arcsin\left(\frac{r}{L_2}\right)\cos\left(\frac{2\pi}{T}t\right) \end{bmatrix} \tag{5.1}$$

with $r \in \mathbb{R}_+$ the radius of the circle, $T \in \mathbb{R}_+$ the period of the circle trajectory and $t \in \mathbb{R}_+$ the time. Substituting the value of L_2 and setting $T = 15$ $[s]$ and $r = 0.2$ $[m]$ yields

$$q_d \approx \begin{bmatrix} 0 \\ 0.43\sin(0.42t) \\ 1.57 - 0.43\cos(0.42t) \end{bmatrix}. \tag{5.2}$$

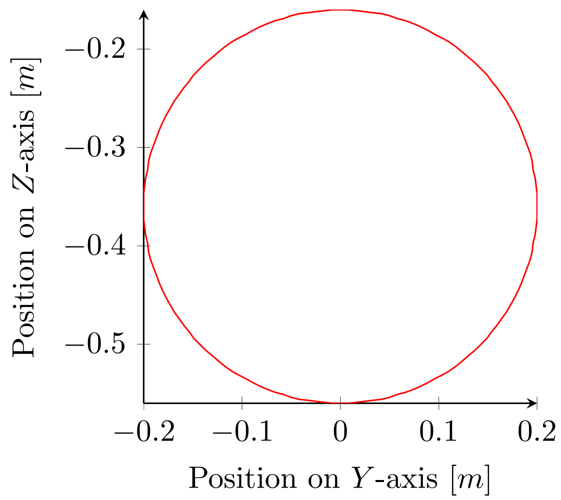

Figure 5.1: Cartesian y- and z-coordinates of the desired circle trajectory of the end-effector of the PERA in the plane $x = 0.44$

If this trajectory is followed precisely, this would allow the PERA to draw a circle with the Cartesian coordinates (Stover and Weisstein, n.d.)

$$x = \sqrt{L_2^2 - r^2} \approx 0.44 \tag{5.3}$$

$$y = r \sin\left(\frac{2\pi}{T}t\right) \approx 0.2 \sin(0.42t) \tag{5.4}$$

$$z = -L_1 - r\cos\left(\frac{2\pi}{T}t\right) \approx 0.36 - 0.2\cos(0.42t)\,. \tag{5.5}$$

The circle, in Cartesian coordinates, is depicted in Figure 5.1

The desired trajectory of the PERA is visualized using MATLAB® and the Robotic Toolbox developed by Corke et al. (1996) (see Appendix C for the script). The result is in Figure 5.2, where the red line is the path to be followed by the end-effector.

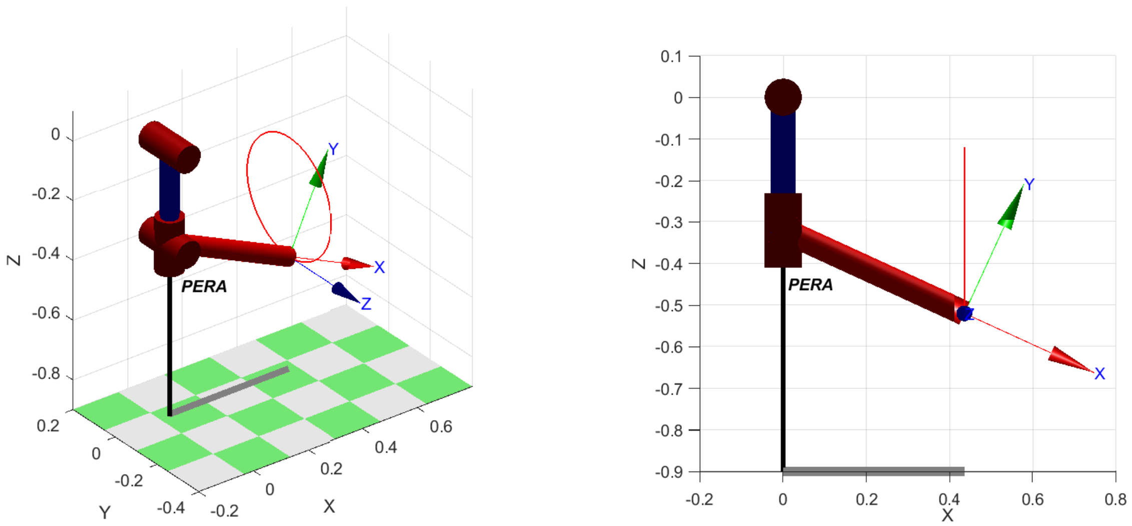

(a) 3D view

(b) Side view

Figure 5.2: Visualization of the desired trajectory of the PERA

Following from (4.4) and (5.2), the second term of the control law (4.42), which can be seen as the desired input when there are no position errors, gravitational forces or damping, becomes

$$\Psi^{-\top}(q_d)\frac{d\Psi^{-1}(q_d)\dot{q}_d}{dt} = \begin{bmatrix} 0.0015\cos(0.42t) \\ -0.032\sin(0.42t) \\ 0.0015\cos(0.42t) \end{bmatrix}. \tag{5.6}$$

This term induces the desired frictionless acceleration of the joints. Due to the large period of the desired trajectory, the magnitude of this term is relatively small compared to the other terms in the control law. Based on (3.6) and (5.6), the values of α should be selected according to

$$\alpha = \begin{bmatrix} \alpha_1 \\ \alpha_2 \\ \alpha_3 \end{bmatrix} \leq \begin{bmatrix} 11.03 \\ 1.71 \\ 6.15 \end{bmatrix}, \tag{5.7}$$

such that saturation of the control law (4.42) within the limits in (3.14) is ensured.

5.2 Simulations

Before testing the controller on the actual PERA system, simulations are preformed to verify the stability of the controller first. Tuning of the controller gains plays an important role in obtaining the desired performance of the closed-loop system. Since the number of gains to be tuned is quite large (α, β, K_c, R_c), some simplifications are made. First of all, the values of α are set slightly lower than their limits, i.e.

$$\alpha = \begin{bmatrix} 11.0 \\ 1.7 \\ 6.0 \end{bmatrix}. \tag{5.8}$$

Furthermore, the gain matrices K_c and R_c are set to be diagonal matrices to limit the amount of gains to tune.

To determine a starting point for the manual tuning of the controller, Lyapunov's first method is used. A tuning loop is designed in MATLAB®, such that the real parts of the poles of the linearized closed-loop system around the equilibrium are all strictly negative, ensuring stability near the equilibrium. The tuning loop can be found in Appendix D. From this starting point, simulations were preformed in Simulink®, using the mathematical model (4.2) with the control law (4.42). The model used for the simulations can be found in Appendix E. By further tuning of the controller using trial and error, the desired results were obtained.

The main finding from the tuning is that the value of β should be sufficiently large to ensure a fast response of the controller; when the values of β are too small, oscillations occur in the error of the positions. Furthermore, it is found that the tuning of the diagonal elements of the matrices K_c and R_c is a very delicate procedure; by trial and error the controller is tuned to the desired performance, but this is a time-consuming and difficult task.

The final controller gains selected for the simulations is given by

$$\alpha = \begin{bmatrix} 11.0 \\ 1.7 \\ 6.0 \end{bmatrix} \quad \beta = \begin{bmatrix} 40 \\ 30 \\ 30 \end{bmatrix} \quad K_c = \mathrm{diag}\{1,\ 2,\ 0.1\} \quad R_c = \mathrm{diag}\{0.4,\ 0.11,\ 0.5\}. \tag{5.9}$$

Simulations are performed using these controller gains and the initial position of the PERA set as the downward position, $q_0 = \mathbf{0}_3$. Furthermore, the initial time is set to zero, i.e. $t_0 = 0$. The results of the simulation are plotted in Figure 5.3.

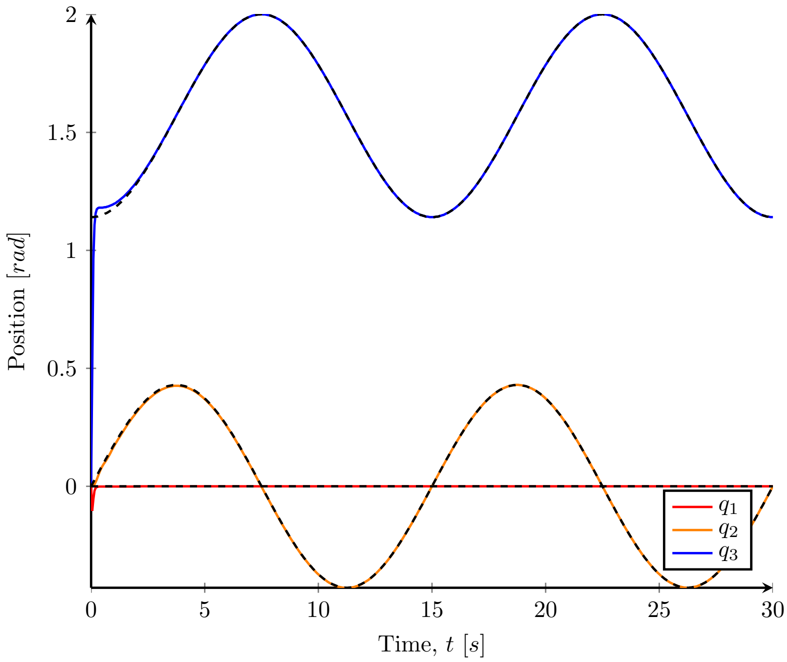

Figure 5.3: Simulation results. The colored lines represent the position of the joints during the simulation. The dashed lines represent the desired positions.

The figure shows that the convergence to the trajectory is successful and fast. To allow a better observation of the start of the simulation, Figure 5.3 was zoomed into to obtain Figure 5.4. It becomes clear that, although there is some undesired movement of the joints as a result of the trajectory initiation, the simulations converge to the desired trajectory smoothly. The peak in the response of the shoulder pitch joint (q_1) is caused by the force on this joint, resulting from the motion of the elbow pitch joint (q_3).

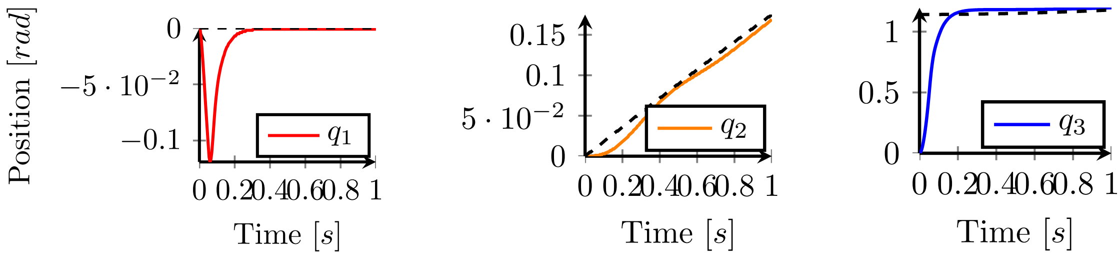

Figure 5.4: First second of the simulation results

These results are inserted into the visualization script (Appendix C) to observe the trajectory followed by the end-effector of the PERA in the simulations. As can be seen in the resulting figure (Figure 5.5), the model indeed converges to the desired trajectory (Figure 5.2).

From these results, it can be concluded that the selected control law theoretically stabilizes the system on the desired trajectory. Convergence is achieved well within one second, and the overshoot of the elbow pitch joint (q_3) is small and rapidly rejected. The first joint shows a response to the strong motion of the third joint during the start of the trajectory, but this disturbance is rapidly rejected as well.

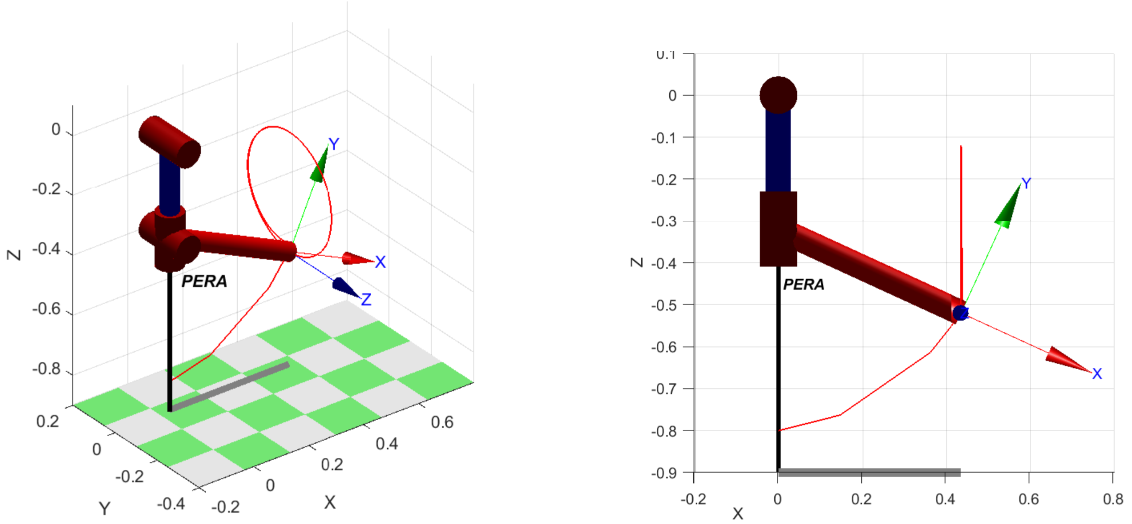

(a) 3D view (b) Side view

Figure 5.5: Visualization of the simulated trajectory of the PERA

5.3 Experiments

By conducting experiments, the control law (4.42) is verified in a real environment. This is done in several steps. First, the gravity compensation of the control law is verified. Second, SPR is preformed. Next, trajectory tracking is performed on the desired trajectory of a circle. Using these results, a canvas is placed such that the PERA draws a circle. Finally, other trajectories are considered, the drawing routine is enhanced by proposing a heuristic approach, and the orientation of the end-effector is considerd.

5.3.1 Gravity compensation

In the first experiments, the potential energy of the PERA as specified in (3.6) was verified. The partial derivative of the potential energy with respect to the positions acts as a gravity compensator for the system. Therefore, (3.6) can be verified by using only the first term of (4.42) as the control law, such that

$$u = \frac{\partial V}{\partial q}(q). \tag{5.10}$$

If the potential energy is correct, the gravity will be compensated by the input, resulting in the PERA standing still, i.e. $q = q_0$. To test this, the PERA was manually moved to various random initial positions before the controller was activated. With the control law activated, there was no motion from the initial position. This confirms the gravity compensation by the control law, which implies that the determined potential energy is correct.

5.3.2 Set Point Regulation

Next, following in the footsteps of van den Bos (2019), SPR was performed with the PERA to further verify the modeling of the system. The goal of SPR indicates that the desired velocities of the joints are equal to zero, such that the second term of the control law (4.42) is equal to zero, i.e.

$$u = \frac{\partial V}{\partial q}(q) - \sum_{i=1}^{3} e_i \alpha_i \tanh\left(\beta_i z_i\right). \tag{5.11}$$

In this experiment, it was found that the control law (5.11) works for SPR, as was previously determined in van den Bos (2019). However, the control law renders a steady-state error. By tuning of the controller, this steady-state error can be reduced, but not fully eradicated. Furthermore, it was found in the SPR experiments that the tuning from simulations did not return the desired results in the experiments. When manually tuning the control law, one particularly interesting feature of the tuning was found; to obtain a smooth motion (meaning no large overshoot or oscillations) from the initial position to steady-state, the value of β should not be too large, especially not when the initial error is relatively large. However, for the steady-state error to be as small as possible, the value of β should be large, such the input signal arising from the error is sufficiently large.

This finding poses an issue for the tracking of the desired trajectory (5.2) from the initial position, since the initial error of the elbow pitch joint would be rather large ($\tilde{q}_3 \approx 1.14\ rad$). Therefore, the PERA is initialized in a point close to the starting point of the trajectory, using SPR. During the first five seconds of the experiment, the desired positions are defined as

$$q_d = \begin{bmatrix} 0 \\ 0 \\ 1.14\sin(0.31t) \end{bmatrix}, \tag{5.12}$$

such that at time $t = 5$, the PERA is initialized in

$$q_0 \approx \begin{bmatrix} 0 \\ 0 \\ 1.14 \end{bmatrix}. \tag{5.13}$$

Because the desired position of the elbow pitch joint changes from zero to 1.14 with time, the position error is never large and the value of β can be set to a large value without causing oscillations or large overshoots. At time $t = 5$, the virtual state is set to $x_c = \mathbf{0}_3$, such that the system is initialized in the desired starting position.

5.3.3 Trajectory tracking

Finally, the trajectory tracking experiments were conducted, aiming to track the desired trajectory (5.2). As a starting point, the gains obtained in simulations and SPR experiments were used. However, several issues arised, e.g., the input signal to the shoulder yaw joint (q_2), was not strong enough to let the joint follow the trajectory at the desired velocity. This was caused by the factor α_2, which should be tuned at a higher value to make the shoulder yaw joint converge to the trajectory. On the other hand, increasing the value of α_2 would violate the limits on α in (5.7), which secure the saturation in (3.12). However, it is known that the initial position of the shoulder pitch joint is approximately equal to zero, while the desired position of this joint is equal to zero, i.e. $q_{2,0} \approx q_{2,d} = 0$. This indicates that the magnitude of the gravity compensation ((3.6)) for the shoulder yaw joint remains well below its maximum during the experiment, since the second element of the gravity compensation is equal to zero when the position of the shoulder pitch joint is equal to zero. Therefore, the value of α can be slightly increased in the experiments without jeopardizing the saturation limits of the motors.

Another issue arised in the motion of the the elbow pitch joint (q_3) of the PERA. The joint expressed a shaking behaviour, which can be seen as oscillations of the joint about the desired trajectory. In an attempt to follow the desired trajectory using the original PD control strategy of the PERA, it was determined that the shaking was also present in this experiment. This indicates that the shaking was not caused by the control law used, but by the hardware of the PERA. Presumably, the shaking was caused by either the natural damping of the PERA, looseness in the gearing, or hysteresis in the sensor measurements. By extensive tuning of the controller gains and increasing the sampling rate of the control loop from 100 $[Hz]$ to 200 $[Hz]$, the shaking of the joint was eradicated. The oscillations are still present in the input signal, but they are not (visibly) carried through to the movement of the joint. It should be mentioned that this tuning eradicates the shaking only on the desired trajectory. A different trajectory may require a different tuning. For example, during the initialization of the PERA, the elbow pitch joint does express the shaking behaviour (see Figure 5.7).

The final controller gains selected in the experiments is given by

$$\alpha = \begin{bmatrix} 11.0 \\ 2.0 \\ 6.0 \end{bmatrix} \qquad \beta = \begin{bmatrix} 400 \\ 100 \\ 120 \end{bmatrix}$$
$$K_c = \text{diag}\{30,\ 20,\ 200\} \qquad R_c = \text{diag}\{0.0001,\ 0.00001,\ 0.45\}. \tag{5.14}$$

This tuning was selected to obtain the desired performance while removing the shaking from the motion of the elbow joint. In the experiments, SPR is preformed in the first five seconds to initialize the PERA. After that, the value of the new state x_c is set to $x_c = \mathbf{0}_3$ and the trajectory is initiated. The results are plotted in Figure 5.6. The results show that the PERA stabilizes on the desired trajectory successfully.

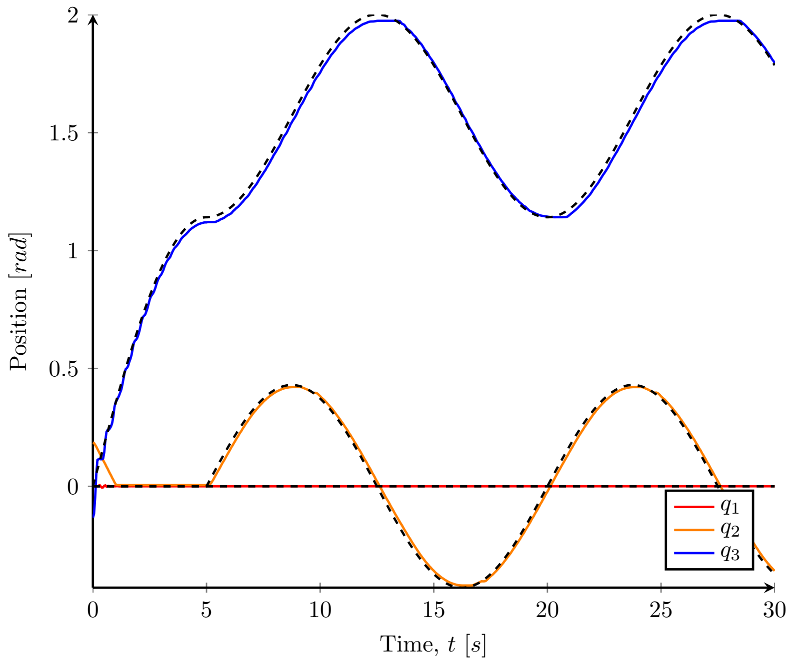

Figure 5.6: Experimental results. The colored lines represent the position of the joints during the experiment. The dashed lines represent the desired positions.

By zooming in to the first two seconds of the experiment, it is found that convergence is fast (Figure 5.7). Furthermore, by observing the position errors in Figure 5.8, it is found that the PERA follows the desired trajectory closely in steady-state; for the two joints that make the major motions (q_2 and q_3), the absolute position error remains smaller than 0.05 $[rad]$, i.e. $|\tilde{q}| < 0.05$.

Figure 5.9 depicts the input to the motors during the experiments. Obviously, the input signals match the motion of the joints in Figure 5.6. Moreover, the figure shows oscillations in the input signal of the elbow pitch joint (q_3), especially when the motion of the joint is downward, i.e. along the direction of gravity. These oscillations are what remains of the previously discussed shaking of the joint. As opposed to the shaking, the oscillations in the input signal could not be eradicated by tuning of the controller.

For the sake of visualization of the trajectory followed by the PERA in the experiments, the data obtained in the experiments were plugged into the visualization script (Appendix C). Comparison of Figure 5.10 and Figure 5.2 confirms that the trajectory covered is approximately equal to the desired trajectory.

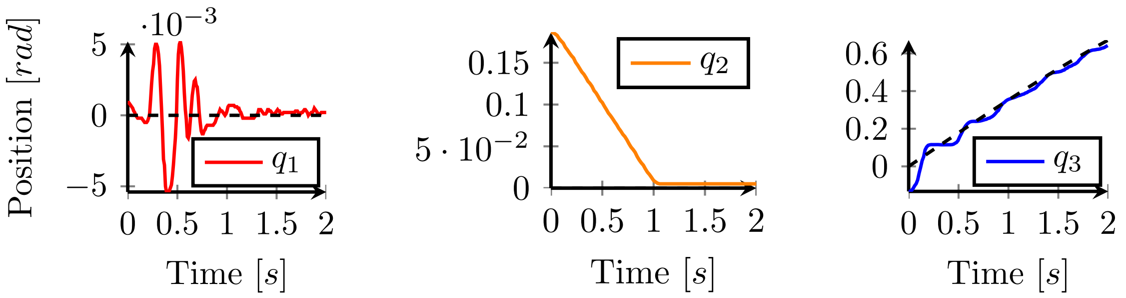

Figure 5.7: First two seconds of the experimental results

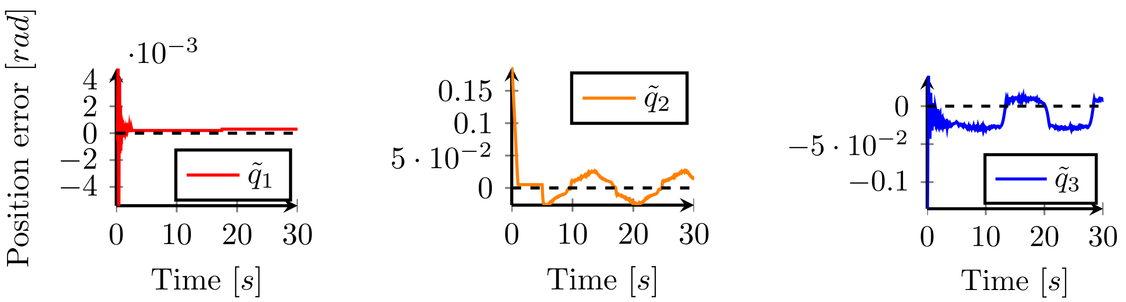

Figure 5.8: Position errors in the experiment

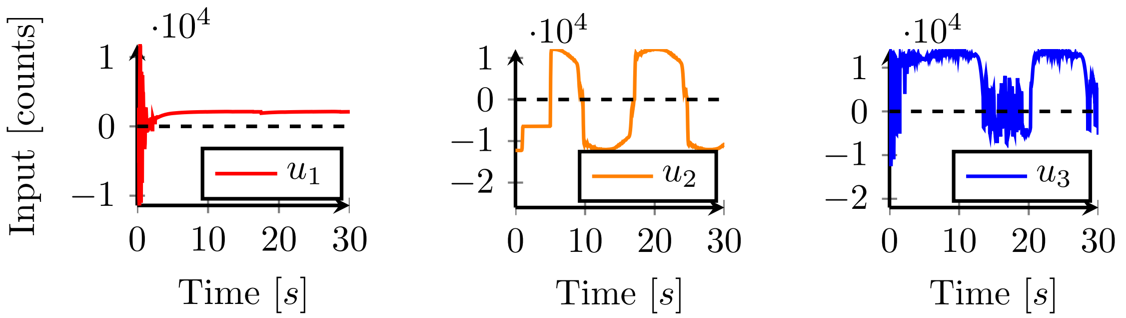

Figure 5.9: Input signals in the experiment

From the experiments it becomes clear that there exists a steady-state error in the joint positions. This steady-state error could presumably be reduced by using an integral term in the control law. However, introducing a integral term has some drawbacks. Most importantly, the introduction of an integral term would cause the pH structure of the closed-loop system to be lost, such that the system can only be proven locally AS by Lyapunov's first method (van den Bos, 2019). Moreover, the introduction of an integral term may cause large overshoots, oscillations or slower response of the controller (Albertos et al., 1997). Since the steady-state errors are reasonably small, it is decided not to use an integral term in the control law.

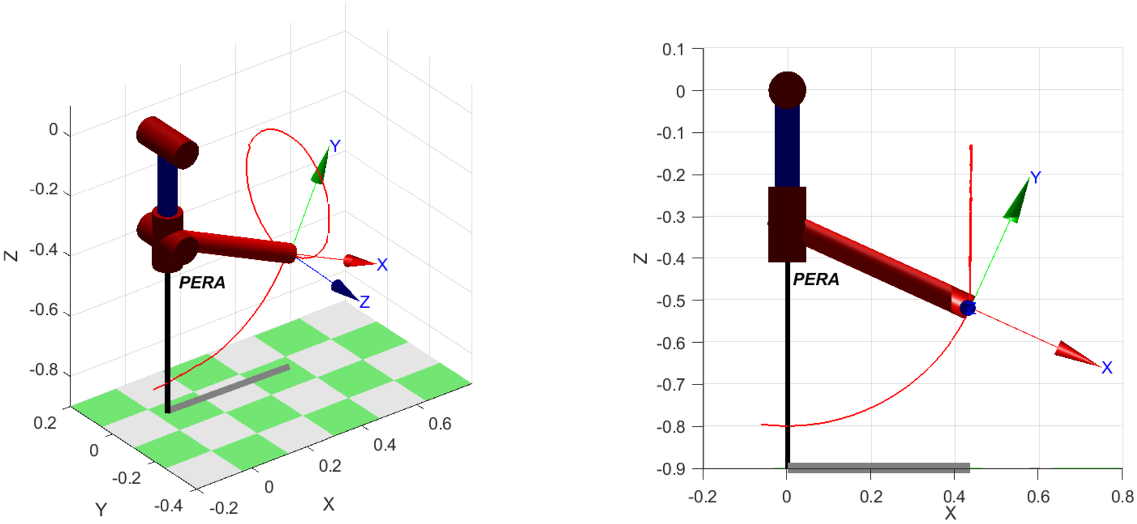

(a) 3D view (b) Side view

Figure 5.10: Visualization of the trajectory covered by the PERA in experiments

5.3.4 Comparison with non-saturated control

To compare the performance of the saturated controller with another controller, the non-saturated control law proposed in Theorem 4.2 was implemented into the system, resulting in the overall control law

$$u = \frac{\partial V}{\partial q}(q) + \Psi^{-\top}(q_d)\frac{d\Psi^{-1}(q_d)\dot{q}_d}{dt} - K_I z. \tag{5.15}$$

This input signal is translated to a signal in counts following (3.13), which is then saturated at the limits in (3.12). The system is initialized during the first five seconds, in the exact same way as in the experiments with the saturated controller; using the control law in (4.42) with the controller gains

$$\begin{aligned} \alpha &= \begin{bmatrix} 11.0 \\ 2.0 \\ 6.0 \end{bmatrix} & \beta &= \begin{bmatrix} 400 \\ 100 \\ 120 \end{bmatrix} \\ K_c &= \text{diag}\{30,\ 20,\ 200\} & R_c &= \text{diag}\{0.0001,\ 0.00001,\ 0.45\} \end{aligned} \tag{5.16}$$

for SPR. At time $t = 5$, the value of the new state x_c is set to $x_c = \mathbf{0}_3$ and the trajectory is initiated using control law (5.15) with the controller gains

$$K_I = \text{diag}\{400,\ 300,\ 600\} \quad K_c = \text{diag}\{30,\ 10,\ 60\} \quad R_c = \text{diag}\{0.0008,\ 0.00001,\ 0.5\}. \tag{5.17}$$

As in the saturated experiments, the tuning was selected to obtain the desired performance while removing the shaking from the motion of the elbow joint. The results are plotted in Figure 5.11. The results show that the performance is comparable with that of the saturated control law. The main difference that can be seen from comparing figures 5.6 and 5.11 is that the non-saturated control strategy results in larger errors in the position of the elbow joint (q_3). The position errors and input signals of the three joints are given in Figures 5.12 and 5.13.

From comparison of Figures 5.8 and 5.12 it can be observed that for q_1 and q_3, the performance of the saturated controller is better in terms of position errors. For q_2, however, the position error is larger when using the saturated controller. The logical explanation of these observations is that due to the shape of the hyperbolic tangent used in the saturated controller, the input in at a

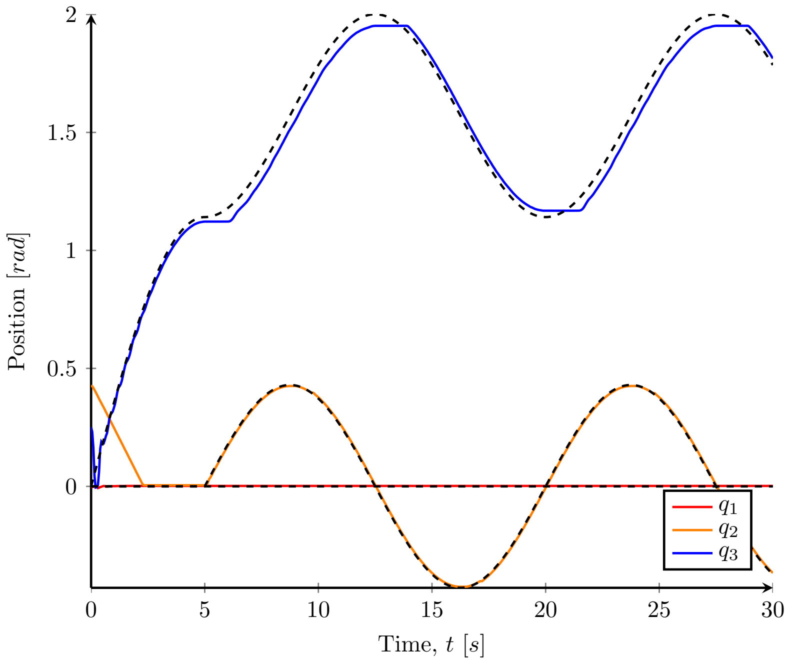

Figure 5.11: Experimental results (non-saturated). The colored lines represent the position of the joints during the experiment. The dashed lines represent the desired positions.

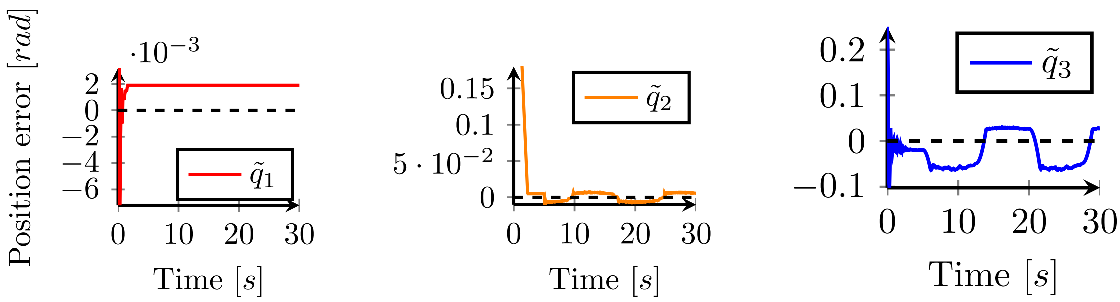

Figure 5.12: Position errors in the experiment (non-saturated)

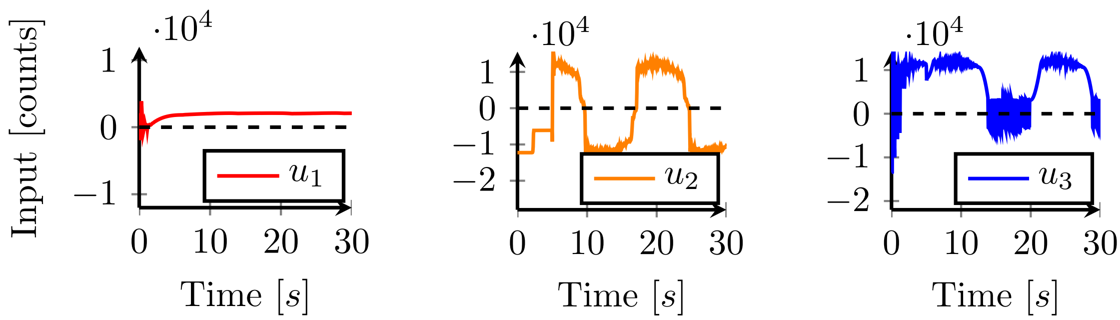

Figure 5.13: Input signals in the experiment (non-saturated)

high level for errors larger than some limit value. In the case of the second joint, the value of α is too small due to the saturation limit, resulting in relatively poor performance compared to the non-saturated control law. Furthermore, when the input signals to the joints are compared (Figures 5.9 and 5.13), they seem equal. The signal to the second joint is oscillating more for the non-saturated control law, while the oscillations in the third joint are larger when the saturated control law is used.

Again, the trajectory followed by the PERA is visualized in Figure 5.14. It can be observed from comparison of this figure to Figures 5.2 and 5.10 that the motion obtained with the non-saturated control law is less well positioned on the X-axis than the result with the saturated control law. This is caused by the larger error in the elbow pitch joint (q_3).

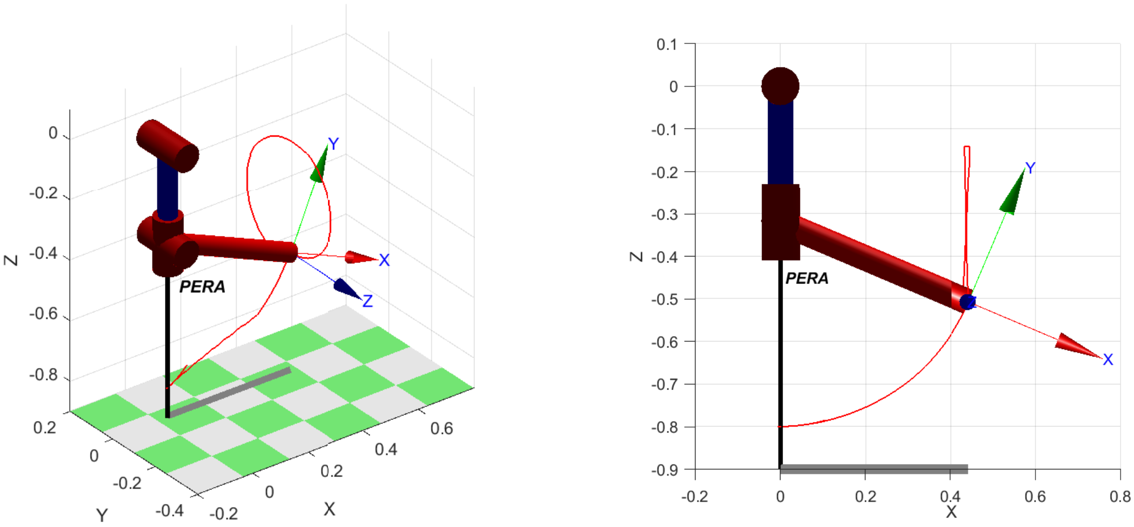

(a) 3D view (b) Side view

Figure 5.14: Visualization of the trajectory covered by the PERA in experiments (non-saturated)

In Table 5.1, the results of the saturated experiments and non-saturated experiments are further assessed on four properties. As could be expected, the saturated control law has a relatively low maximum input signal. Only for the shoulder pitch joint, the maximum input is higher with the saturated control law, which is caused by the large value of β. The total energy used by the motors is surprisingly equal for the first two joints. The third joint, however, uses more energy with the saturated control law. This is caused by the oscillations in the control signal. As a result, the maximum position errors of the first and third joint are both smaller when the saturated control law is used. The maximum position error of the second joint is smaller for the non-saturated controller. This is, as discussed above, caused by the low value of α in the saturated controller of the second joint. The average error positions are all proportional to the maximum error positions.

Property	**Parameter**	**Control type**	
		Saturated	**Non-saturated**
Maximum input signal [counts]	$\max\{u_1\}$	$2,128$	$2,094$
	$\max\{u_2\}$	$12,122$	$15,800$
	$\max\{u_3\}$	$15,646$	$16,000$
Total energy used $[N \cdot m]$	$\int \lvert u_1 \rvert$	24.04	23.48
	$\int \lvert u_2 \rvert$	16.60	16.83
	$\int \lvert u_3 \rvert$	75.23	56.30
Maximum position error $[rad]$	$\max\{\tilde{q}_1\}$	$3.00 \cdot 10^{-4}$	$1.90 \cdot 10^{-3}$
	$\max\{\tilde{q}_2\}$	$2.67 \cdot 10^{-2}$	$1.06 \cdot 10^{-2}$
	$\max\{\tilde{q}_3\}$	$3.29 \cdot 10^{-2}$	$6.39 \cdot 10^{-2}$
Average position error $[rad]$	$\text{mean}\{\tilde{q}_1\}$	$2.17 \cdot 10^{-4}$	$1.90 \cdot 10^{-3}$
	$\text{mean}\{\tilde{q}_2\}$	$1.50 \cdot 10^{-2}$	$5.40 \cdot 10^{-3}$
	$\text{mean}\{\tilde{q}_3\}$	$1.85 \cdot 10^{-2}$	$4.13 \cdot 10^{-2}$

Table 5.1: Comparison of the performance of the saturated controller with the performance of the non-saturated controller during the coverage by the end-effector of one circle trajectory, i.e. $5 < t \leq 20$.

Remark (Table 5.1)**.** To obtain the total energy used, the input signal in counts was translated to the resulting current over the motors using the polynomial approximations of the non-linear amplifiers of the motors (3.13). The absolute values of these data were numerically integrated by the trapezoidal rule (Atkinson, 2008),

$$\int_{20}^{5} |u_i| \; dt = \Delta t \left(\sum_{k=2}^{N-1} |u_{i,k}| + \frac{|u_{i,N}| + |u_{i,1}|}{2} \right), \tag{5.18}$$

with the sampling time $\Delta t = \frac{1}{200 \; [Hz]} = 0.005 \; [s]$, $u_{i.k}$ the input over the motor(s) of joint q_i in data point k and $N = 3001$ the number of data points. This value was multiplied by the nominal voltage over the motors, resulting in the total energy used in $[N \cdot m]$.

Note that the total energy used is the total energy used per motor. Hence, the total energy used by the shoulder and elbow pitch joints (q_1 and q_3) is twice as large.

5.3.5 Drawing a circle

For a final visualization of the trajectory followed by the system in the experiments, the end-effector of the PERA is equipped with a marker. To allow the gripper to hold the marker tight, a holder part is used (Figure 5.15). This part was originally developed for the thesis of Leeuwerik (2015), its intention being to allow the PERA to hold painting brushes. In the experiments, the holder was used to allow some motion of the marker to compensate for errors in the joint positions and sensor measurements. To ensure that the marker maintains contact with the canvas, a spring was added between the marker and the gripper.

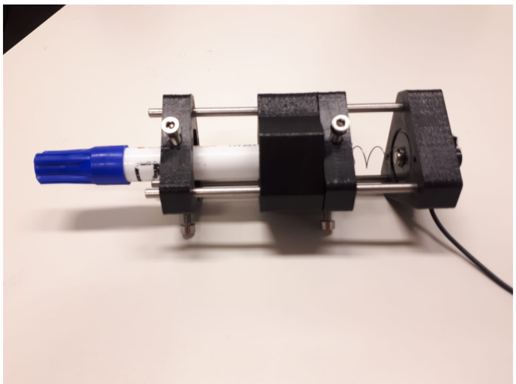

(a) Image of the holder with marker

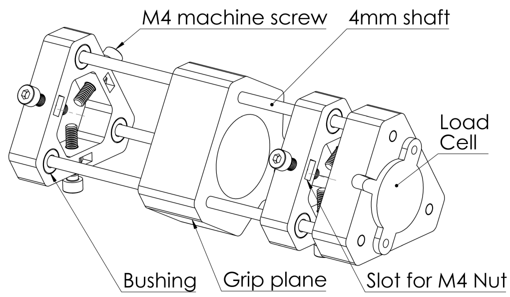

(b) CAD drawing of the holder - by Leeuwerik (2015)

Figure 5.15: Marker holder for the PERA

After mounting the marker and holder to the gripper of the PERA, a canvas (whiteboard) is placed such that a circle is drawn on the canvas when the PERA is following the desired trajectory. The result is shown in Figure 5.16a. To show the path of the marker on the canvas more clearly, the photo was edited, resulting in Figure 5.16b. The resulting drawing (Figure 5.16) closely mimics the shape of a circle. Still, it is not a perfect circle, which is due to joint position errors, motion of the marker and the sensor offsets discussed in Chapter 3. The position errors are partially caused by the normal force exerted on the end-effector by the canvas. Due to the unpredictable position sensor offsets, it was difficult to position the canvas correctly; in most experiments, only half of the circle was drawn, or the motion of the PERA was completely halted by the normal force exerted by the canvas. Furthermore, it can be seen in the result that the pressure of the marker on the canvas is not constant over time.

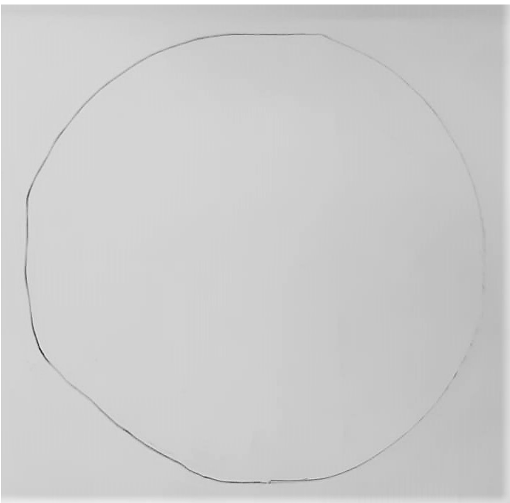

(a) Photo

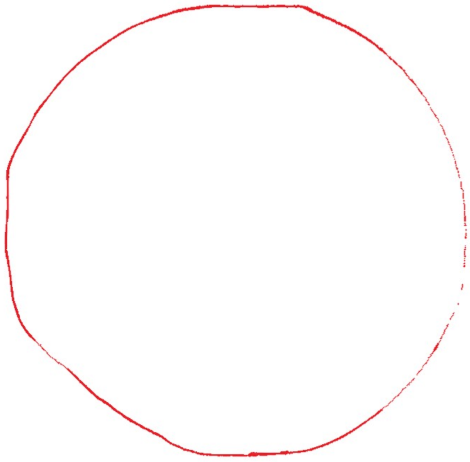

(b) Edited

Figure 5.16: Circle drawn by the PERA

5.3.6 Other trajectories

To further demonstrate the performance of the control law proposed in Theorem 4.3, it was decided to design two more trajectories for the end effector, such that the PERA would draw the shapes of a lemniscate and a heart. These trajectories are considered more complex than the circle trajectory. Due to the complexity of the calculations of the inverse kinematics of the PERA, the desired trajectories are polynomial approximations of the desired positions of the joints. To ensure a good fit (in the sense of least-squares), only one period of motion is tracked, i.e. the shape is tracked once per experiment. Because the closed-loop system was found to theoretically converge to any desired trajectory, the results of simulations for the other trajectories are not provided.

Lemniscate

For the application of drawing of a lemniscate (infinity symbol) with a period of 15 seconds, the desired Cartesian coordinates of the end effector are defined as (Weisstein, n.d.[b])

$$
\begin{aligned}
x &= 0.44 \\
y &= \frac{0.16\sqrt{2}\cos\left(\frac{2\pi}{T}t\right)}{\sin^2\left(\frac{2\pi}{T}t\right)+1} \\
&= \frac{0.23\cos\left(0.42t\right)}{\sin^2\left(0.42t\right)+1} \\
z &= -L_1 + \frac{0.2\sqrt{2}\sin\left(\frac{2\pi}{T}t\right)\cos\left(\frac{2\pi}{T}t\right)}{\sin^2\left(\frac{2\pi}{T}t\right)+1} \\
&= -0.36 + \frac{0.28\sin\left(0.42t\right)\cos\left(0.42t\right)}{\sin^2\left(0.42t\right)+1},
\end{aligned}
\tag{5.19}
$$

such that the PERA follows a lemniscate-shaped path in the plane $x = 0.44$. The y- and z-coordinates are depicted in Figure 5.17.

The trajectory of the end-effector in Cartesian space was translated to the desired trajectory of the PERA in joint space by using the inverse kinematics function (`ikine()`) from the Robotic Toolbox by Corke et al. (1996) in MATLAB®. This function returned a set of 3001 data points with the desired joint angles at discrete times between zero and fifteen seconds after the initiation of the trajectory (one period). However, since the goal of this thesis is trajectory tracking and not SPR, the desired trajectory of the joints should be a differentiable function. Therefore, 20th order

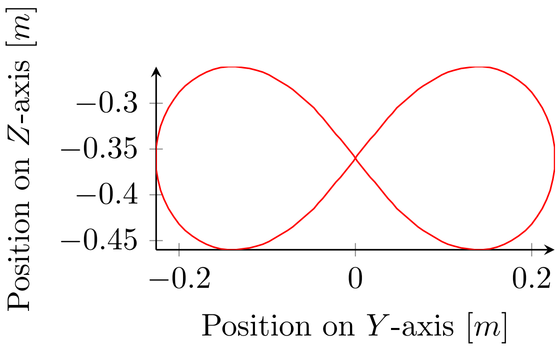

Figure 5.17: Cartesian y- and z-coordinates of the desired lemniscate trajectory of the end-effector of the PERA in the plane $x = 0.44$

polynomial approximations of the desired joint trajectories were constructed, using the `polyfit()` function in MATLAB®. The functions of the desired trajectory, along with the MATLAB® script used to compute these functions, can be found in Appendix F. The approximations found were used to compute the desired steady-state input (u_d).

As was done previously for the circle trajectory, the desired trajectory of the PERA is visualized in Figure 5.18.

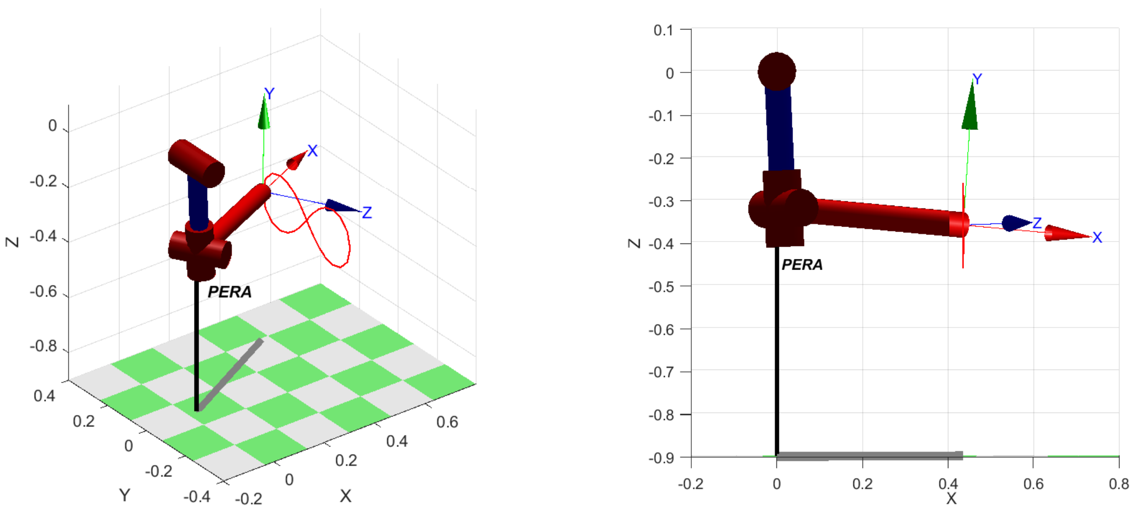

(a) 3D view (b) Side view

Figure 5.18: Visualization of the desired trajectory of the PERA (lemniscate)

Similar to the circle trajectory experiments, the PERA is initialized using SPR in the first five seconds of the experiment, with

$$q_d = \begin{bmatrix} 0.05 \\ 0.50 \\ 1.45\sin(0.31t) \end{bmatrix}, \tag{5.20}$$

such that at time $t = 5$, the PERA is initialized at

$$q_0 \approx \begin{bmatrix} 0.05 \\ 0.50 \\ 1.45 \end{bmatrix}. \tag{5.21}$$

Note that the second term in (5.20) is not a time function, as opposed to the third term. This is due to the larger strength of the motors in the third joint, which would cause oscillations in the response. For the second joint, the motor can exert its maximum force without causing any oscillations, due to its relatively low strength. At time $t = 5$, the virtual state is set to $x_c = \mathbf{0}_3$, such that the system is initialized in the desired starting position.

Next, the desired lemniscate trajectory is started, with the saturated control law proposed in (4.42) and the controller gains as in (5.14). The result is shown in Figure 5.19.

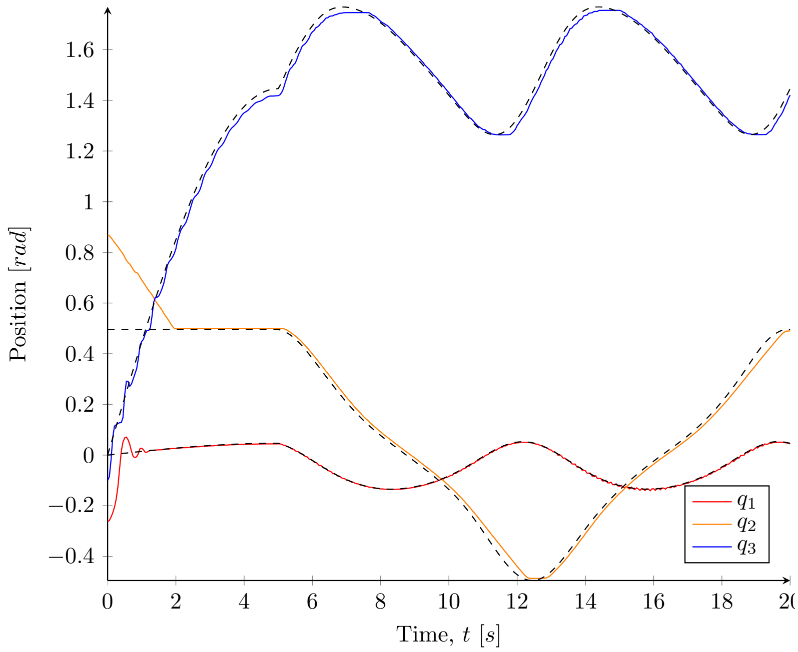

Figure 5.19: Experimental results (lemniscate). The colored lines represent the position of the joints during the experiment. The dashed lines represent the desired positions.

This trajectory is visualized in Figure 5.20. From comparison with Figure 5.18, it becomes clear that the trajectory travelled by the end-effector is not perfect, but approaches the desired path quite successfully. Furthermore, the lemniscate is slightly tilted around the Y-axis compared with the desired trajectory. When attempting to draw the lemniscate on a canvas, this poses an issue.

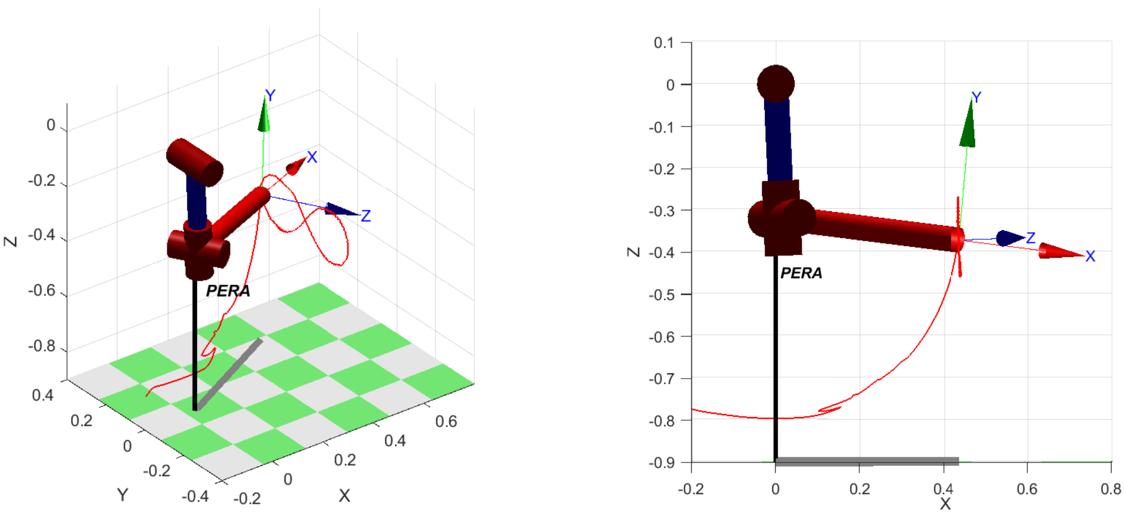

(a) 3D view (b) Side view

Figure 5.20: Visualization of the trajectory covered by the PERA in experiments (lemniscate)

Heart

For the application of drawing of a heart, the desired Cartesian coordinates of the end effector are defined as (Weisstein, n.d.[a])

$$
\begin{aligned}
x &= 0.44 \\
y &= \frac{1}{80} 16 \sin^3\left(\frac{2\pi}{T}t\right) \\
&= 0.2 \sin^3(0.42t) \\
z &= \frac{1}{80}\left(13\cos\left(\frac{2\pi}{T}t\right) - 5\cos\left(\frac{4\pi}{T}t\right) - 2\cos\left(\frac{6\pi}{T}t\right) - \cos\left(\frac{8\pi}{T}t\right)\right) - 0.4 \\
&= 0.16\cos(0.42t) - 0.06\cos(0.84t) - 0.03\cos(1.26t) - 0.01\cos(1.68t) - 0.4,
\end{aligned}
\tag{5.22}
$$

such that the PERA follows a heart-shaped path in the plane $x = 0.44$. The y- and z-coordinates are depicted in Figure 5.21.

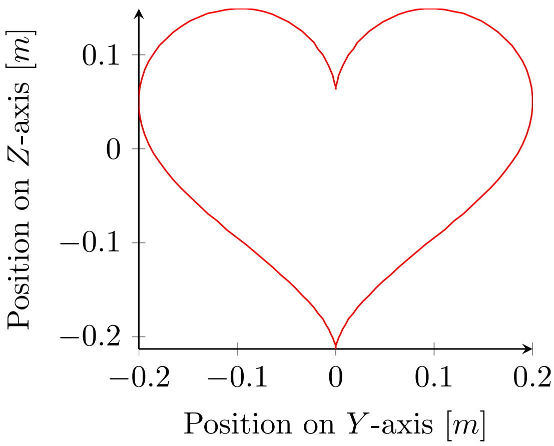

Figure 5.21: Cartesian y- and z-coordinates of the desired heart trajectory of the end-effector of the PERA in the plane $x = 0.44$

Using the same method as discussed for the lemniscate, 20th order polynomial approximations of the desired trajectory were constructed. These approximation, as well as the MATLAB® script used to find them, can be found in Appendix F. In this script, the desired input (u_d) is constructed from the polynomials.

Again, the desired trajectory of the PERA is visualized in Figure 5.22.

Similar to the other experiments, the PERA was initialized with SPR in the first five seconds of the experiment, with

$$
q_d = \begin{bmatrix} 0.19 \\ 0 \\ 0.71\sin(0.31t) \end{bmatrix}, \tag{5.23}
$$

such that at time $t = 5$, the PERA is initialized at

$$
q_0 \approx \begin{bmatrix} 0.19 \\ 0 \\ 0.71 \end{bmatrix}. \tag{5.24}
$$

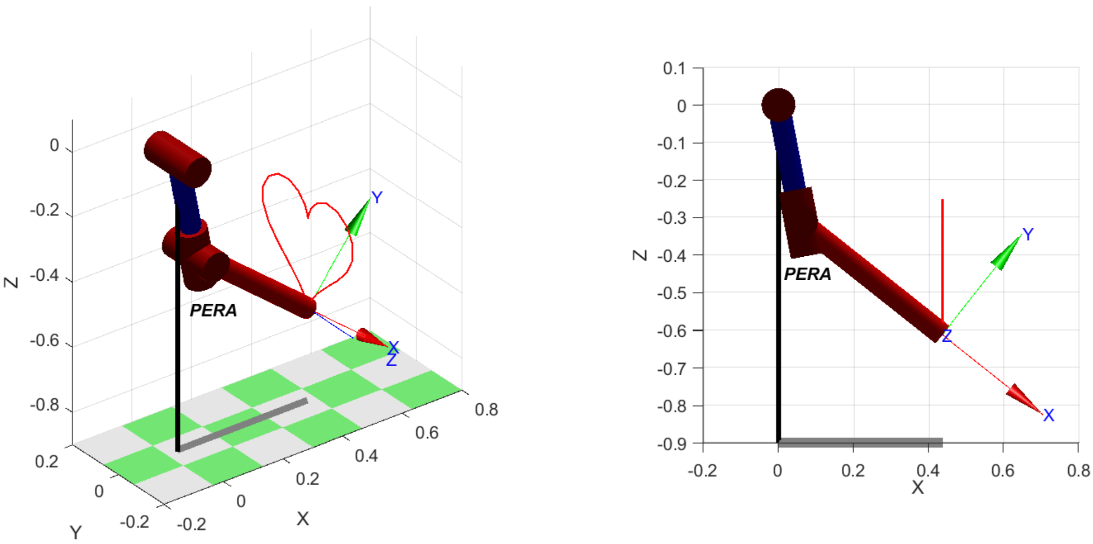

(a) 3D view (b) Side view

Figure 5.22: Visualization of the desired trajectory of the PERA (heart)

At time $t = 5$, the virtual state is set to $x_c = \mathbf{0}_3$, such that the system is initialized in the desired starting position.

Then, the desired heart trajectory is started, using the saturated control law proposed in (4.42) and the controller gains as in (5.14). The result is shown in Figure 5.23. This trajectory is visualized

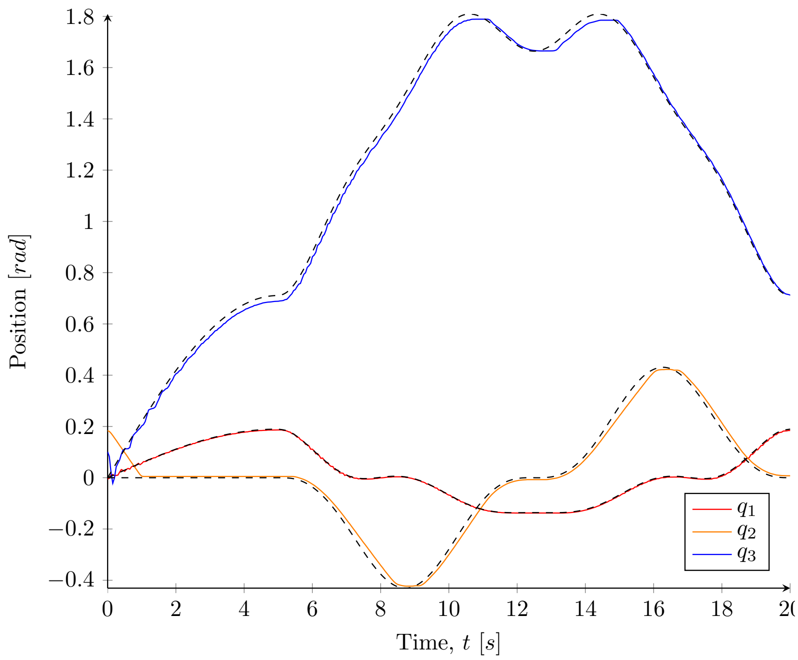

Figure 5.23: Experimental results (heart). The colored lines represent the position of the joints during the experiment. The dashed lines represent the desired positions.

in Figure 5.24. From comparison with Figure 5.22, it becomes clear that the trajectory travelled by the end-effector shows some visible differences with the desired trajectory. Furthermore, there is some variance of the x-coordinate of the end-effector, which should be invariant. These issues are problematic for drawing the heart in the current setup.

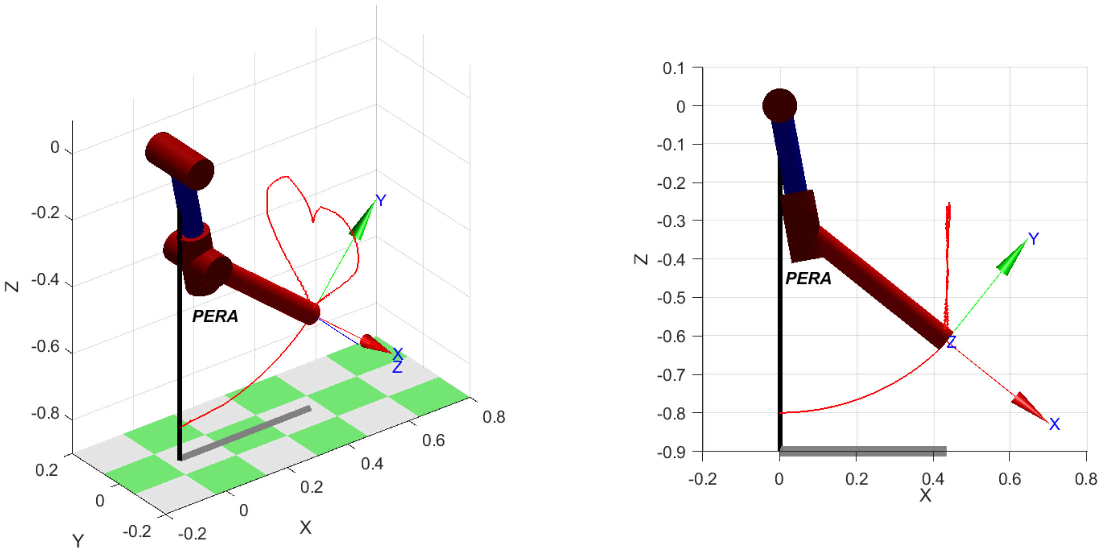

(a) 3D view

(b) Side view

Figure 5.24: Visualization of the trajectory covered by the PERA in experiments (heart)

5.3.7 Drawing enhancement

To enhance the drawings produced by the PERA, the position sensor offsets, position errors and slightly wrong placement of the canvas have to be dealt with. Furthermore, in the case of the lemniscate and heart, errors of the polynomial approximations are present. Therefore, a heuristic approach to update the desired position of the shoulder pitch joint (q_1) is proposed. This strategy aims to regulate the position of the joint, such that the force exerted by the canvas on the end-effector of the PERA remains below the desired maximum. When the forces measured in the wrist joints of the PERA are above a specified level, the desired position of the shoulder pitch joint ($q_{d,1}$) is decreased, such that the x-coordinate of the end-effector in the Cartesian space decreases and the PERA can continue its motion without being halted by the canvas. When the forces in the wrist decrease to below another specified level, the value of $q_{d,1}$ is gradually brought back to its original value, such that the end-effector maintains contact with the canvas.

To determine the 'normal' force measured by the force sensors during the motion of the PERA, i.e. without disturbances of the canvas, the averages of the signal of the two force sensors in the wrist during the first circle motion ($5 \leq t \leq 20$) are determined by

$$\begin{aligned}\mu_{W1} &= \sum_{k=1001}^{4001} \frac{F_{W1}(k)}{N} \\ \mu_{W2} &= \sum_{k=1001}^{4001} \frac{F_{W2}(k)}{N},\end{aligned} \tag{5.25}$$

with μ the mean signal form the force sensor during initialization, F the signal from the force sensor, k the sample-number, such that for $k = 1,\ t(k) \approx 0\ [s]$, for $k = 1001,\ t(k) \approx 5\ [s]$ and for $k = 4001,\ t(k) \approx 20\ [s]$, $N = 3001$ the number of samples used to determine the mean and the subscripts $W1$ and $W2$ denoting the first and second force sensor in the wrist, respectively.

Using the means, the total force deviation e is given by

$$e(k) = |F_{W1}(k) - \mu_{W1}| + |F_{W2}(k) - \mu_{W2}|\,. \tag{5.26}$$

To filter the noise coming from the sensor measurements, a simple moving average (SMA) is applied to the total force deviation, such that

$$e_{\mathrm{SMA}}(k) = \frac{1}{M} \sum_{i=k-M+1}^{k} e(i), \tag{5.27}$$

with $M = 200$ the number of samples used for the SMA.

The following sequence is used to update the desired position of the shoulder pitch joint, starting after the first circle motion, i.e. at $t = 20$.

$$q_{d,1,\mathrm{new}}(k) = q_{d,1}(t(k)) - c(k), \tag{5.28}$$

where the compensation angle c in radians is updated according to

$$c(k) = \begin{cases} c(k-1) + 0.002, & \text{if } e_{\mathrm{SMA}}(k) > l_1 \\ c(k-1) - 0.002, & \text{if } e_{\mathrm{SMA}}(k) < l_2 \text{ and } c(k-1) > 0, \end{cases} \tag{5.29}$$

with l_1 and l_2 denoting the upper and lower bounds on the SMA of the total force deviation. These bounds ensure that the magnitude of the compensation angle remains constant when the SMA is within the bounds. If the SMA is greater than the upper limit, the compensation angle increases and when the SMA is smaller than the lower limit, the value of the compensation angle decreases back to zero.

Use of this heuristic approach allows the dealing with sensor offsets and errors in the positions of the joint and placement of the canvas. This ensures that the marker remains in contact with the canvas, as long as the canvas is close to the correct position. The downside of this approach is that the value of $q_{d,1}$ is changed with respect to the desired trajectory. As a result, the object drawn by the PERA does not have the exact shape that is intended. Furthermore, when the pressure of the marker on the canvas is such that the total force deviation is oscillating around the limit on the total force deviation, this causes oscillations in the desired position of the shoulder pitch joint. In time, this issue was largely solved by tuning of the upper and lower bounds.

In a new experiment, a circle is drawn by the PERA using the proposed heuristic approach with

$$\begin{aligned} l_1(k) =& 4.7t(k) - 906 \\ l_2(k) =& 4.7t(k) - 606. \end{aligned} \tag{5.30}$$

These bounds are determined by comparison of the values of e_{SMA} during experiments without external disturbances and during experiments where the canvas acted as an external disturbance.

An average experiment would result in drawings such as the one depicted in Figure 5.25. The corresponding SMA of the total force deviation (e_{SMA}) and compensation angle c are plotted in Figure 5.26. However, the drawing quality could be greatly improved by altering the orientation of the canvas; the best result is shown in Figure 5.27a. To show the path of the marker on the canvas more clearly, the photo was edited, resulting in Figure 5.27b. Comparison of Figure 5.27 to Figure 5.16 shows that the pressure of the marker on the canvas is larger and more constant, and therefore the quality of the drawing is better. It can be concluded that the error in the drawing arising from the positioning errors of sensors, joints and canvas is worse than the errors arising from the change in trajectory due to the heuristic approach.

Furthermore, an attempt is made to draw the shapes of the heart and lemniscate, by using the proposed heuristic approach. For the lemniscate, the limits are set to

$$\begin{aligned} l_1(k) =& 800 \\ l_2(k) =& 500. \end{aligned} \tag{5.31}$$

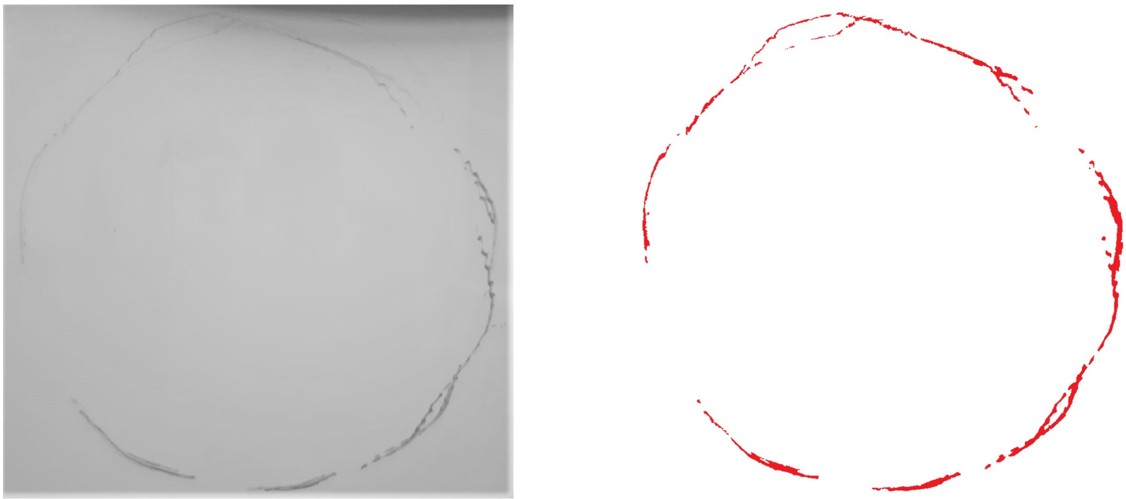

(a) Photo (b) Edited

Figure 5.25: Average result with the heuristic approach for drawing enhancement

The best result obtained is shown in Figure 5.28. The shaking of the elbow joint results in the irregularities which are visible in the drawing. Although the shape of the lemniscate is not perfect, the result is close to the desired trajectory.

For the heart, the limits are set to

$$\begin{aligned} l_1(k) =& 3.3t(k) + 750 \\ l_2(k) =& 3.3t(k) + 450. \end{aligned} \tag{5.32}$$

The best result is shown in Figure 5.29. It is clearly visible that the shape is not exactly as desired. On the other hand the shape of a heart is clearly recognizable, and contact with the canvas is maintained throughout the trajectory.

From the experiments, it is concluded that the heuristic approach for drawing enhancement allows the dealing with errors and offsets, enabling the PERA to draw the desired shapes. It should be mentioned, however, that the proposed heuristic approach is far from optimal. While it improves the drawing results of the circle, the result was still very dependent on the placement of the canvas with respect to the PERA. For the application of drawing with robotic arms, it may be interesting to further develop this heuristic approach in the future, by involving other joints and force sensors in the heuristic approach and adapting the limits and update sequence of the compensation angle. Another option to maintain a constant pressure on the canvas may be to use the Jacobian matrix obtained in this work to design a force control strategy as described in Spong and Vidyasagar (2008), Craig (2009), and Siciliano and Khatib (2016) and many other works.

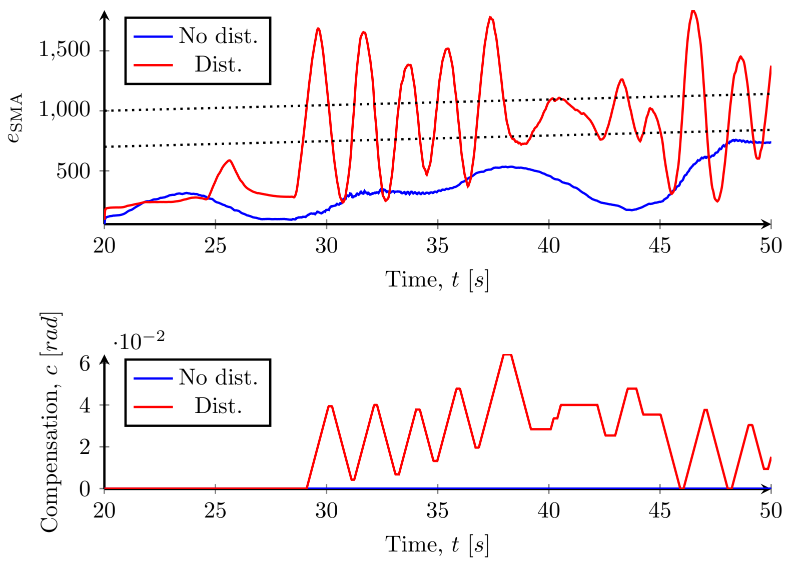

Figure 5.26: Values of e_{SMA} and the resulting compensation angle of the shoulder pitch joint. The blue lines represent the results when there is no disturbance. The red lines represent the case of the experiment resulting in Figure 5.25

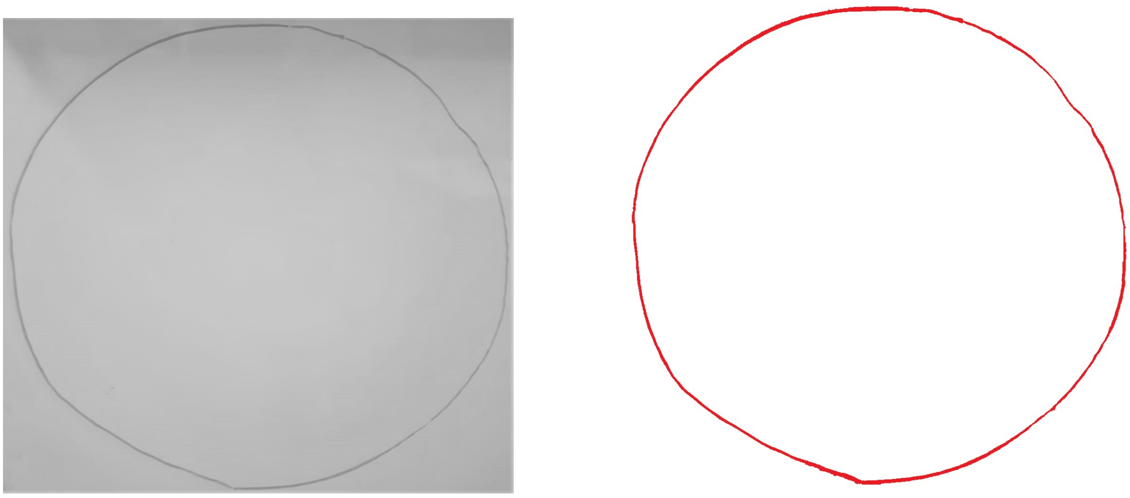

(a) Photo (b) Edited

Figure 5.27: Circle drawn by the PERA, using the heuristic approach for drawing enhancement

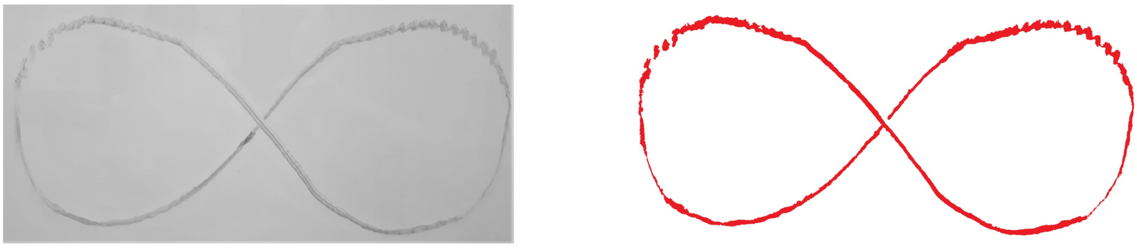

(a) Photo (b) Edited

Figure 5.28: Lemniscate drawn by the PERA, using the heuristic approach for drawing enhancement

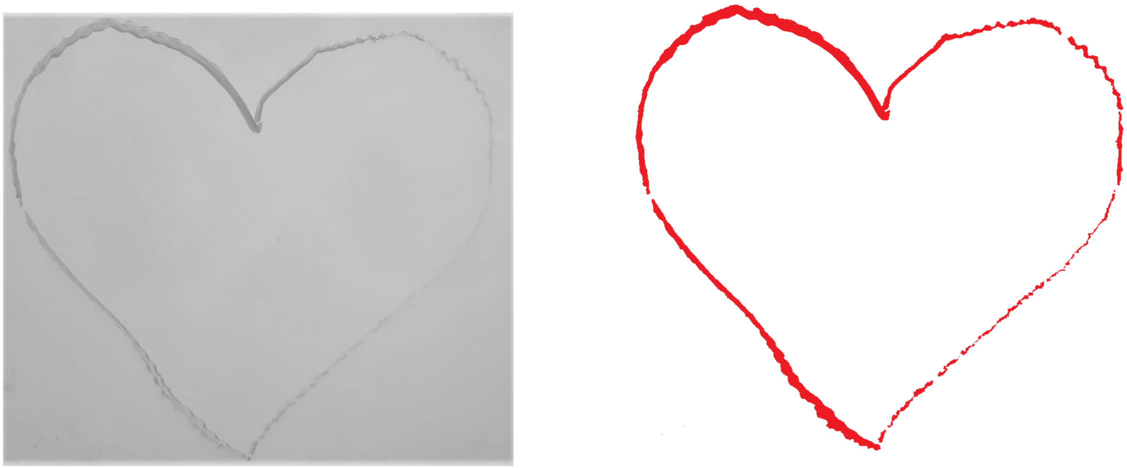

(a) Photo (b) Edited

Figure 5.29: Heart drawn by the PERA, using the heuristic approach for drawing enhancement

5.3.8 End-effector orientation

In another approach to improving the drawings produced by the PERA, control of the orientation of the end-effector is investigated. Including the wrist of the PERA allows the orientation of the marker to remain perpendicular to the canvas. This is assumed to improve the drawing quality. To allow implementation of the wrist joints into the system, all steps previously done for the shoulder pitch, shoulder yaw and elbow pitch need to be repeated for the wrist joints.

System modeling (5 DoF)

As a first step towards implementation of the wrist joint in the experiments, a new model is constructed. The following schematic representation of the PERA follows from the inclusion of the wrist.

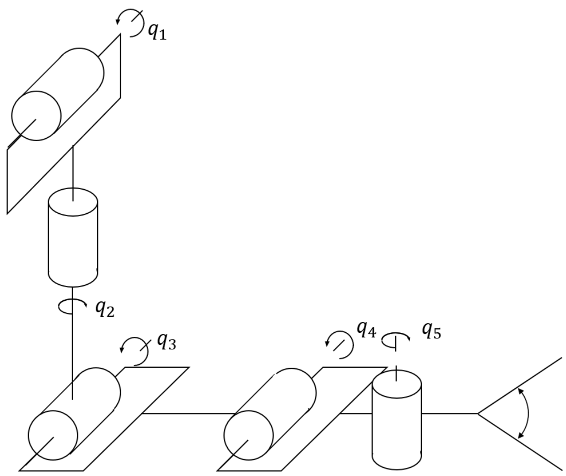

Figure 5.30: Schematic representation of the PERA (5DoF)

The corresponding DH parameters are in Table 5.2. Using the Robotic Toolbox, a new graphical model is obtained, as shown in Figure 5.31.

i	α_{i-1}	a_{i-1}	d_i	θ_i
1	$\frac{\pi}{2}$	0	0	q_1
2	$-\frac{\pi}{2}$	0	-0.32	q_2
3	$\frac{\pi}{2}$	0	0	$q_3 - \frac{\pi}{2}$
4	0	0.28	0	q_4
5	$-\frac{\pi}{2}$	0	0	q_5
6	0	0.20	0	0

Table 5.2: Denavit-Hartenberg link parameters (5 DoF)

Using the same procedure as used for the model with three DoF, the inertia matrix and potential energy vector are obtained (see Appendix G). The magnitude of the potential energy is such that

$$\left|\frac{\partial V}{\partial q}(q)\right| \leq \begin{bmatrix} 7.74 \\ 1.57 \\ 1.57 \\ 0.13 \\ 0.13 \end{bmatrix}. \tag{5.33}$$

From the inertia matrix, the Cholesky factorization of its inverse ($\Psi(q)$) is obtained. Furthermore, the gyroscopic forces matrix for the five DoF model, which is non-zero in this case, is computed

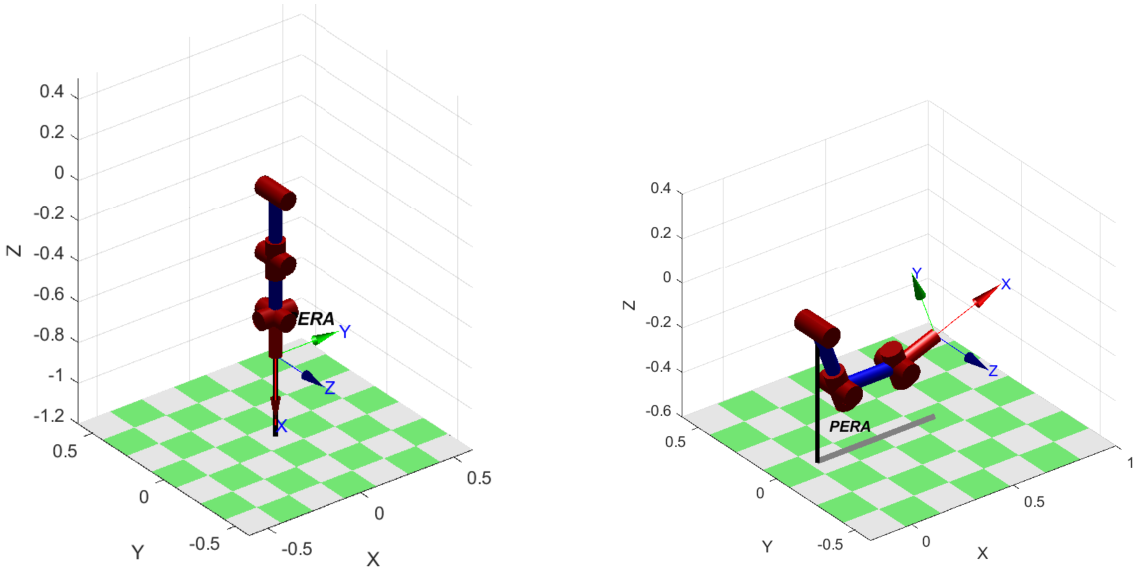

(a) $q_1 = 0°$, $q_2 = 0°$, $q_3 = 0°$, $q_4 = 0°$, $q_5 = 0°$ (b) $q_1 = 20°$, $q_2 = 0°$, $q_3 = 70°$, $q_4 = 20°$, $q_5 = 0°$

Figure 5.31: Graphical model of the PERA (5 DoF)

following the procedure of Venkatraman et al. (2010). Moreover, the equation for the desired steady-state input is now defined as

$$u_d = \frac{\partial V}{\partial q}(q_d) + \underbrace{\Psi^{-\top}(q_d)\frac{d\Psi^{-1}(q_d)\dot{q}_d}{dt} - \Psi^{-\top}(q_d)J(q_d,p_d)\Psi^{-1}(q_d)\dot{q}_d}_{\gamma}. \tag{5.34}$$

Due to the high complexity of the γ-term in this equation, it could not be computed in real-time during simulations or experiments. Therefore, the value of this input for each time step was computed beforehand and then taken from an external file during simulations.

Due to the changed desired steady-state input, the control law for the torque on each joint is now given by

$$u = \frac{\partial V}{\partial q}(q) + \gamma - \sum_{i=1}^{3} e_i \alpha_i \tanh(\beta_i z_i). \tag{5.35}$$

Experimental setup of the wrist

Next, the experimental setup of the wrist is investigated. The behaviour of the non-linear amplifiers in the wrist is plotted in Figure 5.32. Because this relationship is virtually linear, it is approximated by

$$u_{\text{counts},W_1,W_2} = 70.5 u_{\text{current},W_1,W_2}. \tag{5.36}$$

Furthermore, the relation between current over the wrist motors and torque on the joints is given by

$$u_{\text{current},W_1} = \frac{1000 \cdot 1000 \cdot (u_{\text{torque},q_4} + u_{\text{torque},q_5})}{G_r \cdot \eta \cdot k_m \cdot k_d} \tag{5.37}$$

$$u_{\text{current},W_2} = \frac{1000 \cdot 1000 \cdot (u_{\text{torque},q_4} - u_{\text{torque},q_5})}{G_r \cdot \eta \cdot k_m \cdot k_d}, \tag{5.38}$$

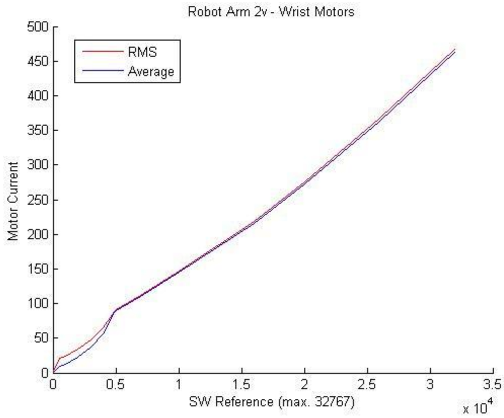

Figure 5.32: Behaviour of non-linear amplifiers in the wrist - by Rijs et al. (2014)

with $G_r = 290$ (Rijs et al., 2014), $\eta = 0.70$ (Appendix B), $k_m = 21.2$ $[\frac{mN \cdot m}{A}]$ (Appendix B) and $k_d = 2$.

This leads to the saturation limits on the torque inputs on the wrist joints as

$$\begin{aligned} -1.95 \leq u_{q_4} + u_{q_5} \leq 1.95 \\ -1.95 \leq u_{q_4} - u_{q_5} \leq 1.95. \end{aligned} \tag{5.39}$$

Desired trajectory (5 DoF)

For the end-effector to follow the path of a circle, the desired trajectory in joint space is given by

$$q_d = \begin{bmatrix} q_{d1} \\ q_{d2} \\ q_{d3} \\ q_{d4} \\ q_{d5} \end{bmatrix} = \begin{bmatrix} 0 \\ \arcsin\left(\frac{r}{L_2}\right)\sin\left(\frac{2\pi}{T}t\right) \\ \frac{\pi}{2} - \arcsin\left(\frac{r}{L_2}\right)\cos\left(\frac{2\pi}{T}t\right) \\ \arcsin\left(\frac{r}{L_2}\right)\cos\left(\frac{2\pi}{T}t\right) \\ -\arcsin\left(\frac{r}{L_2}\right)\sin\left(\frac{2\pi}{T}t\right) \end{bmatrix} \tag{5.40}$$

with $L_2 \in \mathbb{R}_+$ the new length of the second link (lower arm), $r \in \mathbb{R}_+$ the radius of the circle, $T \in \mathbb{R}_+$ the period of the circle trajectory and $t \in \mathbb{R}_+$ the time. Due to limitations in the RoM of the wrist yaw, it is not feasible to take the desired radius as $r = 0.2$ $[m]$ again. Therefore, the radius is set to $r = 0.14$ $[m]$. Substituting $L_2 = 0.28$ $[m]$ and setting $T = 15$ $[s]$ yields

$$q_d = \begin{bmatrix} 0 \\ 0.52\sin(0.42t) \\ 1.57 - 0.52\cos(0.42t) \\ 0.52\cos(0.42t) \\ -0.52\sin(0.42t) \end{bmatrix}. \tag{5.41}$$

Compared to the original desired trajectory in (5.2), the amplitude of the second and third joint has become larger. Furthermore, the wrist joints have been added to assure that the orientation of the marker is perpendicular to that of the canvas. The Cartesian x-coordinate of the plane on which to draw is given by $x = \sqrt{L_2^2 - r^2} + L_3$, were $L_3 = 0.2$ $[m]$ is the length of the hand, such that $x \approx 0.44$. The desired trajectory is visualized in Figure 5.33

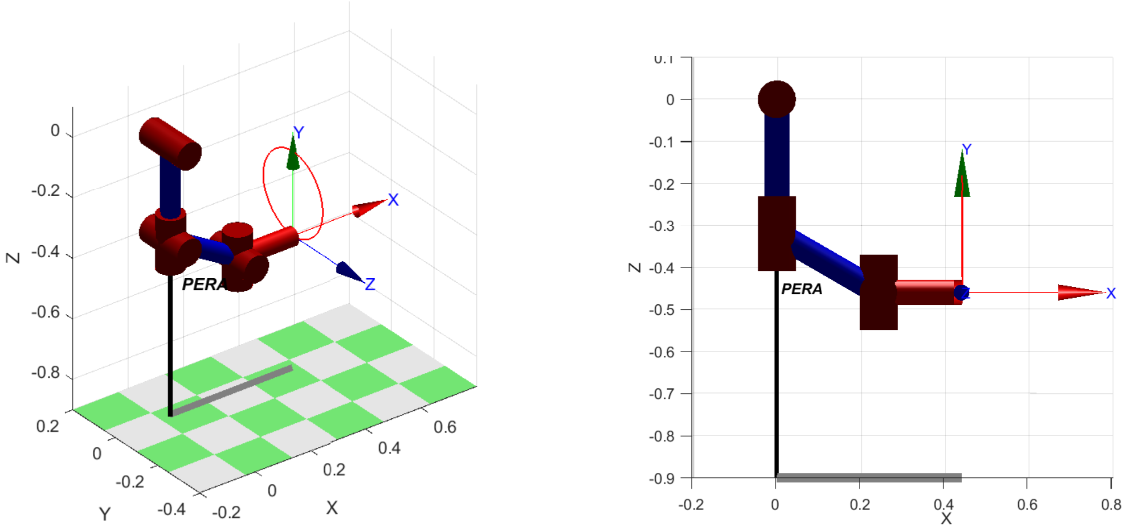

(a) 3D view

(b) Side view

Figure 5.33: Visualization of the desired trajectory of the PERA (5 DoF)

From the desired trajectory (5.41), it follows that the second term of the control law (5.35)

$$|\gamma| \leq \begin{bmatrix} 0.0032 \\ 0.044 \\ 0.0052 \\ 0.0030 \\ 6.89 \cdot 10^{-5} \end{bmatrix}. \tag{5.42}$$

Assuming that for the desired wrist gains $\alpha_4 = \alpha_5$, and following from (5.33), the saturation limits in (3.14) and (5.39) are always satisfied if

$$\alpha = \begin{bmatrix} \alpha_1 \\ \alpha_2 \\ \alpha_3 \\ \alpha_4 \\ \alpha_5 \end{bmatrix} \leq \begin{bmatrix} 11.03 \\ 1.71 \\ 6.14 \\ 0.85 \\ 0.85 \end{bmatrix}. \tag{5.43}$$

Simulations (5 DoF)

Using the new modeling of the PERA, simulations are performed. The values of α are selected as

$$\alpha = \begin{bmatrix} 11.0 \\ 2.0 \\ 6.0 \\ 0.85 \\ 0.85 \end{bmatrix} \tag{5.44}$$

in both the simulations and experiments. In the simulations, the other controller gains are selected as

$$\beta = \begin{bmatrix} 40 \\ 40 \\ 30 \\ 30 \\ 30 \end{bmatrix} \quad K_c = \text{diag}\{30,\ 10,\ 5.3,\ 1.8,\ 1.8\} \quad R_c = \text{diag}\{0.2,\ 0.23,\ 1.22,\ 1.5,\ 1.5\} \tag{5.45}$$

The simulations are performed using this tuning for the controller and the initial position of the PERA set as the downward position, i.e. $q_0 = \mathbf{0}_5$. Moreover, the initial time is set to zero, i.e. $t_0 = 0$. The results of the simulation are plotted in Figure 5.34.

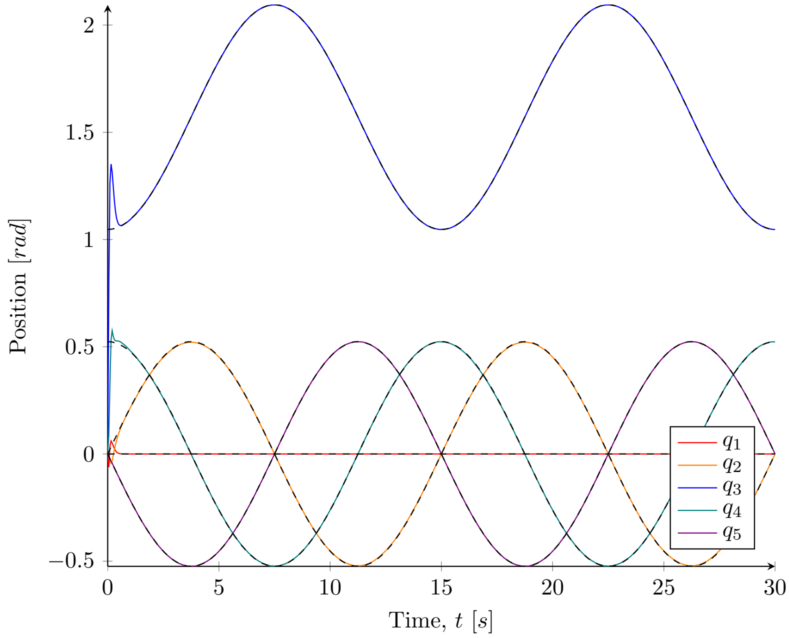

Figure 5.34: Simulation results (5 DoF). The colored lines represent the position of the joints during the simulation. The dashed lines represent the desired positions.

The figure shows that the convergence to the trajectory is successful and fast. To allow a better observation of the start of the simulation, Figure 5.34 is zoomed into to obtain Figure 5.35. It becomes clear that, although there is some undesired movement of the joints as a result of the trajectory initiation, the simulations smoothly converge to the desired trajectory. Considerable overshoots, like that of the elbow pitch joint (q_3), are especially undesirable. Therefore, the system is initialized at a position close to the starting point of the trajectory during the experiments.

The results were visualized to observe the trajectory followed by the end-effector of the PERA in the simulations. As can be seen in the resulting figure (Figure 5.36), the overshoot of the elbow pitch joint results in a serious error on the trajectory, but after the first second, the system indeed converges to the desired trajectory (Figure 5.33).

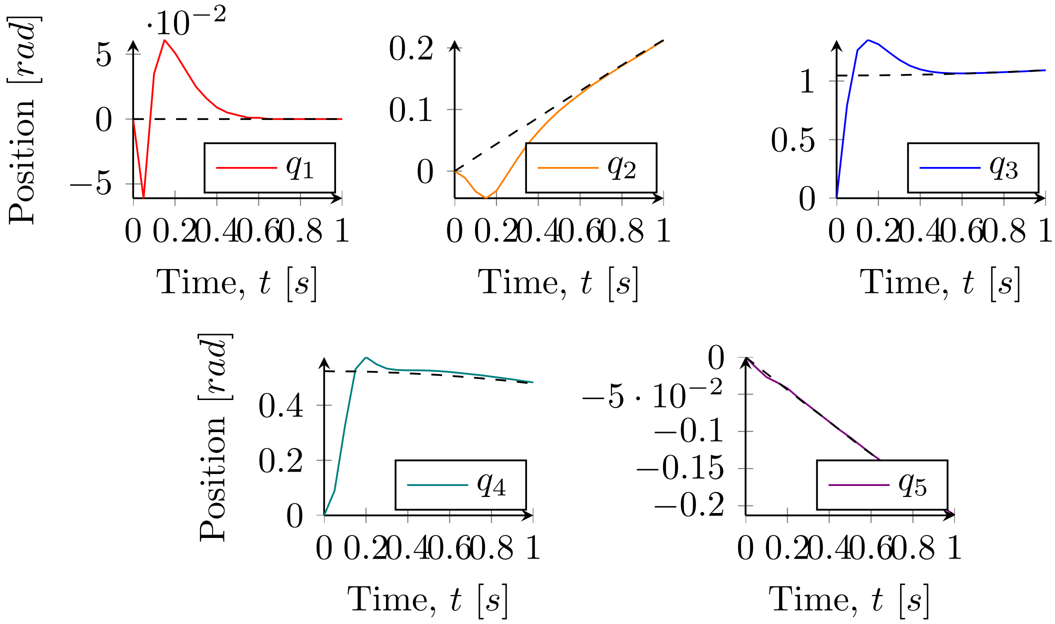

Figure 5.35: First second of the simulation results (5 DoF)

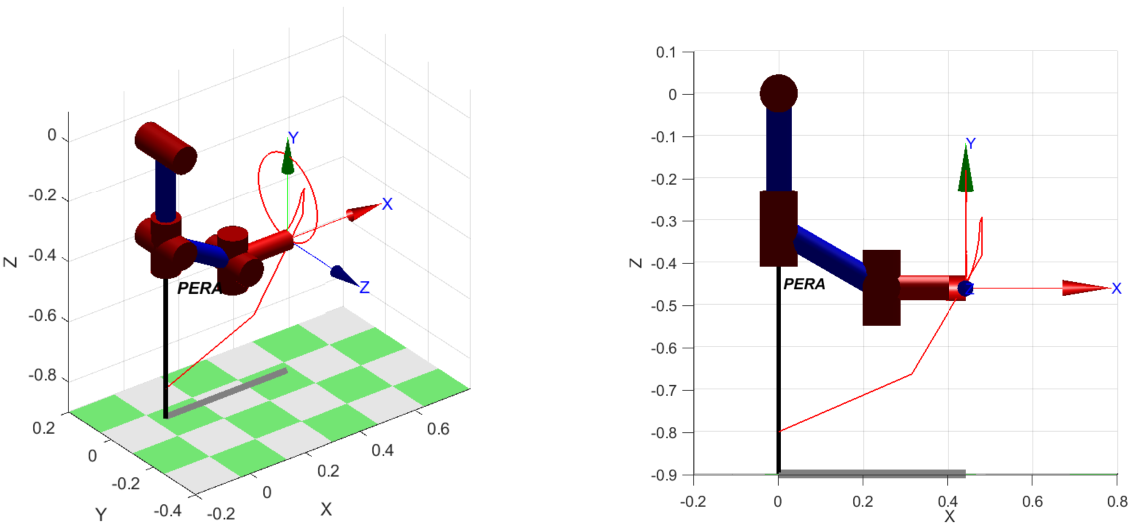

(a) 3D view

(b) Side view

Figure 5.36: Visualization of the simulated trajectory of the PERA (5DoF)

Experiments (5 DoF)

Next, experiments with the PERA are conducted. The α controller gains are selected as in (5.44). Moreover, the other controller gains are selected as

$$\beta = \begin{bmatrix} 400 \\ 100 \\ 120 \\ 50 \\ 50 \end{bmatrix} \quad K_c = \mathrm{diag}\{30,\ 20,\ 200,\ 0.1,\ 0.1\} \quad R_c = \mathrm{diag}\{0.0001,\ 0.00001,\ 0.055,\ 0.0001,\ 0.0001\} \tag{5.46}$$

In the first experiments, a new issue with the elbow of the PERA arised. Due to inequalities between the two elbow motors, the elbow yaw joint (Y_E) exhibited undesired motion. Since incorporation of the second elbow joint in the control would lead to tighter restrictions on the magnitude of the control signal for the elbow pitch joint, it was decided to deal with the motion of the elbow yaw joint by altering the inputs to the wrist joints, such that

$$
\begin{aligned}
q_{d,4,\text{new}} =& q_{d,4}\cos(Y_E) + q_{d,5}\sin(Y_E)\\
q_{d,5,\text{new}} =& -q_{d,4}\sin(Y_E) + q_{d,5}\cos(Y_E)\\
\left[\frac{\partial V}{\partial q_4}\right]_{new} =& \frac{\partial V}{\partial q_4}\cos(Y_E) + \frac{\partial V}{\partial q_5}\sin(Y_E)\\
\left[\frac{\partial V}{\partial q_5}\right]_{new} =& -\frac{\partial V}{\partial q_4}\sin(Y_E) + \frac{\partial V}{\partial q_5}\cos(Y_E)\\
\gamma_{4,\text{new}} =& \gamma_4\cos(Y_E) + \gamma_5\sin(Y_E)\\
\gamma_{5,\text{new}} =& -\gamma_4\sin(Y_E) + \gamma_5\cos(Y_E).
\end{aligned}
\tag{5.47}
$$

The experimental results are shown in Figure 5.37.

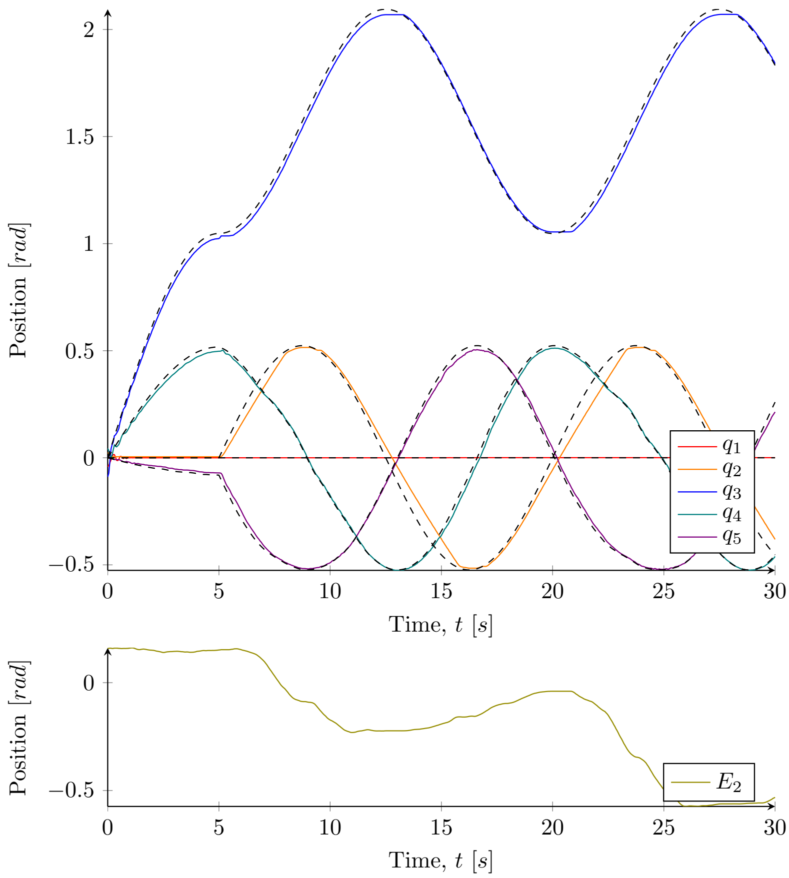

Figure 5.37: Experimental results (5DoF). The colored lines represent the position of the joints during the experiment. The dashed lines represent the desired positions.

By zooming in to the first two seconds of the experiment, it is found that convergence is successful (Figure 5.38). Furthermore, by observing the position errors in Figure 5.39, it is found that the magnitude of these errors is within the same range as that of the second and third joint. Compared to the experiments with three DoF (Figure 5.8), the magnitude of the error on the position of the second joint is larger in the new experiments. The first and third joint, however, show the same behaviour as in the three DoF case. The magnitude of the position errors on the wrist joints are of the same order as those of the elbow joint. Moreover, it should be noted that, while the controller

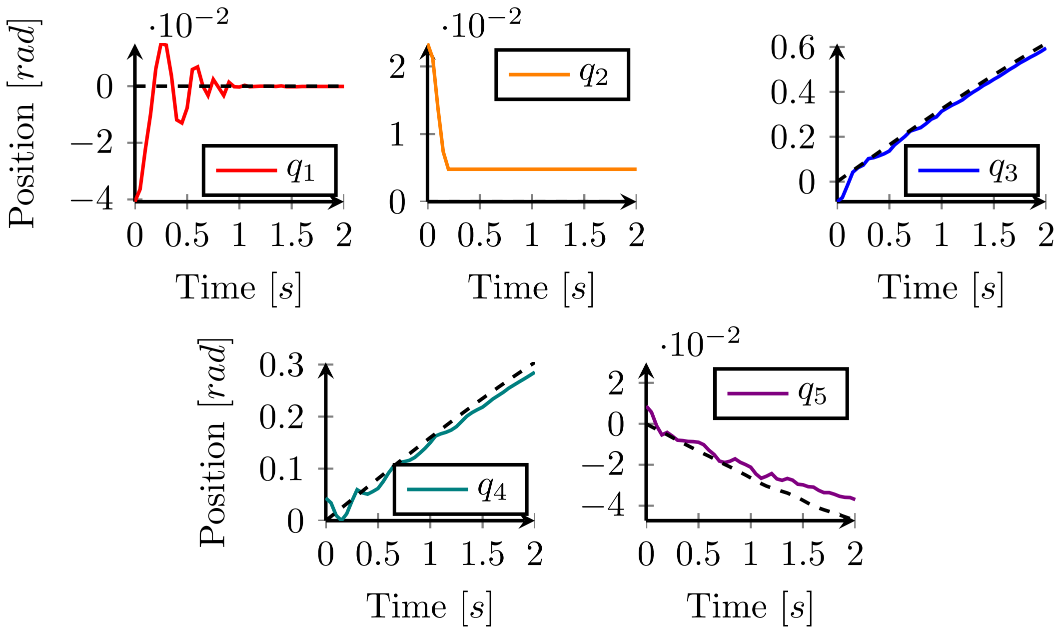

Figure 5.38: First two seconds of the simulation results (5 DoF)

gains of the elbow did not change with respect to the gains in the three DoF experiment, the shaking did return to the motion of the joint. This is caused by the fact that the amplitude of this joint is increased in the five DoF experiments.

Figure 5.40 depicts the input to the motors during the experiments. Clearly, the input signals match the motion of the joints in Figure 5.37. As in the experiments with three DoF, the figure shows oscillations in the input signal of the elbow pitch joint (q_3), especially when the motion of the joint is downward.

The trajectory followed by the PERA in the experiment is visualized in Figure 5.41. From comparison to Figure 5.33 it can be seen that the followed trajectory is close to the desired trajectory, although errors in the five joints make the curves of the circle less appealing than the results with the three DoF arm. Due to these errors, it was deemed impossible to draw a circle without using some drawing enhancement technique.

First, to allow the PERA with five DoF to draw, the possibilities for using the previously proposed heuristic approach for drawing enhancement are investigated. However, in the new experiments, there are forces arising from the motion of the wrist, such that disturbances arising from the canvas cannot be distinguished by the wrist force sensors. Therefore, the following new heuristic approach for drawing enhancement is proposed.

$$q_{d,1,\text{new}}(k) = q_{d,1}(t(k)) - c(k), \tag{5.48}$$

where

$$c(k) = \begin{cases} c(k-1) + 0.002, & \text{if } \tilde{q}(k)^\top \tilde{q}(k) > l_1 \\ c(k-1) - 0.002, & \text{if } \tilde{q}(k)^\top \tilde{q}(k) < l_2 \text{ and } c(k-1) > 0, \end{cases} \tag{5.49}$$

with

$$\begin{aligned} l_1(k) =& 0.1 \\ l_2(k) =& 0.05. \end{aligned} \tag{5.50}$$

These limits are defined such that they are never exceeded when there is no disturbance from the canvas. Using the proposed heuristic approach, several attempts were made to draw the circle.

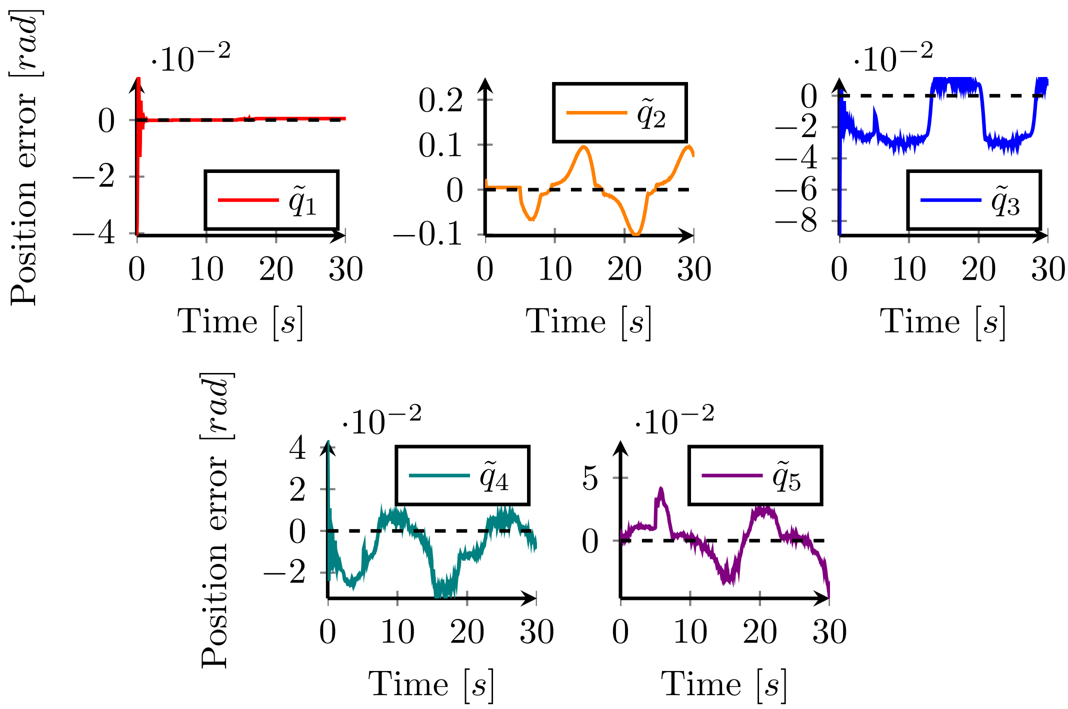

Figure 5.39: Position errors in the experiment (5 DoF)

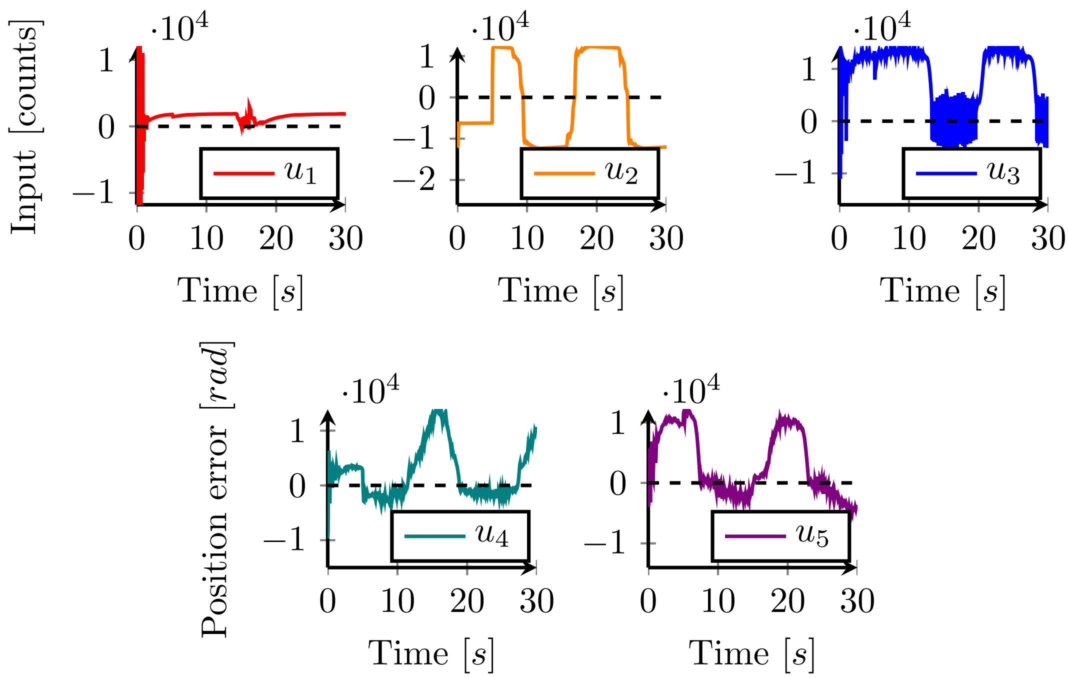

Figure 5.40: Input signals in the experiment (5 DoF)

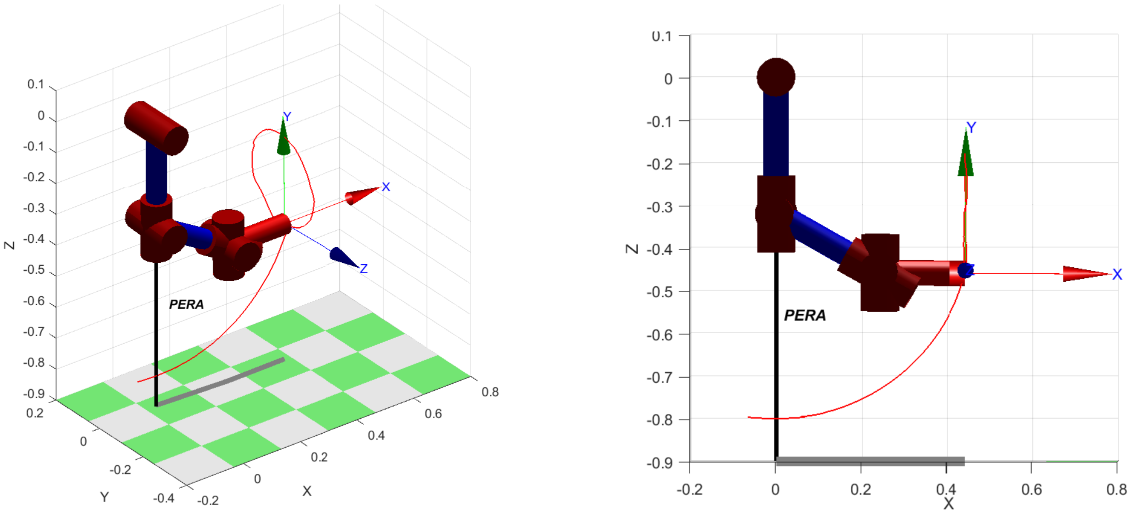

(a) 3D view (b) Side view

Figure 5.41: Visualization of the trajectory covered by the PERA in experiments (5DoF)

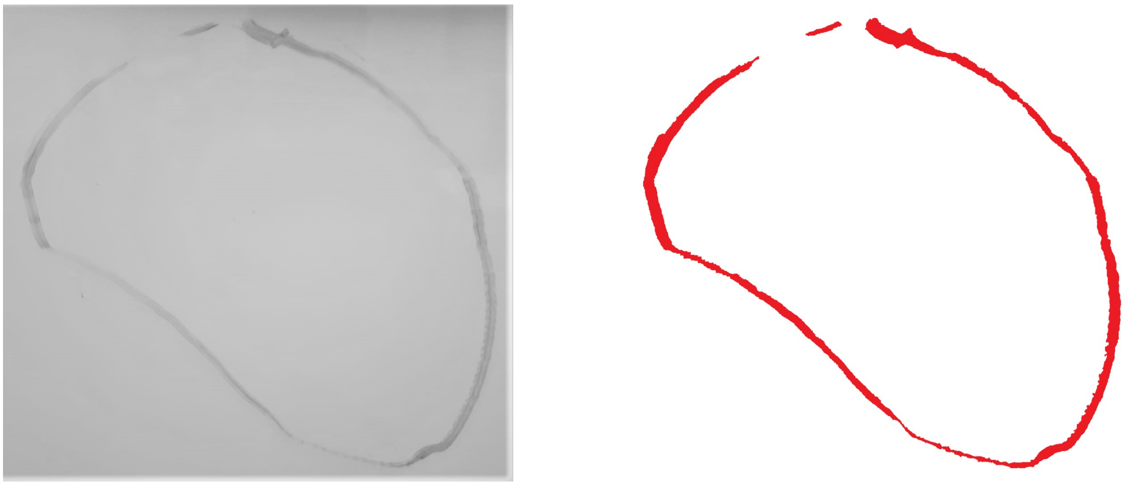

(a) Photo (b) Edited

Figure 5.42: Attempted circle drawing (5 DoF)

Unfortunately, the approach did not improve the drawing as desired. The result is in Figure 5.42. Due to time constraints in the project, it was not possible to test another approach. Again, to perform a more successful drawing routine is a subject of future work. Presumably, implementing a force control strategy on the shoulder pitch joint would yield better results.

Chapter 6

Conclusion and future work

In this concluding chapter, the main contributions presented in this thesis are summarized. The control law and results are discussed, as well as the drawing routine. Other contributions are mentioned and insights about the tuning of the controller gains are provided. Furthermore, recommendations for future work in the line of this research are provided.

6.1 Concluding remarks

In this work, a PBC approach for trajectory tracking was developed for the PERA. In theory, the controller globally asymptotically stabilizes the system on the desired trajectory. Furthermore, the control law proposed in this work is naturally saturated and does not require velocity measurements. The control law uses gravity compensation, which is based on accurate modeling of the gravitational force action on the PERA. Moreover, it is not necessary to solve any partial differential equations when this control approach is used. The control approach proposed was validated by executing a drawing routine with the PERA.

In the conducted experiments, it was found that with the appropriate tuning of the controller gains, the desired trajectory was followed with a minor steady-state error. Especially for the shoulder pitch joint, which is actuated by relatively high-power motors, the saturated control law performed well, such that the steady-state error converged to a very low value ($\max\{\tilde{q}_1\} = 3.00 \cdot 10^{-4}$). As was shown by van den Bos (2019), for SPR, the steady-state errors could be eradicated by introducing an integral gain in the controller, at the cost of the global property of the theoretical asymptotic stability of the closed-loop system. For trajectory tracking, however, this is not the case, because the desired positions are time-dependent. Although the introduction of an integral gain might improve the results, it was decided not to do this, because for the drawing routine, other factors had a more significant impact on the quality of the drawings produced by the PERA. While the errors in the joint positions were generally small, the positioning of the canvas to draw on and the offsets of the position sensors were considered to have a greater influence on the quality of the drawing routine.

Therefore, a heuristic approach was developed to update the desired positions of the joints based on the force exerted by the canvas on the PERA, such that the quality of the drawings produced by the PERA was enhanced.

Moreover, the performance of the proposed control law was compared to the performance of a non-saturated variant. For both control laws, the controller gains were tuned to the desired performance. It was concluded that the performance of the saturated control law is better in terms of steady-state position errors, as long as the power of the actuating motors is slightly larger than the minimally required power. The total energy used does not differ much between the two control laws.

Further contributions of this work are

- the design of polynomial approximations of the behaviour of the non-linear amplifiers in the motors. These polynomials relate the current over the motors to the signal in counts.

- the solving of issues in the existing controller code of the PERA, such as

  - errors in the motor and gearing parameters used to translate the desired torque to a motor input.
  - an error in the sensor used to measure the position of the shoulder pitch. Originally, the desired position of the shoulder pitch was compared to the position of the shoulder yaw.
  - an error in the coded limitations on the RoM of joints. Originally, the shoulder pitch joint was limited at $0 \leq q_1 \leq \frac{\pi}{2}$, such that the desired position could not be set to a negative value.

- several insights about the tuning of the proposed control law. In these findings the experimental performance of the elbow pitch joint is not considered, since it was tuned to remove the shaking from the motion of the joint. This tuning did not necessarily result in the best performance in terms of convergence.
  - The value of α should be set as high as possible while maintaining the saturation limits of the control signal, such that the full potential of the motor can be used for actuation.
  - To minimize the steady-state error, the value of β should be set to a high value, such that when the position error is small, the input remains strong enough to make the joint move closer to the desired trajectory. When the position error is relatively large, however, a large value of β will cause the magnitude of the input signal to be close to the maximum input signal. If the value of α is large, this will result in overshoot or oscillations in the motion of the joint. Therefore, best performance will be achieved with this control law if the system is initialized close to the desired starting position.
  - The tuning of the values of elements of the K_c matrix remains a bit vague. In this research, K_c was chosen as a diagonal matrix. In simulations, different values $(0.1 \sim 30)$ resulted in the best performance of the control law on different joints. Similarly, in the experiments, a wide range of values $(0.1 \sim 200)$ yielded the best results. The difference in tuning between simulations and experiments is most likely caused by the natural damping of the PERA, which is not considered in the model that was used for simulations.
  - Furthermore, the tuning of the values in the R_c matrix, remains vague as well. As is the case for the K_c matrix, R_c was chosen as a diagonal matrix in this work. It is clear that the values should be relatively small, since higher values cause oscillations in the value of x_c, which are amplified in the control signal. In the simulations, the values ranged between 0.11 and 1.5, while in the experiments, the best results were obtained with values of a much smaller magnitude $(1.0 \cdot 10^{-5} \sim 1.0 \cdot 10^{-4})$. Again, this difference is presumably caused by the natural damping of the PERA.

6.2 Future work

In this work, the simulations and experimental results obtained with the proposed control law have been presented. The findings in this work give rise to several opportunities for future work on the control law, drawing routine and PERA.

During the transition from simulations to experiments, it was found that the natural damping of the mechanical system has a significant influence on the behaviour of the system. Therefore, it is recommended to test the control law on mechanical systems where the natural damping of the system is known. This will decrease the effort in the transition from simulations to experiments, such that new insights in the tuning of the control law can be obtained. Furthermore, new trajectories can be investigated in experiments, possibly using more DoF. For instance, Dr. Daniel Dirkz, who is an university contact at Philips Drachten, mentioned during a short visit that a possible trajectory would be to mimic the motion of a human shaving. Experiments with these types of trajectories would make the research more interesting from a business perspective. Another opportunity for future research would be the introduction of variable controller gains. For example, the value of β can be set to be dependent on time or error, such that the motion of the joints will be smooth for large errors while ensuring a small steady-state error. Another example would be to define the value of α such that the full potential of the motors can be used, regardless of the magnitude of the gravity compensating component. Moreover, the effects of selecting the gain matrices K_c and R_c as positive definite matrices in stead of diagonal matrices may be investigated.

There are several options to enhance the results of the drawing routine, e.g., the drawing enhancement heuristic proposed in this work may be adapted by considering other force sensors, joints and limits. This will allow the drawing of more complex shapes. Another approach could be to use a force control strategy to maintain a constant pressure on the canvas. In addition, visual control may be applied to determine the orientation of the canvas in the Cartesian space. Using the orientation of the canvas, a set of points on the canvas can be constructed, which can then be translated into a desired trajectory in joint space by computing the inverse kinematics. Furthermore, the ideal drawing angle between the marker and canvas can be investigated. This will allow a smooth motion of the marker over the canvas.

Finally, there are some suggestions for future work on the mechanical system of the PERA itself. Most importantly, the sensors should be re-calibrated, such that the sensor signals correspond closely to the actual joint positions. Furthermore, a recommendation is to experimentally determine an approximation of the natural damping of the system, such that this can be included in the modeling and simulation. Finally, the cause of the shaking of the elbow joint should be determined to solve this issue.

Bibliography

Albertos, P. et al. (1997). *Control engineering solutions: a practical approach.* 54. Iet.

Astolfi, A., R. Ortega, and A. Venkatraman (2010). "A globally exponentially convergent immersion and invariance speed observer for mechanical systems with non-holonomic constraints". In: *Automatica* 46.1, pp. 182–189.

Aström, K.J. and R.M. Murray (2010). *Feedback systems: an introduction for scientists and engineers.* Princeton university press.

Atkinson, K.E. (2008). *An introduction to numerical analysis.* John wiley & sons.

Bai, H., M. Arcak, and J. Wen (2011). *Cooperative control design: a systematic, passivity-based approach.* Springer Science & Business Media.

Bögel, Nering (2012). "Modeling and PID-control for a 5 degrees of freedom robotic arm". Bachelor's thesis. University of Groningen.

Bol, M.E. (2012). "Force and position control of the Philips Pxperimental Robot Arm in an energy based setting". MA thesis. University of Groningen.

Bos, F. van den (2019). "A pouring application for the Philips Experimental Robotic Arm, using saturated passivity-based control without velocity measurements". MA thesis. University of Groningen.

Corke, P.I. et al. (1996). "A robotics toolbox for MATLAB". In: *IEEE Robotics & Automation Magazine* 3.1, pp. 24–32.

Craig, J.J. (2009). *Introduction to robotics: mechanics and control, 3/E.* Pearson Education India.

Denavit, J. and R.S. Hartenberg (1955). "A kinematic notation for lower pair mechanisms based on matrices". In: *Journal of applied mechanics* 77.2, pp. 215–221.

Dereniowski, D. and M. Kubale (2003). "Cholesky factorization of matrices in parallel and ranking of graphs". In: *International Conference on Parallel Processing and Applied Mathematics.* Springer, pp. 985–992.

Dirksz, D.A. and J.M.A. Scherpen (2010). "Power-based adaptive and integral control of standard mechanical systems". In: *49th IEEE Conference on Decision and Control (CDC).* IEEE, pp. 4612–4617.

Dirksz, D.A., J.M.A. Scherpen, and R. Ortega (2008). "Interconnection and Damping Assignment Passivity-Based Control for Port-Hamiltonian mechanical systems with only position measurements". In: *2008 47th IEEE Conference on Decision and Control.* IEEE, pp. 4957–4962.

Duindam, Vincent et al. (2009). *Modeling and control of complex physical systems: the port-Hamiltonian approach.* Springer Science & Business Media.

Elhami, M.R. and I. Dashti (2016). "A New Approach to the Solution of Robot Kinematics Based on Relative Transformation Matrices". In: *International Journal of Robotics and Automation (IJRA)* 5.3, pp. 213–222.

Fujimoto, K. and T. Sugie (Mar. 2001). "Canonical transformation and stabilization of generalized Hamiltonian systems". In: *Systems & Control Letters* 42, pp. 217–227. DOI: 10.1016/S0167-6911(00)00091-8.

Hancock, E.J. and A. Papachristodoulou (2012). "An invariance principle for time-varying systems". In: *2012 IEEE 51st IEEE Conference on Decision and Control (CDC)*. IEEE, pp. 4597–4602.

Harmo, Panu et al. (2005). "Needs and solutions-home automation and service robots for the elderly and disabled". In: *2005 IEEE/RSJ international conference on intelligent robots and systems*. IEEE, pp. 3201–3206.

Jong, M.C. de (2013). "Soft touch and dexterous controlled movement for the gripper of the Philips Experimental Robot Arm". Bachelor's thesis. University of Groningen.

Khalil, H.K. (2002). *Nonlinear Systems*. Pearson Education. Prentice Hall. ISBN: 9780130673893.

Koops, F. (2014). "Trajectory tracking control of the philips experimental robot arm in the port-hamiltonian framework". MA thesis. University of Groningen.

Krasovskii, N.N. (1963). "Stability of motion". In: *Stanford University Press*.

LaSalle, J.P. (1960). "Some extensions of Liapunov's second method". In: *IRE Transactions on circuit theory* 7.4, pp. 520–527.

Leeuwerik, C.P. (2015). "Implementation of force control in a Philips experimental robotic arm". MA thesis. University of Groningen.

Lin, Patrick, George Bekey, and Keith Abney (2008). *Autonomous military robotics: Risk, ethics, and design*. Tech. rep. California Polytechnic State Univ San Luis Obispo.

Lyapunov, A.M. (1992). "The general problem of the stability of motion". In: *International journal of control* 55.3, pp. 531–534.

Ma, Y-M. and G-H. Yang (2008). "Performance analysis for linear discrete-time systems subject to actuator saturation". In: *2008 American Control Conference*. IEEE, pp. 3608–3613.

Maschke, B.M. and A.J. van der Schaft (1992). "Port-controlled hamiltonian systems: modelling origins and systemtheoretic properties". In: *IFAC Proceedings Volumes* 25.13, pp. 359–365.

Maxon Group (n.d.). *RE 30 Ø30 mm, Graphite Brushes, 60 Watt*. URL: `https://www.maxongroup.com/maxon/view/product/motor/dcmotor/re/re30/268216?etcc_cu=onsite&etcc_med=Header%20Suche&etcc_cmp=mit%20Ergebnis&etcc_ctv=Layer&query=268216`.

Meinsma, G. and A.J. van der Schaft (2018). *Calculus of Optimal Control*. Lecture Notes for WIVOB-09. University of Groningen.

Mendels, J.D. (2011). "Modeling and linear control for a humanoid robot arm manipulator". Bachelor's thesis. University of Groningen.

Muñoz-Arias, M. (2015). "Energy-based Control Design for Mechanical Systems: Applications of the Port-Hamiltonian Approach". PhD thesis. University of Groningen.

Okamura, Allison M, Maja J Mataric, and Henrik I Christensen (2010). "Medical and health-care robotics". In: *IEEE Robotics & Automation Magazine* 17.3, pp. 26–37.

Ortega, R. and M.W. Spong (1989). "Adaptive motion control of rigid robots: A tutorial". In: *Automatica* 25.6, pp. 877–888.

Ortega, R. et al. (2002). "Interconnection and damping assignment passivity-based control of port-controlled Hamiltonian systems". In: *Automatica* 38.4, pp. 585–596.

Ortega, R. et al. (2013). "Passivity-based control of Euler-Lagrange systems: mechanical, electrical and electromechanical applications". In:

Rijs, R. et al. (2014). *Philips experimental robot arm, user instruction manual v1.1*. Philips.

Romero, J.G., R. Ortega, and I. Sarras (2014). "A globally exponentially stable tracking controller for mechanical systems using position feedback". In: *IEEE Transactions on Automatic Control* 60.3, pp. 818–823.

Schaft, A.J. van der (2000). *L2-gain and passivity techniques in nonlinear control*. Vol. 2. Springer.

— (2004). "Port-Hamiltonian systems: network modeling and control of nonlinear physical systems". In: *Advanced dynamics and control of structures and machines*. Springer, pp. 127–167.

Schaft, A.J. van der and J.M.A. Scherpen (2014a). *Modeling & Control of Complex Nonlinear Engineering Systems, Part II.* Lecture Notes for WIMCCNES12. University of Groningen.

— (2014b). *Modeling & Control of Complex Nonlinear Engineering Systems, Part III.* Lecture Notes for WIMCCNES12. University of Groningen.

— (2018). *Modeling & Control of Complex Nonlinear Engineering Systems, Part I.* Lecture Notes for WIMCCNES12. University of Groningen.

Serway, R.A. and J.W. Jewett (2018). *Physics for scientists and engineers with modern physics.* Cengage learning.

Siciliano, B. and O. Khatib (2016). *Springer handbook of robotics.* Springer.

Siemonsma, J. (2014). "Design and implementation of a nonlinear force controller for the Philips Experimental Robot Arm". Bachelor's thesis. University of Groningen.

Spong, M.W. and M. Vidyasagar (2008). *Robot dynamics and control.* John Wiley & Sons.

Stover, C. and E.W. Weisstein (n.d.). *Parametric Equations. From MathWorld–A Wolfram Web Resource.* Last visited on 27/1/2020. URL: `%5Curl%7Bhttp://mathworld.wolfram.com/ParametricEquations.html%7D`.

Veltman, A. (2019). "Pick and place routines with a flexible joint robotic arm using passivity-based control". MA thesis. University of Groningen.

Venkatraman, A. et al. (2010). "Speed observation and position feedback stabilization of partially linearizable mechanical systems". In: *IEEE Transactions on Automatic Control* 55.5, pp. 1059–1074.

Viola, G. et al. (2007). "Total energy shaping control of mechanical systems: simplifying the matching equations via coordinate changes". In: *IEEE Transactions on Automatic Control* 52.6, pp. 1093–1099.

Weisstein, E.W. (n.d.[a]). *Heart Curve. From MathWorld–A Wolfram Web Resource.* Last visited on 27/1/2020. URL: `%5Curl%7B%20http://mathworld.wolfram.com/HeartCurve.html%7D`.

— (n.d.[b]). *Lemniscate. From MathWorld–A Wolfram Web Resource.* Last visited on 27/1/2020. URL: `%5Curl%7Bhttp://mathworld.wolfram.com/Lemniscate.html%7D`.

Wesselink, T.C. (2018). "Non-linear saturated control without velocity measurements for planar, flexible-joint manipulators". MA thesis. University of Groningen.

Wesselink, T.C., P. Borja, and J.M.A. Scherpen (2018). "Saturated control without velocity measurements for planar robots with flexible joints". In: *arXiv preprint arXiv:1812.08257*.

Appendices

Appendix A

PERA wiring

On the next page, the wiring diagram of the PERA is shown (Rijs et al., 2014). It should be noted that in the current setup, the force sensor of the gripper is connected to the wrist board (4) in stead of the grippers own board (3). For more information on these wiring changes, see (Leeuwerik, 2015; van den Bos, 2019).

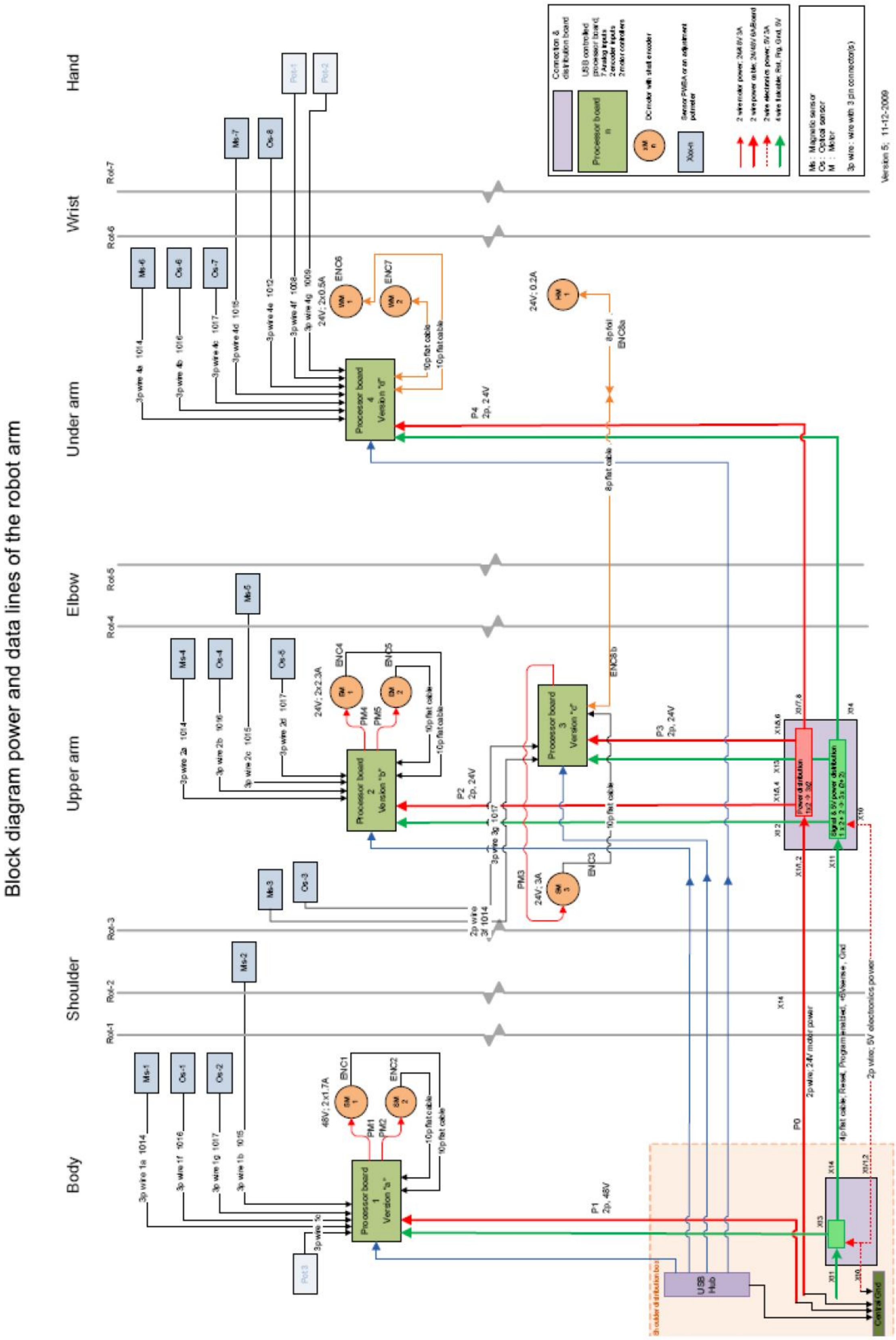
Block diagram power and data lines of the robot arm
Body
Shoulder
Upper arm
Elbow
Under arm
Wrist
Hand
Rot-1
Rot-2
Rot-3
Rot-4
Rot-5
Rot-6
Rot-7
Processor board 1 Version "a"
Processor board 2 Version "b"
Processor board 3 Version "c"
Processor board 4 Version "d"
P0
P1 2p, 48V
P2 2p, 24V
P3 2p, 24V
P4 2p, 24V
48V; 2x1.7A
24V; 2x2.3A
24V; 3A
24V; 2x0.5A
24V; 0.2A
USB Hub
Central Gnd
2p wire; 24V motor power
2p wire; 5V electronics power
Version 5; 11-12-2009

Appendix B

Data-sheets Maxon parts

Since the data-sheets of the Hall angle sensors produced by AMS are quite comprehensive, they are not added here. The data-sheets can be found on `https://ams.com/documents/20143/36005/AS5040_DS000374_3-00.pdf/c4dd3ec3-24f4-f3a2-0eca-811af6c30c84` (AS5040) and `https://ams.com/documents/20143/36005/AS5145_DS000398_1-00.pdf/4964e511-a5bd-4e73-2d33-5259e407a179` (AS5145). Table B.1 lists the joints of the PERA and the corresponding Maxon Motors parts.

Joint(s)	**Motor(s)**	**Motor Part No.**	**Gearing Part No.**	**Encoder Part No.**
q_1	S_1 and S_2	268216	166940	225783
q_2	S_3	268214	166940	225783
q_3	E_1 and E_2	118752	166938	225778
q_4 and q_5	W_1 and W_2	110164	143979	228177
	G	118641	110314	323052

Table B.1: Maxon part numbers

The following pages contain the data-sheets of the Maxon parts in the following order.

- Data-sheet motors q_1 and q_2.
- Data-sheet motors q_3.
- Data-sheet motors q_4 and q_5.
- Data-sheet motor gripper.
- Data-sheet gearings q_1, q_2 and q_3.
- Data-sheet gearings q_4 and q_5.
- Data-sheet gearing gripper.
- Data-sheet encoders q_1 and q_2.
- Data-sheet encoders q_3.
- Data-sheet encoders q_4 and q_5.
- Data-sheet encoder gripper.

The data-sheets are taken from the Maxon catalog (`https://www.maxongroup.com/`).

RE 30 ∅30 mm, Graphite Brushes, 60 Watt

maxon RE motor

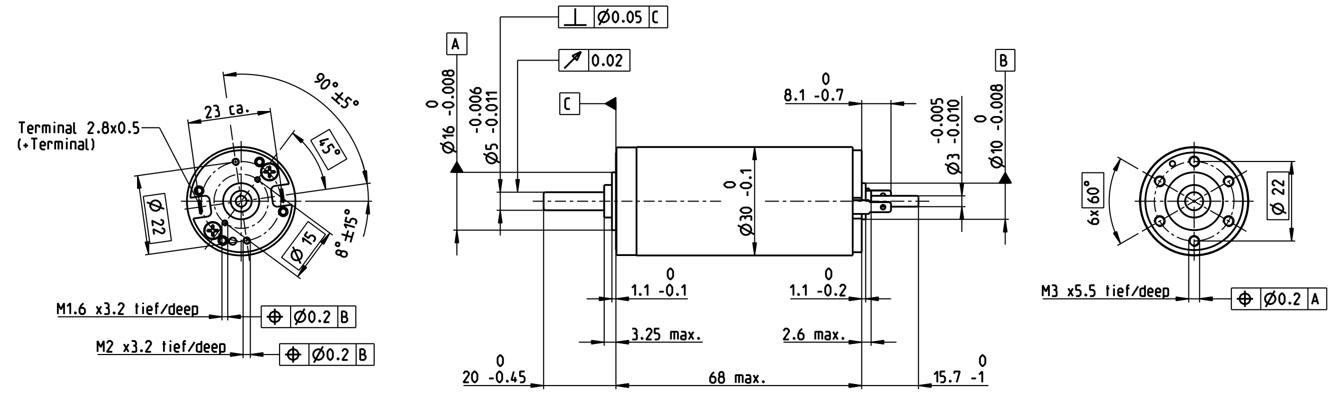

M 1:2

Stock program
Standard program
Special program (on request)

	Part Numbers				
according to dimensional drawing	310005	310006	310007	310008	310009
shaft length 15.7 shortened to 8.7 mm	268193	268213	268214	268215	268216
Motor Data					
Values at nominal voltage					
1 Nominal voltage V	12	18	24	36	48
2 No load speed rpm	8170	8590	8810	8590	8490
3 No load current mA	301	213	165	106	78.6
4 Nominal speed rpm	7630	7910	8050	7840	7760
5 Nominal torque (max. continuous torque) mNm	51.6	75.5	85.6	86.6	89.7
6 Nominal current (max. continuous current) A	4	4	3.47	2.28	1.74
7 Stall torque mNm	853	1000	1020	1000	1050
8 Stall current A	61.1	50.3	39.3	25.2	19.6
9 Max. efficiency %	85	87	87	87	88
Characteristics					
10 Terminal resistance Ω	0.196	0.358	0.611	1.43	2.45
11 Terminal inductance mH	0.034	0.07	0.119	0.281	0.513
12 Torque constant mNm/A	13.9	19.9	25.9	39.8	53.8
13 Speed constant rpm/V	685	479	369	240	178
14 Speed / torque gradient rpm/mNm	9.64	8.61	8.7	8.61	8.09
15 Mechanical time constant ms	3.4	3.24	3.05	2.98	2.94
16 Rotor inertia gcm^2	33.7	35.9	33.5	33.1	34.7

Specifications

Thermal data
17 Thermal resistance housing-ambient 6.0 K/W
18 Thermal resistance winding-housing 1.7 K/W
19 Thermal time constant winding 16.3 s
20 Thermal time constant motor 593 s
21 Ambient temperature -30…+100°C
22 Max. winding temperature +125°C

Mechanical data (ball bearings)
23 Max. speed 12000 rpm
24 Axial play 0.05 - 0.15 mm
25 Radial play 0.025 mm
26 Max. axial load (dynamic) 5.6 N
27 Max. force for press fits (static) 110 N
(static, shaft supported) 1200 N
28 Max. radial load, 5 mm from flange 28 N

Other specifications
29 Number of pole pairs 1
30 Number of commutator segments 13
31 Weight of motor 260 g

Values listed in the table are nominal.
Explanation of the figures on page 68.

Option
Preloaded ball bearings

Operating Range

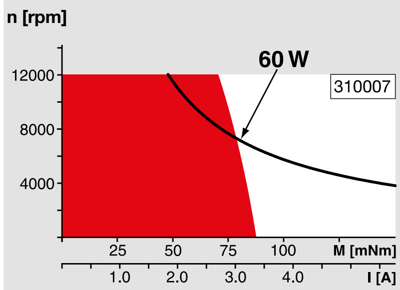

Comments

Continuous operation
In observation of above listed thermal resistance (lines 17 and 18) the maximum permissible winding temperature will be reached during continuous operation at 25°C ambient.
= Thermal limit.

Short term operation
The motor may be briefly overloaded (recurring).

Assigned power rating

maxon Modular System

Details on catalog page 32

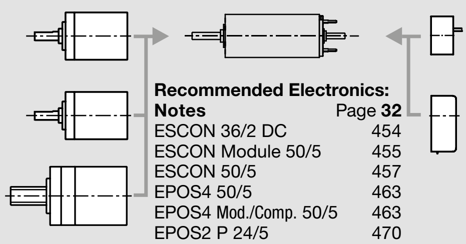

Planetary Gearhead
∅32 mm
0.75 - 6.0 Nm
Page 348–355

Koaxdrive
∅32 mm
1.0 - 4.5 Nm
Page 359

Screw Drive
∅32 mm
Page 382–387

Recommended Electronics:

Notes	Page **32**
ESCON 36/2 DC	454
ESCON Module 50/5	455
ESCON 50/5	457
EPOS4 50/5	463
EPOS4 Mod./Comp. 50/5	463
EPOS2 P 24/5	470
MAXPOS 50/5	473

Encoder MR
256 - 1024 CPT,
3 channels
Page 433

Encoder HED_ 5540
500 CPT,
3 channels
Page 440/442

RE 25 ∅25 mm, Graphite Brushes, 20 Watt

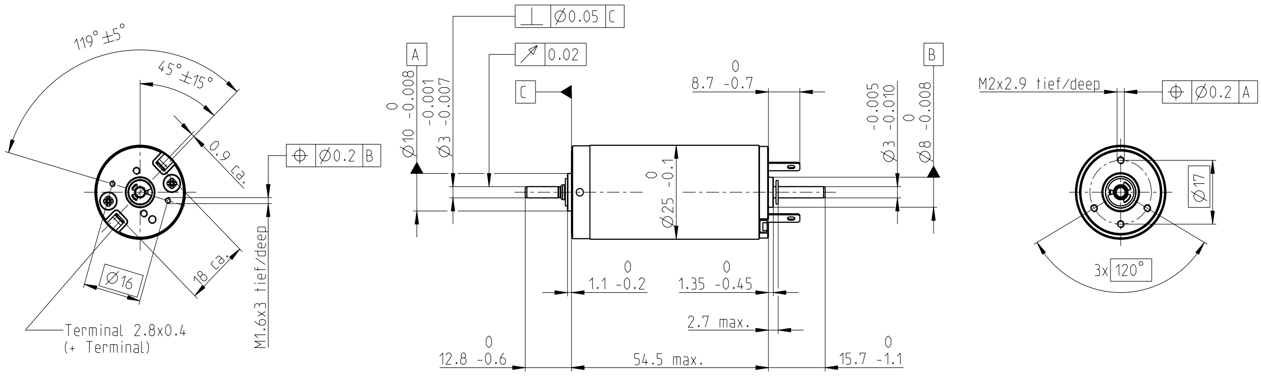

M 1:2

Stock program
Standard program
Special program (on request)

Part Numbers

		1	2	3	4	5	6	7	8	9
according to dimensional drawing		118749	118750	118751	118752	118753	118754	118755	118756	118757
shaft length 15.7 shortened to 4 mm		302002	302003	302004	302005	302006	302007	302001	302008	302009
Motor Data										
Values at nominal voltage										
1 Nominal voltage	V	9	15	18	24	30	42	48	48	48
2 No load speed	rpm	10000	9660	10200	9560	9860	11100	10300	8240	5050
3 No load current	mA	110	60.8	53.9	36.9	30.5	25.2	20.1	15.2	8.52
4 Nominal speed	rpm	8970	8430	8850	8330	8640	9920	9160	7040	3830
5 Nominal torque (max. continuous torque)	mNm	11.1	20.5	22.9	26.3	26.7	27.1	27.7	28.7	30
6 Nominal current (max. continuous current)	A	1.5	1.5	1.46	1.16	0.968	0.784	0.653	0.536	0.343
7 Stall torque	mNm	232	225	220	243	249	283	264	209	129
8 Stall current	A	29.1	15.8	13.5	10.4	8.72	7.94	6.03	3.81	1.44
9 Max. efficiency	%	76	82	83	85	86	87	87	86	84
Characteristics										
10 Terminal resistance	Ω	0.309	0.952	1.33	2.32	3.44	5.29	7.96	12.6	33.4
11 Terminal inductance	mH	0.028	0.088	0.115	0.238	0.353	0.551	0.832	1.31	3.48
12 Torque constant	mNm/A	7.96	14.3	16.3	23.4	28.5	35.6	43.8	55	89.6
13 Speed constant	rpm/V	1200	670	586	408	335	268	218	174	107
14 Speed / torque gradient	rpm/mNm	46.5	44.7	48	40.3	40.4	39.8	39.6	39.8	39.7
15 Mechanical time constant	ms	5.68	4.87	4.77	4.55	4.47	4.4	4.37	4.37	4.35
16 Rotor inertia	gcm^2	11.7	10.4	9.49	10.8	10.6	10.6	10.5	10.5	10.5

Specifications

Thermal data

17	Thermal resistance housing-ambient	14 K/W
18	Thermal resistance winding-housing	3.1 K/W
19	Thermal time constant winding	12.5 s
20	Thermal time constant motor	612 s
21	Ambient temperature	-30…+100°C
22	Max. winding temperature	+125°C

Mechanical data (ball bearings)

23	Max. speed	14000 rpm
24	Axial play	0.05 - 0.15 mm
25	Radial play	0.025 mm
26	Max. axial load (dynamic)	3.2 N
27	Max. force for press fits (static)	64 N
	(static, shaft supported)	800 N
28	Max. radial load, 5 mm from flange	16 N

Other specifications

29	Number of pole pairs	1
30	Number of commutator segments	11
31	Weight of motor	130 g

Values listed in the table are nominal.
Explanation of the figures on page 68.

Option
Preloaded ball bearings

Operating Range

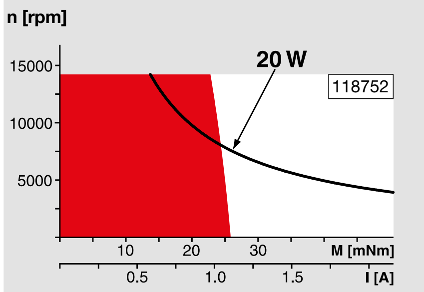

Comments

Continuous operation
In observation of above listed thermal resistance (lines 17 and 18) the maximum permissible winding temperature will be reached during continuous operation at 25°C ambient.
= Thermal limit.

Short term operation
The motor may be briefly overloaded (recurring).

Assigned power rating

maxon Modular System

Details on catalog page 32

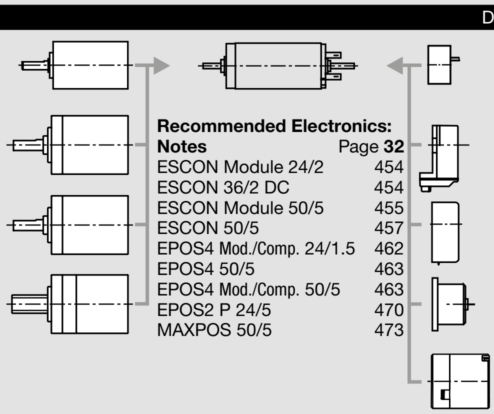

Planetary Gearhead
∅26 mm
0.75 - 4.5 Nm
Page 346

Planetary Gearhead
∅32 mm
0.75 - 6.0 Nm
Page 348/349/352

Koaxdrive
∅32 mm
1.0 - 4.5 Nm
Page 359

Screw Drive
∅32 mm
Page 382–387

Recommended Electronics:

Notes	Page **32**
ESCON Module 24/2	454
ESCON 36/2 DC	454
ESCON Module 50/5	455
ESCON 50/5	457
EPOS4 Mod./Comp. 24/1.5	462
EPOS4 50/5	463
EPOS4 Mod./Comp. 50/5	463
EPOS2 P 24/5	470
MAXPOS 50/5	473

Encoder MR
128 - 1000 CPT,
3 channels
Page 432

Encoder Enc
22 mm
100 CPT, 2 channels
Page 437

Encoder HED_ 5540
500 CPT,
3 channels
Page 440/442

DC-Tacho DCT
∅22 mm
0.52 V
Page 449

Brake AB 28
24 VDC
0.4 Nm
Page 491

maxon A-max

A-max 22 ∅22 mm, Graphite Brushes, 6 Watt

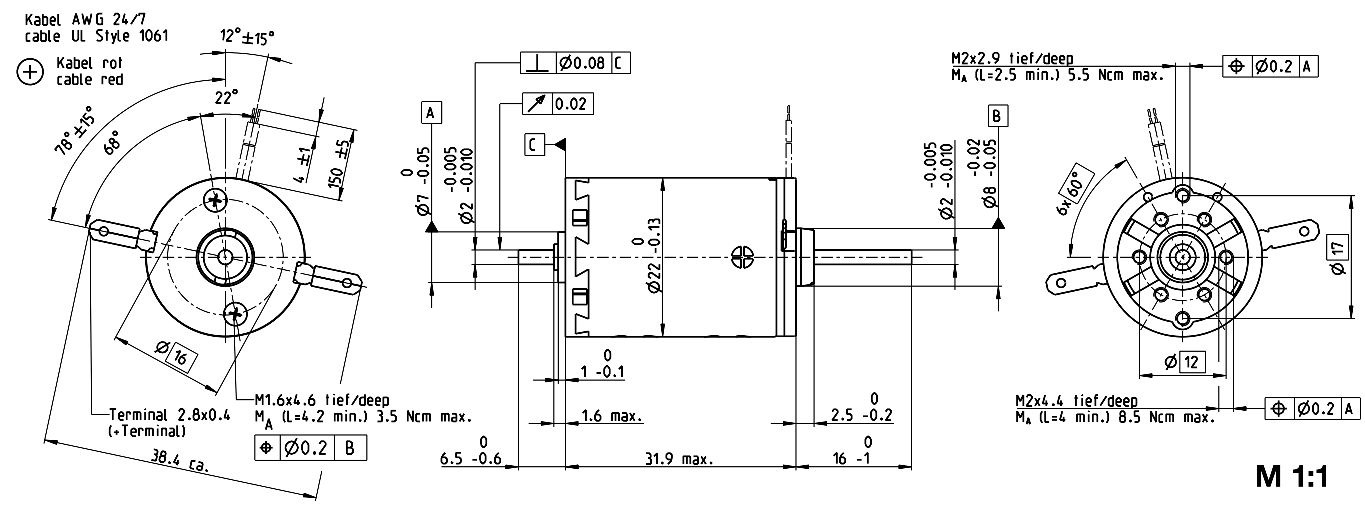

M 1:1

Stock program
Standard program
Special program (on request)

Part Numbers

with terminals		110156	110158	110159	110160	110161	110162	110163	110164	110165	110166	110167	110168
with cables		139848	353023	353024	231171	353025	353026	231174	353027	353028	353029	316659	353603
Motor Data													
Values at nominal voltage													
1 Nominal voltage	V	6	9	9	12	12	15	18	24	24	36	48	48
2 No load speed	rpm	9240	9690	8500	10200	9170	10000	9770	10500	8480	9630	9110	8210
3 No load current	mA	83.1	57.9	49.6	45.8	40.5	36	29	23.7	18.4	14.2	9.99	8.84
4 Nominal speed	rpm	6240	6530	5350	7060	6000	6890	6600	7380	5270	6420	5840	4940
5 Nominal torque (max. continuous torque)	mNm	5.91	6.88	7.04	6.96	6.95	6.93	6.92	6.9	6.97	6.86	6.75	6.86
6 Nominal current (max. continuous current)	A	1.08	0.859	0.77	0.681	0.613	0.534	0.432	0.347	0.283	0.21	0.147	0.135
7 Stall torque	mNm	19.4	22.1	19.8	23.7	20.9	22.9	22	23.7	18.9	21.1	19.2	17.6
8 Stall current	A	3.29	2.59	2.04	2.17	1.72	1.65	1.29	1.12	0.721	0.606	0.393	0.325
9 Max. efficiency	%	67	70	69	72	70	72	72	73	70	72	71	70
Characteristics													
10 Terminal resistance	Ω	1.82	3.48	4.42	5.53	6.96	9.09	14	21.5	33.3	59.4	122	148
11 Terminal inductance	mH	0.106	0.223	0.288	0.363	0.445	0.585	0.891	1.37	2.1	3.69	7.3	8.97
12 Torque constant	mNm/A	5.9	8.55	9.73	10.9	12.1	13.9	17.1	21.2	26.2	34.8	48.9	54.3
13 Speed constant	rpm/V	1620	1120	981	875	790	689	558	450	364	274	195	176
14 Speed / torque gradient	rpm/mNm	500	454	446	444	455	452	457	456	461	468	487	479
15 Mechanical time constant	ms	21.3	20.5	20.4	20.2	20.3	20.2	20.1	20.1	20.1	20.1	20.2	20.1
16 Rotor inertia	gcm^2	4.07	4.32	4.37	4.36	4.26	4.27	4.2	4.2	4.16	4.09	3.97	4.01

Specifications

Thermal data

17	Thermal resistance housing-ambient	20 K/W
18	Thermal resistance winding-housing	6.0 K/W
19	Thermal time constant winding	10.2 s
20	Thermal time constant motor	313 s
21	Ambient temperature	-30…+85°C
22	Max. winding temperature	+125°C

Mechanical data (sleeve bearings)

23	Max. speed	9800 rpm
24	Axial play	0.05 - 0.15 mm
25	Radial play	0.012 mm
26	Max. axial load (dynamic)	1 N
27	Max. force for press fits (static)	80 N
	(static, shaft supported)	440 N
28	Max. radial load, 5 mm from flange	2.8 N

Mechanical data (ball bearings)

23	Max. speed	9800 rpm
24	Axial play	0.05 - 0.15 mm
25	Radial play	0.025 mm
26	Max. axial load (dynamic)	3.3 N
27	Max. force for press fits (static)	45 N
	(static, shaft supported)	240 N
28	Max. radial load, 5 mm from flange	12.3 N

Other specifications

29	Number of pole pairs	1
30	Number of commutator segments	9
31	Weight of motor	54 g

Values listed in the table are nominal.
Explanation of the figures on page 68.

Option
Ball bearings in place of sleeve bearings

Operating Range

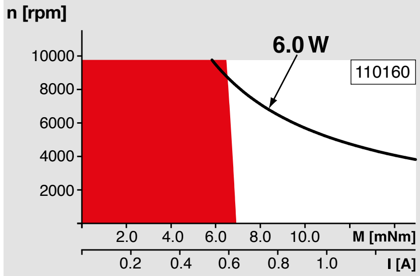

Comments

Continuous operation
In observation of above listed thermal resistance (lines 17 and 18) the maximum permissible winding temperature will be reached during continuous operation at 25°C ambient.
= Thermal limit.

Short term operation
The motor may be briefly overloaded (recurring).

Assigned power rating

maxon Modular System

Details on catalog page 32

Planetary Gearhead
∅22 mm
0.1 - 0.6 Nm
Page 337/338

Planetary Gearhead
∅22 mm
0.5 - 2.0 Nm
Page 339/341

Spur Gearhead
∅24 mm
0.1 Nm
Page 345

Screw Drive
∅22 mm
Page 380/381

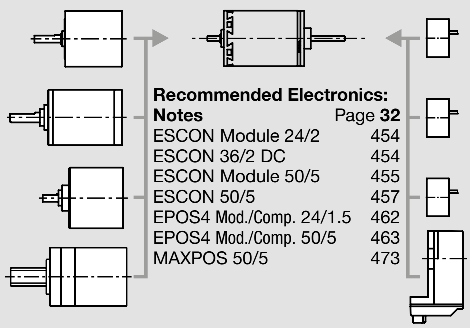

Recommended Electronics:

Notes	Page **32**
ESCON Module 24/2	454
ESCON 36/2 DC	454
ESCON Module 50/5	455
ESCON 50/5	457
EPOS4 Mod./Comp. 24/1.5	462
EPOS4 Mod./Comp. 50/5	463
MAXPOS 50/5	473

Encoder MEnc
∅13 mm
16 CPT, 2 channels
Page 417

Encoder MR
32 CPT,
2 / 3 channels
Page 429

Encoder MR
128 / 256 / 512 CPT,
2 / 3 channels
Page 430

Encoder Enc
22 mm
100 CPT, 2 channels
Page 437

April 2019 edition / subject to change

RE 13 ∅13 mm, Graphite Brushes, 3 Watt

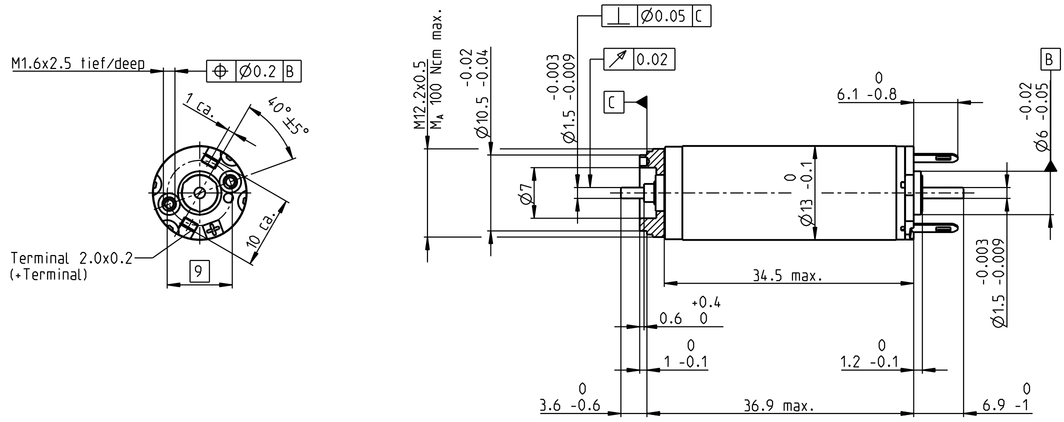

M 1:1

- Stock program
- Standard program
- Special program (on request)

Part Numbers

			118628	118629	118630	118631	118632	118633	118634	118635	118636	118637	118638	118639	118640	118641	118642
Motor Data																	
	Values at nominal voltage																
1	Nominal voltage	V	3	3.6	3.6	4.8	6	6	7.2	9	10	12	15	18	21	24	30
2	No load speed	rpm	12000	13600	11900	13600	13600	12100	13100	13800	13200	13300	13400	13000	14100	13800	14000
3	No load current	mA	168	164	136	121	95.5	81	75.3	64	53.9	45.4	36.8	29.2	28	23.8	19.5
4	Nominal speed	rpm	9520	10800	8780	10100	10300	8660	9790	10600	10100	10200	10400	9910	11100	10800	11000
5	Nominal torque (max. continuous torque)	mNm	1.22	1.32	1.58	1.92	2.05	2.17	2.12	2.17	2.32	2.3	2.31	2.36	2.29	2.33	2.28
6	Nominal current (max. continuous current)	A	0.72	0.72	0.72	0.72	0.602	0.558	0.495	0.422	0.383	0.319	0.259	0.212	0.192	0.167	0.134
7	Stall torque	mNm	7.44	8.13	7.11	8.58	9.25	8.35	9.03	10.1	10.5	10.4	10.5	10.4	11.1	11	10.9
8	Stall current	A	3.46	3.51	2.69	2.73	2.33	1.87	1.82	1.69	1.52	1.25	1.03	0.814	0.809	0.688	0.556
9	Max. efficiency	%	50	53	53	57	60	60	61	63	64	65	65	66	66	66	66
	Characteristics																
10	Terminal resistance	Ω	0.867	1.02	1.34	1.76	2.57	3.21	3.96	5.32	6.6	9.56	14.6	22.1	26	34.9	54
11	Terminal inductance	mH	0.021	0.025	0.032	0.046	0.073	0.092	0.114	0.164	0.223	0.316	0.486	0.75	0.871	1.19	1.79
12	Torque constant	mNm/A	2.15	2.31	2.65	3.14	3.97	4.46	4.96	5.95	6.94	8.27	10.2	12.7	13.7	16	19.7
13	Speed constant	rpm/V	4440	4130	3610	3040	2410	2140	1930	1600	1380	1160	932	750	696	595	485
14	Speed / torque gradient	rpm/mNm	1790	1830	1830	1700	1560	1540	1540	1430	1310	1340	1330	1300	1320	1300	1330
15	Mechanical time constant	ms	12.8	11.4	10.5	9.44	8.68	8.46	8.23	7.93	7.74	7.62	7.51	7.42	7.39	7.37	7.38
16	Rotor inertia	gcm^2	0.681	0.596	0.548	0.53	0.53	0.526	0.512	0.528	0.565	0.545	0.541	0.544	0.536	0.543	0.529

Specifications

Thermal data

17	Thermal resistance housing-ambient	33 K/W
18	Thermal resistance winding-housing	7.0 K/W
19	Thermal time constant winding	4.88 s
20	Thermal time constant motor	259 s
21	Ambient temperature	-20…+65°C
22	Max. winding temperature	+85°C

Mechanical data (sleeve bearings)

23	Max. speed	16000 rpm
24	Axial play	0.05 - 0.15 mm
25	Radial play	0.014 mm
26	Max. axial load (dynamic)	0.8 N
27	Max. force for press fits (static)	15 N
	(static, shaft supported)	95 N
28	Max. radial load, 5 mm from flange	1.4 N

Other specifications

29	Number of pole pairs	1
30	Number of commutator segments	7
31	Weight of motor	27 g

Values listed in the table are nominal.
Explanation of the figures on page 68.

Operating Range

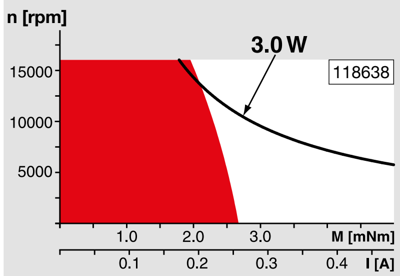

Comments

Continuous operation
In observation of above listed thermal resistance (lines 17 and 18) the maximum permissible winding temperature will be reached during continuous operation at 25°C ambient.
= Thermal limit.

Short term operation
The motor may be briefly overloaded (recurring).

Assigned power rating

maxon Modular System

Details on catalog page 32

Planetary Gearhead
∅13 mm
0.05 - 0.15 Nm
Page 328

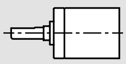

Planetary Gearhead
∅13 mm
0.2 - 0.35 Nm
Page 329

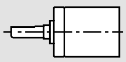

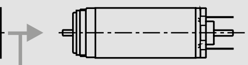

Recommended Electronics:

Notes	Page 32
ESCON Module 24/2	454
ESCON 36/2 DC	454
ESCON Module 50/5	455
ESCON 50/5	457
EPOS4 Mod./Comp. 24/1.5	462
MAXPOS 50/5	473

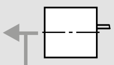

Encoder MEnc
∅13 mm
16 CPT, 2 channels
Page 416

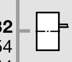

Encoder MR
16 CPT,
2 channels
Page 426

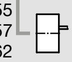

Encoder MR
64 - 256 CPT,
2 channels
Page 427/428

maxon gear

Planetary Gearhead GP 32 C ∅32 mm, 1.0–6.0 Nm

Ceramic Version

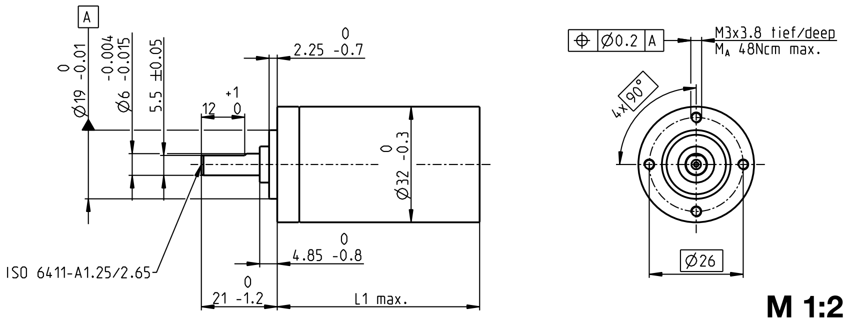

M 1:2

Technical Data

Planetary Gearhead	straight teeth
Output shaft	stainless steel
Shaft diameter as option	8 mm
Bearing at output	ball bearing
Radial play, 5 mm from flange	max. 0.14 mm
Axial play	max. 0.4 mm
Max. axial load (dynamic)	120 N
Max. force for press fits	120 N
Direction of rotation, drive to output	=
Max. continuous input speed	8000 rpm
Recommended temperature range	-40…+100°C
Number of stages	1 2 3 4 5
Max. radial load, 10 mm from flange	90 N 140 N 200 N 220 N 220 N

Option: Low-noise version

Stock program
Standard program
Special program (on request)

Part Numbers		166930	166933	166938	166939	166944	166949	166954	166959	166962	166967	166972	166977
Gearhead Data													
1 Reduction		3.7 : 1	14 : 1	33 : 1	51 : 1	111 : 1	246 : 1	492 : 1	762 : 1	1181 : 1	1972 : 1	2829 : 1	4380 : 1
2 Absolute reduction		26/7	676/49	529/16	17576/343	13824/125	421824/1715	86112/175	19044/25	10123776/8575	8626176/4375	495144/175	109503/25
3 Max. motor shaft diameter	mm	6	6	3	6	4	4	3	3	4	4	3	3
Part Numbers		166931	166934		166940	166945	166950	166955	166960	166963	166968	166973	166978
1 Reduction		4.8 : 1	18 : 1		66 : 1	123 : 1	295 : 1	531 : 1	913 : 1	1414 : 1	2189 : 1	3052 : 1	5247 : 1
2 Absolute reduction		24/5	624/35		16224/245	6877/56	101062/343	331776/625	36501/40	2425488/1715	536406/245	1907712/625	839523/160
3 Max. motor shaft diameter	mm	4	4		4	3	3	4	3	3	3	3	3
Part Numbers		166932	166935		166941	166946	166951	166956	166961	166964	166969	166974	166979
1 Reduction		5.8 : 1	21 : 1		79 : 1	132 : 1	318 : 1	589 : 1	1093 : 1	1526 : 1	2362 : 1	3389 : 1	6285 : 1
2 Absolute reduction		23/4	299/14		3887/49	3312/25	389376/1225	20631/35	279841/256	9345024/6125	2066688/875	474513/140	6436343/1024
3 Max. motor shaft diameter	mm	3	3		3	3	4	3	3	4	3	3	3
Part Numbers			166936		166942	166947	166952	166957		166965	166970	166975	
1 Reduction			23 : 1		86 : 1	159 : 1	411 : 1	636 : 1		1694 : 1	2548 : 1	3656 : 1	
2 Absolute reduction			576/25		14976/175	1587/10	359424/875	79488/125		1162213/686	7962624/3125	457056/125	
3 Max. motor shaft diameter	mm		4		4	3	4	3		3	4	3	
Part Numbers			166937		166943	166948	166953	166958		166966	166971	166976	
1 Reduction			28 : 1		103 : 1	190 : 1	456 : 1	706 : 1		1828 : 1	2623 : 1	4060 : 1	
2 Absolute reduction			138/5		3588/35	12167/64	89401/196	158171/224		2238912/1225	2056223/784	3637933/896	
3 Max. motor shaft diameter	mm		3		3	3	3	3		3	3	3	
4 Number of stages		1	2	2	3	3	4	4	4	5	5	5	5
5 Max. continuous torque	Nm	1	3	3	6	6	6	6	6	6	6	6	6
6 Max. intermittent torque at gear output	Nm	1.25	3.75	3.75	7.5	7.5	7.5	7.5	7.5	7.5	7.5	7.5	7.5
7 Max. efficiency	%	80	75	75	70	70	60	60	60	50	50	50	50
8 Weight	g	118	162	162	194	194	226	226	226	258	258	258	258
9 Average backlash no load	°	0.7	0.8	0.8	1.0	1.0	1.0	1.0	1.0	1.0	1.0	1.0	1.0
10 Mass inertia	gcm²	1.5	0.8	0.8	0.7	0.7	0.7	0.7	0.7	0.7	0.7	0.7	0.7
11 Gearhead length L1	mm	26.5	36.4	36.4	43.1	43.1	49.8	49.8	49.8	56.5	56.5	56.5	56.5

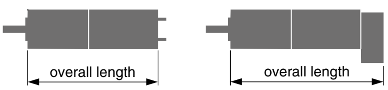

maxon Modular System

+ Motor	Page	+ Sensor/Brake	Page	Overall length [mm] = Motor length + gearhead length + (sensor/brake) + assembly parts											
RE 25, 10 W	125			81.1	91.0	91.0	97.7	97.7	104.4	104.4	104.4	111.1	111.1	111.1	111.1
RE 25, 10 W	125	MR	419	92.1	102.0	102.0	108.7	108.7	115.4	115.4	115.4	122.1	122.1	122.1	122.1
RE 25, 10 W	125	Enc 22	426	95.2	105.1	105.1	111.8	111.8	118.5	118.5	118.5	125.2	125.2	125.2	125.2
RE 25, 10 W	125	HED_5540	429/431	101.9	111.8	111.8	118.5	118.5	125.2	125.2	125.2	131.9	131.9	131.9	131.9
RE 25, 10 W	125	DCT 22	438	103.4	113.3	113.3	120.0	120.0	126.7	126.7	126.7	133.4	133.4	133.4	133.4
RE 25, 20 W	126			69.6	79.5	79.5	86.2	86.2	92.9	92.9	92.9	99.6	99.6	99.6	99.6
RE 25, 20 W	126	MR	419	80.6	90.5	90.5	97.2	97.2	103.9	103.9	103.9	110.6	110.6	110.6	110.6
RE 25, 20 W	126	HED_5540	430/433	90.4	100.3	100.3	107.0	107.0	113.7	113.7	113.7	120.4	120.4	120.4	120.4
RE 25, 20 W	126	DCT22	438	91.9	101.8	101.8	108.5	108.5	115.2	115.2	115.2	121.9	121.9	121.9	121.9
RE 25, 20 W	126	AB 28	480	103.7	113.6	113.6	120.3	120.3	127.0	127.0	127.0	133.7	133.7	133.7	133.7
RE 25, 20 W	126	HED_5540/AB 28	430/480	120.9	130.8	130.8	137.5	137.5	144.2	144.2	144.2	150.9	150.9	150.9	150.9
RE 25, 20 W	127	AB 28	480	115.2	125.1	125.1	131.8	131.8	138.5	138.5	138.5	145.2	145.2	145.2	145.2
RE 25, 20 W	127	HED_5540/AB 28	480	132.4	142.3	142.3	149.0	149.0	155.7	155.7	155.7	162.4	162.4	162.4	162.4
RE 30, 60 W	129			94.6	104.5	104.5	111.2	111.2	117.9	117.9	117.9	124.6	124.6	124.6	124.6
RE 30, 60 W	129	MR	420	106.0	115.9	115.9	122.6	122.6	129.3	129.3	129.3	136.0	136.0	136.0	136.0
RE 30, 60 W	129	HED_5540	429/431	115.4	125.3	125.3	132.0	132.0	138.7	138.7	138.7	145.4	145.4	145.4	145.4
RE 35, 90 W	130			97.6	107.5	107.5	114.2	114.2	120.9	120.9	120.9	127.6	127.6	127.6	127.6
RE 35, 90 W	130	MR	420	109.0	118.9	118.9	125.6	125.6	132.3	132.3	132.3	139.0	139.0	139.0	139.0
RE 35, 90 W	130	HED_5540	429/431	118.3	128.2	128.2	134.9	134.9	141.6	141.6	141.6	148.3	148.3	148.3	148.3
RE 35, 90 W	130	DCT 22	438	115.7	125.6	125.6	132.3	132.3	139.0	139.0	139.0	145.7	145.7	145.7	145.7
RE 35, 90 W	130	AB 28	480	133.7	143.6	143.6	150.3	150.3	157.0	157.0	157.0	163.7	163.7	163.7	163.7
RE 35, 90 W	130	HEDS 5540/AB 28	429/480	150.9	160.8	160.8	167.5	167.5	174.2	174.2	174.2	180.9	180.9	180.9	180.9
A-max 26	151-158			71.3	81.2	81.2	87.9	87.9	94.6	94.6	94.6	101.3	101.3	101.3	101.3
A-max 26	152-158	MEnc 13	408	78.4	88.3	88.3	95.0	95.0	101.7	101.7	101.7	108.4	108.4	108.4	108.4
A-max 26	152-158	MR	419	80.1	90.0	90.0	96.7	96.7	103.4	103.4	103.4	110.1	110.1	110.1	110.1
A-max 26	152-158	Enc 22	426	85.7	95.6	95.6	102.3	102.3	109.0	109.0	109.0	115.7	115.7	115.7	115.7
A-max 26	152-158	HED_5540	430/432	89.7	99.6	99.6	106.3	106.3	113.0	113.0	113.0	119.7	119.7	119.7	119.7
A-max 32	159/161			89.5	99.4	99.4	106.1	106.1	112.8	112.8	112.8	119.5	119.5	119.5	119.5
A-max 32	160/162			88.1	98.0	98.0	104.7	104.7	111.4	111.4	111.4	118.1	118.1	118.1	118.1
A-max 32	160/162	MR	420	99.3	109.2	109.2	115.9	115.9	122.6	122.6	122.6	129.3	129.3	129.3	129.3
A-max 32	160/162	HED_5540	430/432	108.9	118.8	118.8	125.5	125.5	132.2	132.2	132.2	138.9	138.9	138.9	138.9

Planetary Gearhead GP 22 C ⌀22 mm, 0.5–2.0 Nm

Ceramic Version

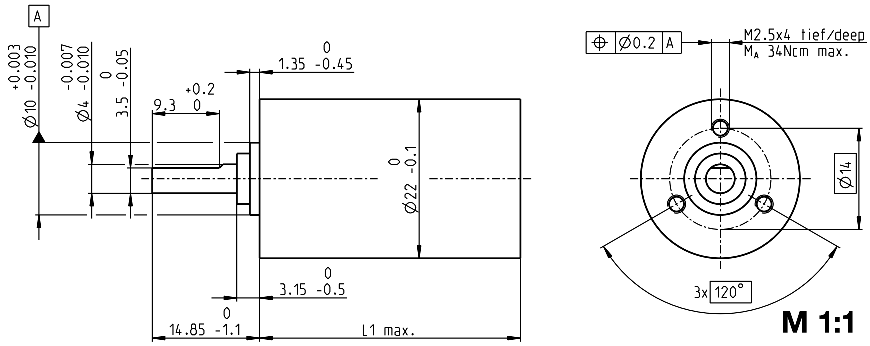

Technical Data

Planetary Gearhead	straight teeth
Output shaft	stainless steel, hardened
Bearing at output	ball bearing
Radial play, 10 mm from flange	max. 0.2 mm
Axial play	max. 0.2 mm
Max. axial load (dynamic)	100 N
Max. force for press fits	100 N
Direction of rotation, drive to output	=
Max. continuous input speed	8000 rpm
Recommended temperature range	-40…+100°C
Number of stages	1 2 3 4 5
Max. radial load, 10 mm from flange	30 N 50 N 55 N 55 N 55 N

maxon gear

Stock program
Standard program
Special program (on request)

	Gearhead Data		Part Numbers										
			143971	143974	143980	143986	143990	143996	144002	144004	144011	144017	144023
1	Reduction		3.8 : 1	14 : 1	53 : 1	104 : 1	198 : 1	370 : 1	590 : 1	742 : 1	1386 : 1	1996 : 1	3189 : 1
2	Absolute reduction		15/4	225/16	3375/64	87723/845	50625/256	10556001/28561	59049/100	759375/1024	158340015/114244	285012027/142805	1594323/500
3	Max. motor shaft diameter	mm	4	4	4	3.2	4	3.2	4	4	3.2	3.2	4
	Part Numbers		143972	143975	143981	143987	143991	143997	144003	144006	144012	144018	144024
1	Reduction		4.4 : 1	16 : 1	62 : 1	109 : 1	231 : 1	389 : 1	690 : 1	867 : 1	1460 : 1	2102 : 1	3728 : 1
2	Absolute reduction		57/13	855/52	12825/208	2187/20	192375/832	263169/676	1121931/1625	2885625/3328	3947535/2704	7105563/3380	30292137/8125
3	Max. motor shaft diameter	mm	3.2	3.2	3.2	4	3.2	3.2	3.2	3.2	3.2	3.2	3.2
	Part Numbers		143973	143976	143982	143988	143992	143998	144005	144007	144013	144019	144025
1	Reduction		5.4 : 1	19 : 1	72 : 1	128 : 1	270 : 1	410 : 1	850 : 1	1014 : 1	1538 : 1	2214 : 1	4592 : 1
2	Absolute reduction		27/5	3249/169	48735/676	41553/325	731025/2704	6561/16	531441/625	10965375/10816	98415/64	177147/80	14348907/3125
3	Max. motor shaft diameter	mm	2.5	3.2	3.2	3.2	3.2	4	2.5	3.2	4	4	2.5
	Part Numbers			143977	143983	143989	143993	143999		144008	144014	144020	
1	Reduction			20 : 1	76 : 1	157 : 1	285 : 1	455 : 1		1068 : 1	1621 : 1	2458 : 1	
2	Absolute reduction			81/4	1215/16	19683/125	18225/64	5000211/10985		273375/256	601692057/371293	135005697/54925	
3	Max. motor shaft diameter	mm		4	4	2.5	4	3.2		4	3.2	3.2	
	Part Numbers			143978	143984		143994	144000		144009	144015	144021	
1	Reduction			24 : 1	84 : 1		316 : 1	479 : 1		1185 : 1	1707 : 1	2589 : 1	
2	Absolute reduction			1539/65	185193/2197		2777895/8788	124659/260		41668425/35152	15000633/8788	3365793/1300	
3	Max. motor shaft diameter	mm		3.2	3.2		3.2	3.2		3.2	3.2	3.2	
	Part Numbers			143979	143985		143995	144001		144010	144016	144022	
1	Reduction			29 : 1	89 : 1		333 : 1	561 : 1		1249 : 1	1798 : 1	3027 : 1	
2	Absolute reduction			729/25	4617/52		69255/208	2368521/4225		1038825/832	373977/208	63950067/21125	
3	Max. motor shaft diameter	mm		2.5	3.2		3.2	3.2		3.2	3.2	3.2	
4	Number of stages		1	2	3	3	4	4	4	5	5	5	5
5	Max. continuous torque	Nm	0.5	0.6	1.2	1.2	1.8	1.8	1.8	2.0	2.0	2.0	2.0
6	Max. intermittent torque at gear output	Nm	0.8	0.9	1.9	1.9	2.7	2.7	2.7	3.0	3.0	3.0	3.0
7	Max. efficiency	%	84	70	59	59	49	49	49	42	42	42	42
8	Weight	g	42	55	68	68	81	81	81	94	94	94	94
9	Average backlash no load	°	1.0	1.2	1.6	1.6	2.0	2.0	2.0	2.0	2.0	2.0	2.0
10	Mass inertia	gcm²	0.5	0.4	0.4	0.4	0.4	0.4	0.4	0.4	0.4	0.4	0.4
11	Gearhead length L1*	mm	25.4	32.2	39.0	39.0	45.8	45.8	45.8	52.6	52.6	52.6	52.6

*L1 is–2.8 mm for calculating the overall length

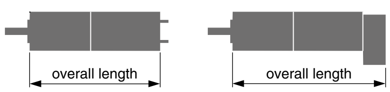

maxon Modular System

+ Motor	Page	+ Sensor/Brake	Page	Overall length [mm] = Motor length + gearhead length + (sensor/brake) + assembly parts										
A-max 19	143/144			51.6	58.4	65.2	65.2	72.0	72.0	72.0	78.8	78.8	78.8	78.8
A-max 19, 1.5 W	144	MR	416/417	56.7	63.5	70.3	70.3	77.1	77.1	77.1	83.9	83.9	83.9	83.9
A-max 19, 1.5 W	144	Enc 22	426	66.0	72.8	79.6	79.6	86.4	86.4	86.4	93.2	93.2	93.2	93.2
A-max 19, 1.5 W	144	MEnc 13	407	59.1	65.9	72.7	72.7	79.5	79.5	79.5	86.3	86.3	86.3	86.3
A-max 19, 2.5 W	145/146			54.2	61.0	67.8	67.8	74.6	74.6	74.6	81.4	81.4	81.4	81.4
A-max 19, 2.5 W	146	MR	416/417	58.5	65.3	72.1	72.1	78.9	78.9	78.9	85.7	85.7	85.7	85.7
A-max 19, 2.5 W	146	Enc 22	426	68.6	75.4	82.2	82.2	89.0	89.0	89.0	95.8	95.8	95.8	95.8
A-max 19, 2.5 W	146	MEnc 13	407	61.7	68.5	75.3	75.3	82.1	82.1	82.1	88.9	88.9	88.9	88.9
A-max 22	147-150			54.6	61.4	68.2	68.2	75.0	75.0	75.0	81.8	81.8	81.8	81.8
A-max 22	148/150	MR	416/417	59.6	66.4	73.2	73.2	80.0	80.0	80.0	86.8	86.8	86.8	86.8
A-max 22	148/150	Enc 22	426	69.0	75.8	82.6	82.6	89.4	89.4	89.4	96.2	96.2	96.2	96.2
A-max 22	148/150	MEnc 13	407	61.7	68.5	75.3	75.3	82.1	82.1	82.1	88.9	88.9	88.9	88.9

Planetary Gearhead GP 13 A ∅13 mm, 0.2–0.35 Nm

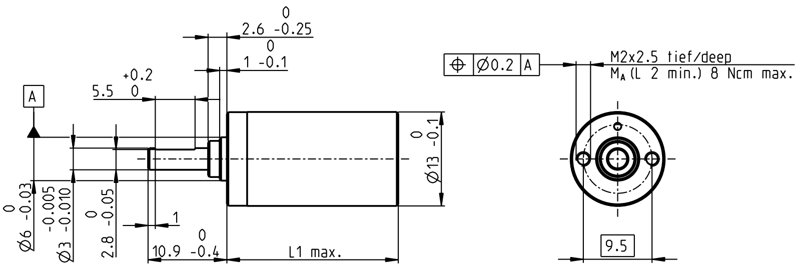

M 1:1

maxon gear

Technical Data

Planetary Gearhead	straight teeth
Output shaft	stainless steel, hardened
Bearing at output	sleeve bearing
Radial play, 6 mm from flange	max. 0.055 mm
Axial play	0.02–0.10 mm
Max. axial load (dynamic)	8 N
Max. force for press fits	100 N
Direction of rotation, drive to output	=
Max. continuous input speed	8000 rpm
Recommended temperature range	-40…+100°C
Number of stages	1 2 3 4 5
Max. radial load, 6 mm from flange	8 N 12 N 16 N 20 N 20 N

Stock program
Standard program
Special program (on request)

			Part Numbers				
			110313	110314	110315	110316	110317
Gearhead Data							
1	Reduction		4.1 : 1	17 : 1	67 : 1	275 : 1	1119 : 1
2	Absolute reduction		57/14	3249/196	185193/2744	10556001/38416	601692057/537824
3	Max. motor shaft diameter	mm	1.5	1.5	1.5	1.5	1.5
	Part Numbers		352365	352366	352367	352368	352369
1	Reduction		5.1 : 1	26 : 1	131 : 1	664 : 1	3373 : 1
2	Absolute reduction		66/13	4356/169	287496/2197	18974736/28561	1252332576/371293
3	Max. motor shaft diameter	mm	1.5	1.5	1.5	1.5	1.5
4	Number of stages		1	2	3	4	5
5	Max. continuous torque	Nm	0.20	0.20	0.30	0.30	0.35
6	Max. intermittent torque at gear output	Nm	0.30	0.30	0.45	0.45	0.53
7	Max. efficiency	%	91	83	75	69	62
8	Weight	g	11	14	17	20	23
9	Average backlash no load	°	1.0	1.2	1.5	1.8	2.0
10	Mass inertia	gcm²	0.025	0.015	0.015	0.015	0.015
11	Gearhead length L1*	mm	16.0	19.9	23.7	27.6	31.4

* for A-max 12 is L1 + 0.3 mm

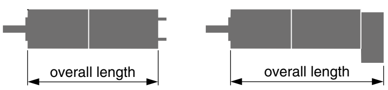

maxon Modular System

+ Motor	Page	+ Sensor/Brake	Page	Overall length [mm] = Motor length + gearhead length + (sensor/brake) + assembly parts				
RE 13	105/107			35.4	39.3	43.1	47.0	50.8
RE 13, 0.75 W	107	MR	413-415	42.5	46.4	50.2	54.1	57.9
RE 13, 0.75 W	107	MEnc 13	407	43.2	47.1	50.9	54.8	58.6
RE 13	109/111			47.6	51.5	55.3	59.2	63.0
RE 13, 2 W	111	MR	413-415	54.7	58.6	62.4	66.3	70.1
RE 13, 2 W	111	MEnc 13	407	55.4	59.3	63.1	67.0	70.8
RE 13, 1.5 W	113/115			38.5	42.4	46.2	50.1	53.9
RE 13, 1.5 W	115	MR	413-415	44.6	48.5	52.3	56.2	60.0
RE 13, 1.5 W	115	MEnc 13	407	46.5	50.4	54.2	58.1	61.9
RE 13, 3 W	117/119			50.7	54.6	58.4	62.3	66.1
RE 13, 3 W	119	MR	413-415	56.8	60.7	64.5	68.4	72.2
RE 13, 3 W	119	MEnc 13	407	58.7	62.6	66.4	70.3	74.1
A-max 12	137/138			37.6	41.5	45.3	49.2	53.0
A-max 12, 0.5 W	138	MR	413-415	41.7	45.6	49.4	53.3	57.1
EC 13, 6 W	208			37.4	41.3	45.1	49.0	52.8
EC 13, 12 W	209			49.6	53.5	57.3	61.2	65.0

Option Ball Bearing

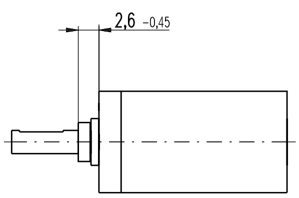

Gearhead length: L1 + 0.2 mm

Part Numbers

4.1 : 1	144300	131 : 1	352393
5.1 : 1	352391	275 : 1	144303
17 : 1	144301	664 : 1	352394
26 : 1	352392	1119 : 1	144304
67 : 1	144302	3373 : 1	352395

Technical Data

Planetary Gearhead	straight teeth
Output shaft	stainless steel, hardened
Bearing at output	preloaded ball bearings
Radial play, 6 mm from flange	max. 0.04 mm
Axial play at axial load	< 5 N 0 mm
	> 5 N max. 0.04 mm
Max. axial load (dynamic)	8 N
Max. force for press fits	25 N
Direction of rotation, drive to output	=
Max. continuous input speed	8000 rpm
Recommended temperature range	-40…+100°C
Number of stages	1 2 3 4 5
Max. radial load, 6 mm from flange	10 N 15 N 20 N 25 N 25 N

Gearhead values according to sleeve bearing version

Encoder MR Type L, 256–1024 CPT, 3 Channels, with Line Driver

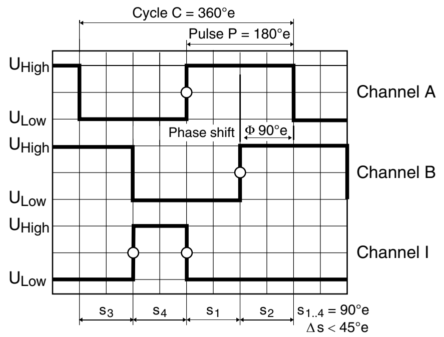

Direction of rotation cw (definition cw p. 60)

Stock program
Standard program
Special program (on request)

	Part Numbers				
	225783	228452	225785	228456	225787
Type					
Counts per turn	256	500	512	1000	1024
Number of channels	3	3	3	3	3
Max. operating frequency (kHz)	80	200	160	200	320
Max. speed (rpm)	18 750	24 000	18 750	12 000	18 750

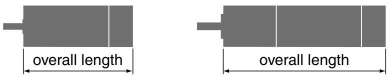

maxon Modular System

+ Motor	Page	+ Gearhead	Page	∅ Enc [mm]	Overall length [mm] / ● see Gearhead				
RE 30, 15 W	128			32	79.4	79.4	79.4	79.4	79.4
RE 30, 15 W	128	GP 32, 0.75 - 4.5 Nm	344	32	●	●	●	●	●
RE 30, 60 W	129			32	79.4	79.4	79.4	79.4	79.4
RE 30, 60 W	129	GP 32, 0.75 - 4.5 Nm	342	32	●	●	●	●	●
RE 30, 60 W	129	GP 32, 0.75 - 6.0 Nm	344-349	32	●	●	●	●	●
RE 30, 60 W	129	GP 32 S	374-379	32	●	●	●	●	●
RE 35, 90 W	130			32	82.4	82.4	82.4	82.4	82.4
RE 35, 90 W	130	GP 32, 0.75 - 4.5 Nm	342	32	●	●	●	●	●
RE 35, 90 W	130	GP 32, 0.75 - 6.0 Nm	344-349	32	●	●	●	●	●
RE 35, 90 W	130	GP 32, 4.0 - 8.0 Nm	350	32	●	●	●	●	●
RE 35, 90 W	130	GP 42, 3 - 15 Nm	354	32	●	●	●	●	●
RE 35, 90 W	130	GP 32 S	374-379	32	●	●	●	●	●
RE 40, 25 W	131			32	82.4	82.4	82.4	82.4	82.4
RE 40, 150 W	132			32	82.4	82.4	82.4	82.4	82.4
RE 40, 150 W	132	GP 42, 3 - 15 Nm	354	32	●	●	●	●	●
RE 40, 150 W	132	GP 52, 4 - 30 Nm	359	32	●	●	●	●	●
A-max 32	160/162			32	72.7	72.7	72.7	72.7	72.7
A-max 32	160/162	GP 32, 0.75 - 6.0 Nm	344-347	32	●	●	●	●	●
A-max 32	160/162	GS 38, 0.1 - 0.6 Nm	353	32	●	●	●	●	●
A-max 32	160/162	GP 32 S	374-379	32	●	●	●	●	●
EC-max 40, 70 W	226			31.8	73.9	73.9	73.9	73.9	73.9
EC-max 40, 70 W	226	GP 42, 3 - 15 Nm	355	31.8	●	●	●	●	●
EC-max 40, 120 W	227			31.8	103.9	103.9	103.9	103.9	103.9
EC-max 40, 120 W	227	GP 52, 4 - 30 Nm	360	31.8	●	●	●	●	●

Technical Data

Supply voltage V_{CC}	5 V ± 5%
Typical current draw	14 mA
Output signal	TTL compatible
Phase shift Φ	90°e ± 45°e
Index pulse width	90°e ± 45°e
Operating temperature range	-25…+85 °C
Moment of inertia of code wheel	≤ 1.7 gcm²
Output current per channel	max. 5 mA

The index signal I is synchronized with channel A or B.

Pin Allocation

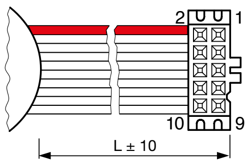

1 N.C.
2 V_{CC}
3 GND
4 N.C.
5 Channel $\bar{A}$
6 Channel A
7 Channel $\bar{B}$
8 Channel B
9 Channel $\bar{I}$ (Index)
10 Channel I (Index)

RE/A-max	L = 506
EC-max	L = 500

DIN Connector 41651/
EN 60603-13
flat band cable AWG 28

Connection example

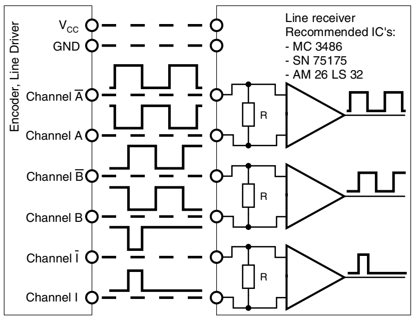

Opt. terminal resistance R > 1 kΩ

Encoder MR Type ML, 128–1000 CPT, 3 Channels, with Line Driver

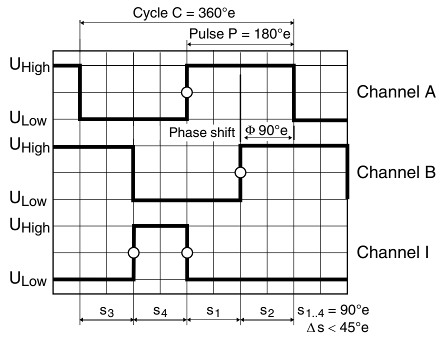

Direction of rotation cw (definition cw p. 60)

Stock program
Standard program
Special program (on request)

Part Numbers

Type	225771	225773	225778	225805	225780
Counts per turn	128	256	500	512	1000
Number of channels	3	3	3	3	3
Max. operating frequency (kHz)	80	160	200	320	200
Max. speed (rpm)	37 500	37 500	24 000	37 500	12 000

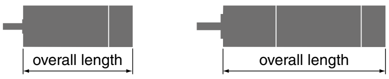

maxon Modular System

+ Motor	Page	+ Gearhead	Page	∅ Enc [mm]	Overall length [mm] / ● see Gearhead				
RE 25	125/127			25	65.5	65.5	65.5	65.5	65.5
RE 25	125/127	GP 26, 0.75 - 4.5 Nm	340	25	●	●	●	●	●
RE 25	125/127	GP 32, 0.75 - 6.0 Nm	342-347	25	●	●	●	●	●
RE 25	125/127	KD 32, 1.0 - 4.5 Nm	352	25	●	●	●	●	●
RE 25	125/127	GP 32 S	374-379	25	●	●	●	●	●
RE 25, 20 W	126			25	54.0	54.0	54.0	54.0	54.0
RE 25, 20 W	126	GP 22, 0.5 Nm	333	25	●	●	●	●	●
RE 25, 20 W	126	GP 26, 0.75 - 4.5 Nm	340	25	●	●	●	●	●
RE 25, 20 W	126	GP 32, 0.75 - 6.0 Nm	342-347	25	●	●	●	●	●
RE 25, 20 W	126	KD 32, 1.0 - 4.5 Nm	352	25	●	●	●	●	●
RE 25, 20 W	126	GP 32 S	374-379	25	●	●	●	●	●
A-max 26	152-158			25	53.5	53.5	53.5	53.5	53.5
A-max 26	152-158	GP 26, 0.75 - 4.5 Nm	340	25	●	●	●	●	●
A-max 26	152-158	GS 30, 0.07 - 0.2 Nm	341	25	●	●	●	●	●
A-max 26	152-158	GP 32, 0.75 - 6.0 Nm	342-347	25	●	●	●	●	●
A-max 26	152-158	GS 38, 0.1 - 0.6 Nm	353	25	●	●	●	●	●
A-max 26	152-158	GP 32 S	374-379	25	●	●	●	●	●
EC-max 30, 40 W	224			25			54.2		54.2
EC-max 30, 40 W	224	GP 32, 1 - 8.0 Nm	347/350	25			●		●
EC-max 30, 40 W	224	KD 32, 1.0 - 4.5 Nm	352	25			●		●
EC-max 30, 40 W	224	GP 32 S	374-379	25			●		●
EC-max 30, 60 W	225			25			76.2		76.2
EC-max 30, 60 W	225	GP 32, 1 - 8.0 Nm	347/350	25			●		●
EC-max 30, 60 W	225	KD 32, 1.0 - 4.5 Nm	352	25			●		●
EC-max 30, 60 W	225	GP 42, 3 - 15 Nm	355	25			●		●

Technical Data

Supply voltage V_{CC}	5 V ± 5%
Typical current draw	14 mA
Output signal	TTL compatible
Phase shift Φ	90°e ± 45°e
Index pulse width	90°e ± 45°e
Operating temperature range	-25…+85 °C
Moment of inertia of code wheel	≤ 0.7 gcm²
Output current per channel	max. 5 mA

The index signal I is synchronized with channel A or B.

Pin Allocation

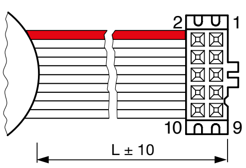

1 N.C.
2 V_{CC}
3 GND
4 N.C.
5 Channel $\bar{A}$
6 Channel A
7 Channel $\bar{B}$
8 Channel B
9 Channel $\bar{I}$ (Index)
10 Channel I (Index)

RE/A-max L = 506
EC-max L = 500

DIN Connector 41651/
EN 60603-13
flat band cable AWG 28

Connection example

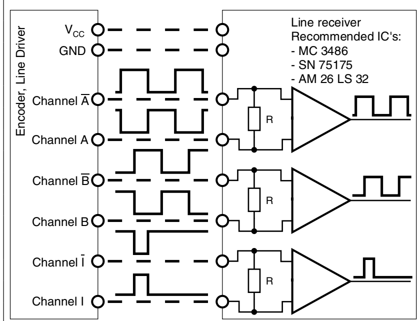

Opt. terminal resistance R > 1 kΩ

Encoder MR Type M, 128–512 CPT, 2/3 Channels, with Line Driver

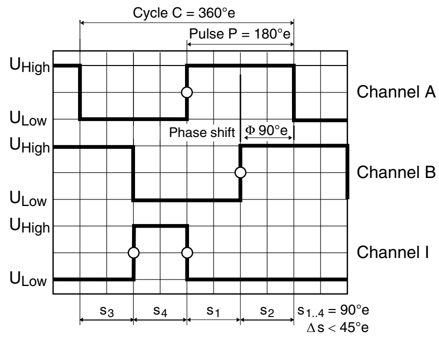

Direction of rotation cw (definition cw p. 60)

maxon sensor

- Stock program
- Standard program
- Special program (on request)

Part Numbers

	228179	228177	228181	228182	201937	201940
Type						
Counts per turn	128	128	256	256	512	512
Number of channels	2	3	2	3	2	3
Max. operating frequency (kHz)	80	80	160	160	320	320
Max. speed (rpm)	37 500	37 500	37 500	37 500	37 500	37 500

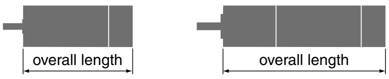

maxon Modular System

+ Motor	Page	+ Gearhead	Page	∅ Enc [mm]	Overall length [mm] / ● see Gearhead					
RE 16, 2 W	120			16	28.0	28.0	28.0	28.0	28.0	28.0
RE 16, 2 W	120	GP 16, 0.1 - 0.6 Nm	328/329	16	●	●	●	●	●	●
RE 16, 2 W	120	GP 16 S	369/370	16	●	●	●	●	●	●
RE 16, 3.2 W	122			16	45.4	45.4	45.4	45.4	45.4	45.4
RE 16, 3.2 W	122	GP 16, 0.1 - 0.6 Nm	328/329	16	●	●	●	●	●	●
RE 16, 3.2 W	122	GP 16 S	369/370	16	●	●	●	●	●	●
RE 16, 4.5 W	124			16	48.4	48.4	48.4	48.4	48.4	48.4
RE 16, 4.5 W	124	GP 16, 0.1 - 0.6 Nm	328/329	16	●	●	●	●	●	●
RE 16, 4.5 W	124	GP 16 S	369/370	16	●	●	●	●	●	●
A-max 16	140/142			16	30.4	30.4	30.4	30.4	30.4	30.4
A-max 16	140/142	GS 16, 0.01 - 0.1 Nm	324-327	16	●	●	●	●	●	●
A-max 16	140/142	GP 16, 0.1 - 0.6 Nm	328/329	16	●	●	●	●	●	●
A-max 16	140/142	GP 16 S	369/370	16	●	●	●	●	●	●
A-max 19, 1.5 W	144			19	34.0	34.0	34.0	34.0	34.0	34.0
A-max 19, 1.5 W	144	GP 19, 0.1 - 0.3 Nm	330	19	●	●	●	●	●	●
A-max 19, 1.5 W	144	GP 22, 0.5 - 2.0 Nm	333/335	19	●	●	●	●	●	●
A-max 19, 1.5 W	144	GS 24, 0.1 Nm	339	19	●	●	●	●	●	●
A-max 19, 1.5 W	144	GP 22 S	372/373	19	●	●	●	●	●	●
A-max 19, 2.5 W	146			19	35.8	35.8	35.8	35.8	35.8	35.8
A-max 19, 2.5 W	146	GP 19, 0.1 - 0.3 Nm	330	19	●	●	●	●	●	●
A-max 19, 2.5 W	146	GP 22, 0.5 - 2.0 Nm	333/335	19	●	●	●	●	●	●
A-max 19, 2.5 W	146	GS 24, 0.1 Nm	339	19	●	●	●	●	●	●
A-max 19, 2.5 W	146	GP 22 S	372/373	19	●	●	●	●	●	●
A-max 22	148/150			22	36.9	36.9	36.9	36.9	36.9	36.9
A-max 22	148/150	GP 22, 0.1 - 0.6 Nm	331/332	22	●	●	●	●	●	●
A-max 22	148/150	GP 22, 0.5 - 2.0 Nm	333/335	22	●	●	●	●	●	●
A-max 22	148/150	GS 24, 0.1 Nm	339	22	●	●	●	●	●	●
A-max 22	148/150	GP 22 S	372/373	22	●	●	●	●	●	●

Technical Data

Supply voltage V_{CC}	5 V ± 5%
Typical current draw 2 channel	11 mA
Typical current draw 3 channel	14 mA
Output signal	TTL compatible
Phase shift Φ	90°e ± 45°e
Index pulse width	90°e ± 45°e
Operating temperature range	-25…+85 °C
Moment of inertia of code wheel	≤ 0.09 gcm²
Output current per channel	max. 5 mA

The index signal I is synchronized with channel A or B.

Pin Allocation

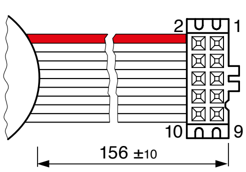

1 Motor +
2 V_{CC}
3 GND
4 Motor –
5 Channel $\bar{A}$
6 Channel A
7 Channel $\bar{B}$
8 Channel B
9* Channel $\bar{I}$ (Index)
10* Channel I (Index)

DIN Connector 41651/
EN 60603-13
flat band cable AWG 28
*version with 3 channels

Connection example

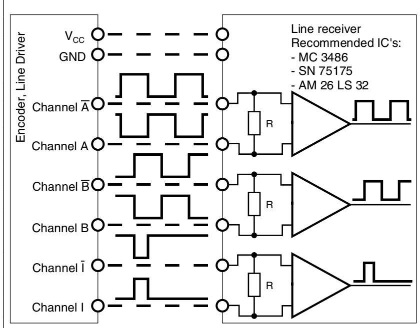

Opt. terminal resistance R > 1 kΩ

Encoder MR Type M, 128–512 CPT, 2/3 Channels, with Line Driver

maxon sensor

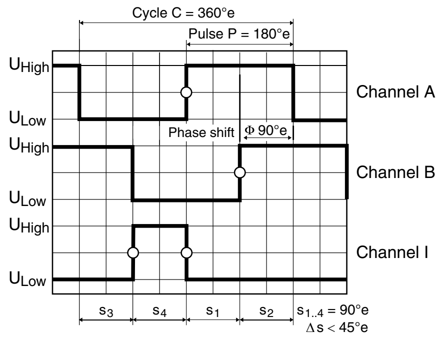

Direction of rotation cw (definition cw p. 60)

Stock program
Standard program
Special program (on request)

Part Numbers

	228179	228177	228181	228182	201937	201940
Type						
Counts per turn	128	128	256	256	512	512
Number of channels	2	3	2	3	2	3
Max. operating frequency (kHz)	80	80	160	160	320	320
Max. speed (rpm)	37 500	37 500	37 500	37 500	37 500	37 500

maxon Modular System

+ Motor	Page	+ Gearhead	Page	∅ Enc [mm]	Overall length [mm] / ● see Gearhead					
EC-max 16, 5 W	219			16	31.3	31.3	31.3	31.3	31.3	31.3
EC-max 16, 5 W	219	GP 16, 0.1 - 0.6 Nm	328/329	16	●	●	●	●	●	●
EC-max 16, 5 W	219	GP 16 S	369/370	16	●	●	●	●	●	●
EC-max 16, 8 W	221			16	43.3	43.3	43.3	43.3	43.3	43.3
EC-max 16, 8 W	221	GP 16, 0.2 - 0.6 Nm	329	16	●	●	●	●	●	●
EC-max 16, 8 W	221	GP 22, 0.5 - 2.0 Nm	336	16	●	●	●	●	●	●
EC-max 16, 8 W	221	GP 16 S/GP 22 S	369/373	16	●	●	●	●	●	●
EC-max 22, 12 W	222			16	41.7	41.7	41.7	41.7	41.7	41.7
EC-max 22, 12 W	222	GP 22, 0.5 - 2.0 Nm	336/337	16	●	●	●	●	●	●
EC-max 22, 12 W	222	KD 32, 1.0 - 4.5 Nm	352	16	●	●	●	●	●	●
EC-max 22, 12 W	222	GP 22 S	372/373	16	●	●	●	●	●	●
EC-max 22, 25 W	223			16	58.2	58.2	58.2	58.2	58.2	58.2
EC-max 22, 25 W	223	GP 22/GP 32	337/347	16	●	●	●	●	●	●
EC-max 22, 25 W	223	GP 32 S	374-379	16	●	●	●	●	●	●

Technical Data

Supply voltage V_{CC}	5 V ± 5%
Typical current draw 2 channel	11 mA
Typical current draw 3 channel	14 mA
Output signal	TTL compatible
Phase shift Φ	90°e ± 45°e
Index pulse width	90°e ± 45°e
Operating temperature range	-25…+85 °C
Moment of inertia of code wheel	≤ 0.09 gcm²
Output current per channel	max. 5 mA

The index signal I is synchronized with channel A or B.

Pin Allocation

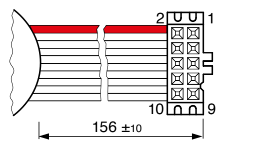

MR Encoder EC-max 16 / EC-max 22

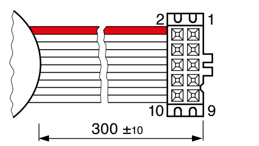

MR Encoder EC 16 / EC 22

1 N.C.
2 V_{CC}
3 GND
4 N.C.
5 Channel $\bar{A}$
6 Channel A
7 Channel $\bar{B}$
8 Channel B
9* Channel $\bar{I}$ (Index)
10* Channel I (Index)

DIN Connector 41651/
EN 60603-13
flat band cable AWG 28
*version with 3 channels

Connection example

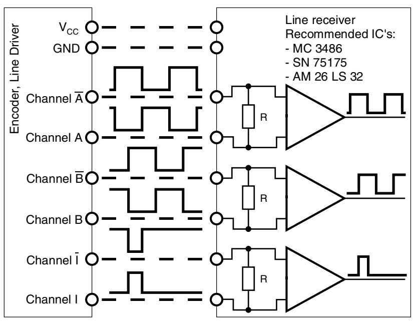

Opt. terminal resistance R > 1 kΩ

Encoder MR Type S, 64–256 CPT, 2 Channels, with Line Driver

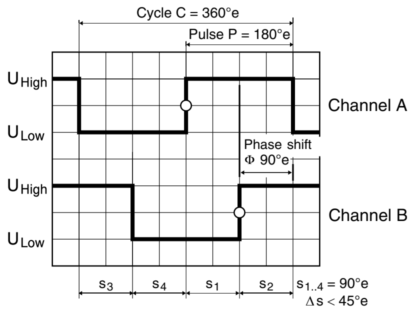

Direction of rotation cw (definition cw p. 60)

Stock program
Standard program
Special program (on request)

Part Numbers

Type	323049	323050	334910	323051	323052	323053	323054
Counts per turn	64	64	100	128	128	256	256
Number of channels	2	2	2	2	2	2	2
Max. operating frequency (kHz)	80	80	100	160	160	320	320
Max. speed (rpm)	75000	75000	60000	75000	75000	75000	75000

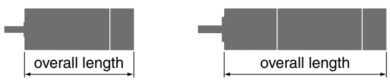

maxon Modular System

+ Motor	Page	+ Gearhead	Page	∅ Enc [mm]	Overall length [mm] / ● see Gearhead						
					323049	323050	334910	323051	323052	323053	323054
RE 8, 0.5 W, A	99			8			22.6				
RE 8, 0.5 W, A	99	GP 8, 0.01 - 0.1 Nm	318	8			●				
RE 8, 0.5 W, A	99	GP 8 S	367–368	8			●				
RE 10, 0.75 W	101			10	22.8			22.8		22.8	
RE 10, 0.75 W	101	GP 10, 0.005 - 0.15 Nm	319/320	10	●			●		●	
RE 10, 1.5 W	103			10	30.4			30.4		30.4	
RE 10, 1.5 W	103	GP 10, 0.005 - 0.15 Nm	319/320	10	●			●		●	
RE 13, 0.75 W	106			13		26.3			26.3		26.3
RE 13, 0.75 W	107			13		28.7			28.7		28.7
RE 13, 0.75 W	107	GP 13, 0.05 - 0.15 Nm	322	13		●			●		●
RE 13, 0.75 W	107	GP 13, 0.2 - 0.35 Nm	323	13		●			●		●
RE 13, 2 W	110			13		38.5			38.5		38.5
RE 13, 2 W	111			13		40.9			40.9		40.9
RE 13, 2 W	111	GP 13, 0.05 - 0.15 Nm	322	13		●			●		●
RE 13, 2 W	111	GP 13, 0.2 - 0.35 Nm	323	13		●			●		●
RE 13, 1.5 W	114			13		28.4			28.4		28.4
RE 13, 1.5 W	115			13		30.8			30.8		30.8
RE 13, 1.5 W	115	GP 13, 0.05 - 0.15 Nm	322	13		●			●		●
RE 13, 1.5 W	115	GP 13, 0.2 - 0.35 Nm	323	13		●			●		●
RE 13, 3 W	118			13		40.6			40.6		40.6
RE 13, 3 W	119			13		43.0			43.0		43.0
RE 13, 3 W	119	GP 13, 0.05 - 0.15 Nm	322	13		●			●		●
RE 13, 3 W	119	GP 13, 0.2 - 0.35 Nm	323	13		●			●		●
A-max 12, 0.5 W	138			12	25.3			25.3		25.3	
A-max 12, 0.5 W	138	GP 10, 0.01 - 0.15 Nm	320	12	●			●		●	
A-max 12, 0.5 W	138	GS 12, 0.01 - 0.03 Nm	321	12	●			●		●	
A-max 12, 0.5 W	138	GP 13, 0.05 - 0.15 Nm	322	12	●			●		●	
A-max 12, 0.5 W	138	GP 13, 0.2 - 0.35 Nm	323	12	●			●		●	

Technical Data

Supply voltage V_{CC}	5 V ± 5%
Typical current draw	11 mA
Output signal	TTL compatible
Phase shift Φ	90°e ± 45°e
Operating temperature range	-25…+85 °C
Moment of inertia of code wheel	≤ 0.005 gcm²
Output current per channel	max. 5 mA

Pin Allocation

Part Numbers 323049–323054
Pin 1–10 / X = 0.3 ±0.05 / Y = 11 –0.1 / L = 80 ±3
Compatible connector:
Molex 52207-1033, Tyco 1-84953-0
Pitch 1.0 mm, top contact style

1 Motor +
2 V_{CC}
3 GND
4 Motor –
5 Channel $\overline{A}$
6 Channel A
7 Channel $\overline{B}$
8 Channel B
9 N.C.
10 N.C.

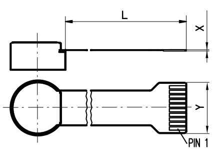

Part Numbers 334910
Pin 1–8 / X = 0.3 ±0.03 / Y = 4.5 ±0.07 / L = 84 ±3
Compatible connector:
Molex 52745-0833

1 Motor +
2 V_{CC}
3 GND
4 Motor –
5 Channel $\overline{A}$
6 Channel A
7 Channel $\overline{B}$
8 Channel B

Connection example

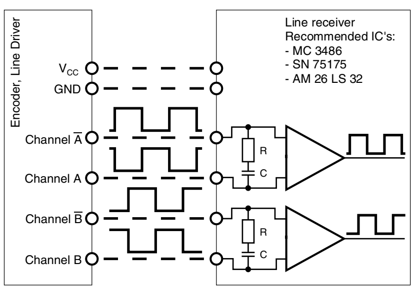

Terminal resistance R = typical 120 Ω
Capacitor C ≥ 0.1 nF per m line length

Appendix C

Visualization script

```
%% Initialize PERA
% Create the Link object , with the 3 joints from DH table
L(1) = Link('revolute','d',0,'a',0,'alpha',pi/2,'modified','offset',0) ;
L(2) = Link('revolute','d',-.32,'a',0,'alpha',-pi/2,'modified','offset',0) ;
L(3) = Link('revolute','d',0,'a',0,'alpha',pi/2,'modified','offset',-pi/2) ;

% Create homogeneous transformation matrix from final joint to end-effector
A34 = [1 0 0 12/25; 0 1 0 0; 0 0 1 0; 0 0 0 1];

% Create and plot PERA
PERA = SerialLink(L,'name','PERA');
PERA.tool = A34;
PERA.plotopt ={'workspace' , [-.5 .5 -.5 .5 -1.2 .5]} ; % Zero configuration
PERA.plot([0 0 0])
% PERA.plotopt ={'workspace' , [-.2 1 -.5 .5 -.6 .4]} ; % Example configuration ...
    (q1=20 deg; q3=70 deg)
% PERA.plot([(2*pi)/18 0 (7*pi)/18])
% PERA.teach

%% Desired circle trajectory simulation
traj = ct(.2,1,2);
figure(1)
PERA.plot(traj,'trail',{'r','LineWidth',1})

%% Simulated trajectory simulation
load('simulated_trajectory.mat', 'controller_trajectory_simulation')
q1 = controller_trajectory_simulation(2,1:10:end);
q2 = controller_trajectory_simulation(3,1:10:end);
q3 = controller_trajectory_simulation(4,1:10:end);
figure(2)
% PERA.plotopt ={'workspace' , [-.1 .8 -.4 .3 -.9 .1]} ;
PERA.plot([q1' q2' q3'],'trail',{'r','LineWidth',1})

%% Experimental trajectory simulation
% Data of the experiment is imported in columns via import button
q11 = q1(1:3:4002);
q21 = q2(1:3:4002);
q31 = q3(1:3:4002);

PERA.plot([q11 q21 q31],'trail',{'r','LineWidth',1})

%% Circle trajectory function
function circle_trajectory = ct(r,T,time)
% Draw a circle on a plane in the direction of Y
% Input: Radius of circle, Period for drawing a circle, Time duration in seconds
% Output: Trajectory planning for joints q1, q2, q3
t = 0:0.005:time;
s = length(t);
q1 = zeros(1,s);
q2 = asin(r/.48)*sin((2*pi/T)*t);
q3 = ones(1,s)*pi/2 - asin(r/.48)*cos((2*pi/T)*t);
circle_trajectory = [q1' q2' q3'];
end
```

Appendix D

Tuning script

```
%% Initialize
q1 = sym('q1','real');
q2 = sym('q2','real');
q3 = sym('q3','real');
q = [q1;q2;q3];
p1 = sym('p1','real');
p2 = sym('p2','real');
p3 = sym('p3','real');
p = [p1;p2;p3];
x1 = sym('x1','real');
x2 = sym('x2','real');
x3 = sym('x3','real');
x = [x1;x2;x3];

states=[q;p;x];

r1 = sym('r1','real');
r2 = sym('r2','real');
r3 = sym('r3','real');
R=diag([r1,r2,r3]);

k1 = sym('k1','real');
k2 = sym('k2','real');
k3 = sym('k3','real');
K=diag([k1,k2,k3]);

a1 = sym('a1','real');
a2 = sym('a2','real');
a3 = sym('a3','real');
a = [a1;a2;a3];

b1 = sym('b1','real');
b2 = sym('b2','real');
b3 = sym('b3','real');
b = [b1;b2;b3];

T=[(26843545600*5^(1/2))/(1509102191936324763648*sin(q1)^2 + ...
    110317174072316078125)^(1/2), 0, 0; 0, ...
    (26843545600*761603732984624577136 5^(1/2))/152320746596924915427 3, 0; ...
    -(26843545600*5^(1/2)*cos(q1))/(1619419366008640841773 - ...
    1509102191936324763648*cos(q1)^2)^(1/2), 0, (20*195^(1/2))/39];

f1=T*p;
f2=-transpose(T)*a.*tanh(b.*(q+x));
f3=-R*(a.*tanh(b.*(q+x))+K*x);

f=[f1;f2;f3];

A=[diff(f,q1),diff(f,q2),diff(f,q3),...
diff(f,p1),diff(f,p2),diff(f,p3),...
diff(f,x1),diff(f,x2),diff(f,x3)];


```

```
%% Trial and error substitution
% Substitute equilibrium
A1=subs(A,{q1 q2 q3 p1 p2 p3 x1 x2 x3},...
{0 0 0 0 0 0 0 0 0});

% Substitute gains
A2=subs(A1,{r1 r2 r3 k1 k2 k3 a1 a2 a3 b1 b2 b3},...
{0.0001 0.00001 0.055 10 20 100 11 2 6 120 100 120});

% Compute eigenvalues
e=vpa(real(eig(A2)),2);


%% Tuning loop
eigmax0=0;
eigmax1=0;
eigmax2=0;
eigmax3=0;
tuning1=zeros(3,1);
tuning2=zeros(3,1);
tuning3=zeros(3,1);
eig0=zeros(9,1); % Current eigenvalues
eig1=zeros(9,1); % Best eigenvalues
eig2=zeros(9,1); % Second best eigenvalues
eig3=zeros(9,1); % Third best eigenvalues
errors=0;
e = eig(A1)
fileID=fopen('myfile.txt','w');
% tic;
for i=[0.001:0.0005:0.011 0.02:0.0025:0.11 0.15:0.05:0.7]
    for j=[0.01:0.01:0.14 0.15:0.05:1.1 2:0.5:11 20:5:100]
        for k=[50:2:150]
            eig0=subs(e,{r1 r2 r3 k1 k2 k3 b1 b2 b3},{i i i j j j k k k});
            fprintf(fileID,'%6.3f\n',[i j k]);
            fprintf(fileID,'\n');
            try
                eigmax0=max(real(vpa(eig0,2)));
                eigmin0=min(real(vpa(eig0,2)));
                upperlimit=logical(eigmax0≤0);
                lowerlimit=logical(eigmin0>-20);
            catch
                fprintf('Failed for i=%6.3f, j=%6.3f, k=%6.3f\n',[i, j, k])
                errors=errors+1;
            end
            if upperlimit==1 && lowerlimit==1
                if eigmax0<eigmax1
                    eig3=eig2;
                    tuning3=tuning2;
                    eigmax3=eigmax2;
                    eig2=eig1;
                    tuning2=tuning1;
                    eigmax2=eigmax1;
                    eig1=eig0;
                    tuning1=[i;j;k];
                    eigmax1=eigmax0;
                    fprintf(fileID,'New best:\n');
                    fprintf(fileID,'%6.3f\n',tuning1);
                elseif eigmax0<eigmax2
                    eig3=eig2;
                    tuning3=tuning2;
                    eigmax3=eigmax2;
                    eig2=eig0;
                    tuning2=[i;j;k];
                    eigmax2=eigmax0;
                elseif eigmax0<eigmax3
                    eig3=eig0;
                    tuning3=[i;j;k];
                    eigmax3=eigmax0;
                end
            end
        end
    end
end
```

```
% toc
fprintf('There were %d errors\n',errors)
fprintf('The best solution was:\n')
vpa(eig1,2)
fprintf('With i=%6.3f, j=%6.3f, k=%6.3f\n',tuning1)
fprintf('The second best solution was:\n')
vpa(eig2,2)
fprintf('With i=%6.3f, j=%6.3f, k=%6.3f\n',tuning2)
fprintf('The third best solution was:\n')
vpa(eig3,2)
fprintf('With i=%6.3f, j=%6.3f, k=%6.3f\n',tuning3)

fclose(fileID);
```

Appendix E

Simulation model

The simulations were preformed in Simulink® using the fixed-step ode8 (Dormand-Prince) solver method with a step size of 0.005. This step size is chosen to match the sampling rate of the actual PERA control loop. The MATLAB® code in the function (`fcn`) block in the model is given below.

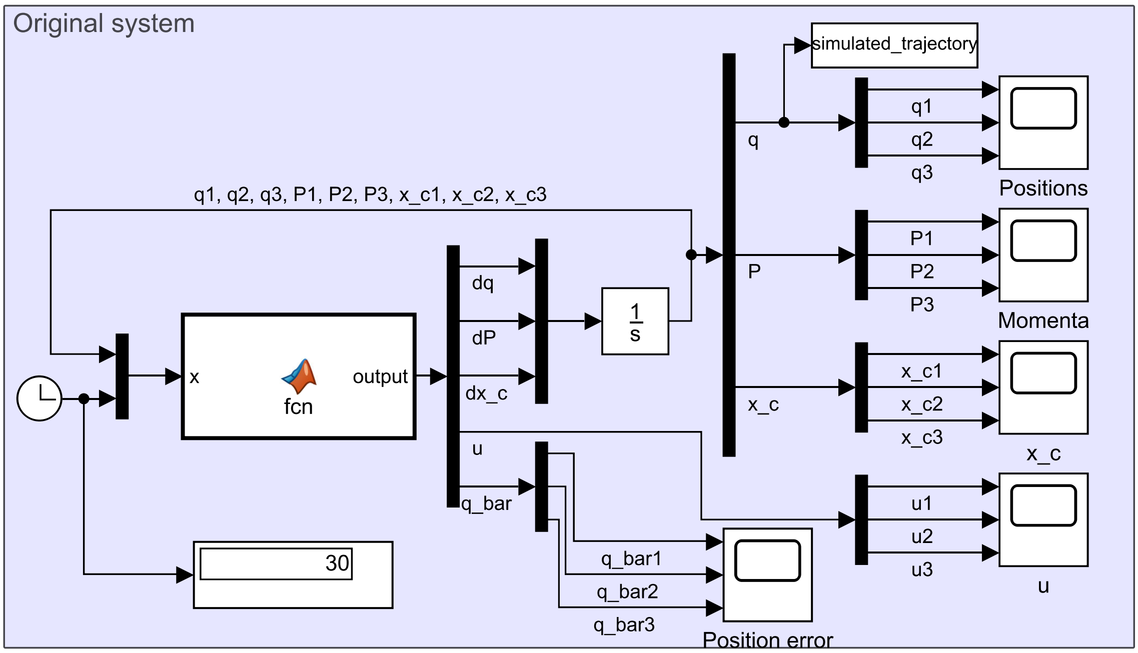

Figure E.1: Simulink® model used for simulations

```
function output = fcn(x)
q1 = x(1);
q2 = x(2);
q3 = x(3);
q = [q1; q2; q3]; % Joint positions
P1 = x(4);
P2 = x(5);
P3 = x(6);
P = [P1; P2; P3]; % Transformed momenta
x_c1 = x(7);
x_c2 = x(8);
x_c3 = x(9);
x_c = [x_c1; x_c2; x_c3]; % Artificial state
t = x(10);

% Trajectory: Circle parameters
r = .2; % Radius of circle in meters
T = 15; % Period for drawing a circle in seconds

```

```
% Trajectory: Desired positions
q_d1 = 0;
q_d2 = asin(r/.48)*sin((2*pi/T)*t);
q_d3 = pi/2 - asin(r/.48)*cos((2*pi/T)*t);
q_d = [q_d1; q_d2; q_d3];

% Trajectory: Derivative of desired positions
dq_d1 = 0;
dq_d2 = (2*pi*asin((25*r)/12)*cos((2*pi*t)/T))/T;
dq_d3 = (2*pi*asin((25*r)/12)*sin((2*pi*t)/T))/T;
dq_d = [dq_d1; dq_d2; dq_d3];

% Error positions
q_bar = q - q_d;

% Desired transformed momenta
P_d = [0; (2580715296368087*7616037329846245771365^(1/2)*pi*cos((2*pi*t)/15))...
/6044629098073145873530880000;...
(2580715296368087*195^(1/2)*pi*sin((2*pi*t)/15))/...
4503599627370496000];
% Derivative of desired transformed momenta
dP_d = [0; ...
-(2580715296368087*7616037329846245771365^(1/2)*pi^2*sin((2*pi*t)/15))/...
45334718235548594051481600000;...
(2580715296368087*195^(1/2)*pi^2*cos((2*pi*t)/15))/33776997205278720000];
% Error transformed momenta
P_bar = P - P_d;

% System matrices and gains
% Cholesky transform of the inertia matrix (Lower triangular, such that ...
    M^-1=T*T^T and P=T^T * p):
psi = [(26843545600*5^(1/2))/(1509102191936324763648*sin(q1)^2 + ...
    110317174072316078125)^(1/2), 0, 0; 0, ...
    (26843545600*7616037329846245771365^(1/2))/1523207465969249154273, 0; ...
    -(26843545600*5^(1/2)*cos(q1))/(1619419366008640841773 - ...
    1509102191936324763648*cos(q1)^2)^(1/2), 0, (20*195^(1/2))/39];
% Gyroscopic forces matrix
J2 = zeros(3,3);
alpha = [11;1.7;6]; % Chosen s.t. saturation limits cannot be exceeded
beta = [40; 30; 30];
K_c = diag([1 2 .1]);
R_c = diag([.4 .11 0.5]);

% Potential energies
dVdq = [6.17*sin(q1) + 1.57*cos(q3)*sin(q1) + 1.57*sin(q3)*cos(q1)*cos(q2); ...
    -1.57*sin(q3)*sin(q1)*sin(q2); 1.57*sin(q3)*cos(q1) + ...
    1.57*cos(q3)*cos(q2)*sin(q1)];
dV_ddq_d = [6.17*sin(q_d1) + 1.57*cos(q_d3)*sin(q_d1) + ...
    1.57*sin(q_d3)*cos(q_d1)*cos(q_d2); -1.57*sin(q_d3)*sin(q_d1)*sin(q_d2); ...
    1.57*sin(q_d3)*cos(q_d1) + 1.57*cos(q_d3)*cos(q_d2)*sin(q_d1)];

% Gradients of Hamiltonian
% H = 1/2*P_bar.'*P_bar + V(q)
dHdq = dVdq;
dHdP = P;

% Input
z = q_bar + x_c;
dphidz = [alpha(1)*tanh(beta(1)*z(1)); alpha(2)*tanh(beta(2)*z(2)); ...
    alpha(3)*tanh(beta(3)*z(3))];
u_bar = dVdq - dV_ddq_d - dphidz;
u_d = dV_ddq_d + (psi.')\dP_d;
u = u_bar + u_d;

% Time-derivatives of states
dq = psi*dHdP;
dP = (-psi.')*dHdq + J2*dHdP + (psi.')*u;
dx_c = -R_c*(K_c*x_c + dphidz);

% Output
output = [dq; dP; dx_c; u; q_bar];
```

Appendix F

Trajectory generation script

The 20th order polynomial approximations of the desired joint trajectories to let the end-effector of the PERA follow the shape of a lemniscate are given by

$$\begin{aligned}q_{d,1} =& 3.0 \cdot 10^{-16}t^{20} - 4.2 \cdot 10^{-14}t^{19} + 2.7 \cdot 10^{-12}t^{18} - 1.0 \cdot 10^{-10}t^{17} + 2.7 \cdot 10^{-9}t^{16} \\ & - 4.9 \cdot 10^{-8}t^{15} + 6.6 \cdot 10^{-7}t^{14} - 6.3 \cdot 10^{-6}t^{13} + 4.2 \cdot 10^{-5}t^{12} - 1.7 \cdot 10^{-4}t^{11} \\ & + 1.4 \cdot 10^{-4}t^{10} + 3.3 \cdot 10^{-3}t^{9} - 0.025t^{8} + 0.1t^{7} - 0.26t^{6} + 0.43t^{5} - 0.45t^{4} \\ & + 0.31t^{3} - 0.15t^{2} - 0.021t + 0.046\end{aligned}$$

$$\begin{aligned}q_{d,2} =& - 1.8 \cdot 10^{-15} * t^{20} + 2.7 \cdot 10^{-13} * t^{19} - 1.8 \cdot 10^{-11} * t^{18} + 7.5 \cdot 10^{-10} * t^{17} \\ & - 2.1 \cdot 10^{-8} * t^{16} + 4.3 \cdot 10^{-7} * t^{15} - 6.6 \cdot 10^{-6} * t^{14} + 7.6 \cdot 10^{-5} * t^{13} - 6.8 \cdot 10^{-4} * t^{12} \\ & + 4.7 \cdot 10^{-3} * t^{11} - 0.025 * t^{10} + 0.1 * t^{9} - 0.31 * t^{8} + 0.69 * t^{7} - 1.1 * t^{6} + 1.2 * t^{5} \\ & - 0.84 * t^{4} + 0.37 * t^{3} - 0.19 * t^{2} - 0.014 * t + 0.5\end{aligned}$$

$$\begin{aligned}q_{d,3} =& 2.2 \cdot 10^{-16} * t^{20} - 4.9 \cdot 10^{-14} * t^{19} + 4.6 \cdot 10^{-12} * t^{18} - 2.5 \cdot 10^{-10} * t^{17} + 8.9 \cdot 10^{-9} * t^{16} \\ & - 2.2 \cdot 10^{-7} * t^{15} + 4.2 \cdot 10^{-6} * t^{14} - 5.9 \cdot 10^{-5} * t^{13} + 6.3 \cdot 10^{-4} * t^{12} - 5.2 \cdot 10^{-3} * t^{11} \\ & + 0.033 * t^{10} - 0.16 * t^{9} + 0.6 * t^{8} - 1.6 * t^{7} + 3.3 * t^{6} - 4.6 * t^{5} + 4.4 * t^{4} - 2.7 * t^{3} \\ & + 0.87 * t^{2} + 0.16 * t + 1.4.\end{aligned}$$

Similarly, the polynomial approximations of the desired joint trajectories to let the end-effector of the PERA follow the shape of a heart are given by

$$\begin{aligned}q_{d,1} =& 8.9 \cdot 10^{-16} * t^{20} - 1.3 \cdot 10^{-13} * t^{19} + 9.3 \cdot 10^{-12} * t^{18} - 4.0 \cdot 10^{-10} * t^{17} + 1.2 \cdot 10^{-8} * t^{16} \\ & - 2.5 \cdot 10^{-7} * t^{15} + 4.0 \cdot 10^{-6} * t^{14} - 4.9 \cdot 10^{-5} * t^{13} + 4.7 \cdot 10^{-4} * t^{12} - 3.5 \cdot 10^{-3} * t^{11} \\ & + 0.021 * t^{10} - 0.093 * t^{9} + 0.32 * t^{8} - 0.84 * t^{7} + 1.6 * t^{6} - 2.2 * t^{5} + 2.0 * t^{4} - 1.1 * t^{3} \\ & + 0.22 * t^{2} - 0.042 * t + 0.19\end{aligned}$$

$$
\begin{aligned}
q_{d,2} =& 1.7 \cdot 10^{-19} * t^{20} + 1.1 \cdot 10^{-15} * t^{19} - 1.6 \cdot 10^{-13} * t^{18} + 1.1 \cdot 10^{-11} * t^{17} - 4.3 \cdot 10^{-10} * t^{16} \\
& + 1.2 \cdot 10^{-8} * t^{15} - 2.3 \cdot 10^{-7} * t^{14} + 3.2 \cdot 10^{-6} * t^{13} - 3.5 \cdot 10^{-5} * t^{12} + 2.9 \cdot 10^{-4} * t^{11} \\
& - 1.8 \cdot 10^{-3} * t^{10} + 8.2 \cdot 10^{-3} * t^{9} - 0.028 * t^{8} + 0.067 * t^{7} - 0.1 * t^{6} + 0.089 * t^{5} \\
& - 6.8 \cdot 10^{-4} * t^{4} - 0.085 * t^{3} + 0.024 * t^{2} - 5.0 \cdot 10^{-3} * t + 2.2 \cdot 10^{-4}
\end{aligned}
$$

$$
\begin{aligned}
q_{d,3} =& - 7.3 \cdot 10^{-16} * t^{20} + 1.1 \cdot 10^{-13} * t^{19} - 7.6 \cdot 10^{-12} * t^{18} + 3.2 \cdot 10^{-10} * t^{17} - 9.4 \cdot 10^{-9} * t^{16} \\
& + 2.0 \cdot 10^{-7} * t^{15} - 3.2 \cdot 10^{-6} * t^{14} + 3.9 \cdot 10^{-5} * t^{13} - 3.7 \cdot 10^{-4} * t^{12} + 2.7 \cdot 10^{-3} * t^{11} \\
& - 0.016 * t^{10} + 0.07 * t^{9} - 0.24 * t^{8} + 0.62 * t^{7} - 1.2 * t^{6} + 1.6 * t^{5} - 1.4 * t^{4} + 0.76 * t^{3} \\
& - 0.018 * t^{2} + 0.029 * t + 0.71.
\end{aligned}
$$

Because of the great length of the expressions for the desired input for both shapes, these expressions are not given here. The MATLAB® script used to define the trajectories is given below. Note that the scripts in Appendices C and E need to be ran prior to running this script, as the matrix Ψ (`T` in the script) and the `SerialLink` object that represents the PERA (`PERA`) are needed to compute the desired input and the inverse kinematics, respectively.

```matlab
%% Inverse kinematics to generate trajectory: lemniscate
t=0:0.005:15;
a=0.2;
L1=0.36;
L2=0.48;
r=0.2;
period=15;
x_lemniscate=zeros(length(t),1);
y_lemniscate=zeros(length(t),1);
z_lemniscate=zeros(length(t),1);
lemniscate_trajectory=zeros(length(t),3);
for i=1:length(t)
    x_lemniscate(i)=sqrt(L2^2-r^2);
    y_lemniscate(i)=0.8*(a*sqrt(2)*cos(((2*pi)/period)*t(i)))/(sin(((2*pi)/period)...
    *t(i))*sin(((2*pi)/period)*t(i))+1);
    z_lemniscate(i)=(a*sqrt(2)*cos(((2*pi)/period)*t(i))*sin(((2*pi)/period)*t(i)))...
    /(sin(((2*pi)/period)*t(i))*sin(((2*pi)/period)*t(i))+1)-L1;
    translation=transl(x_lemniscate(i),y_lemniscate(i),z_lemniscate(i));
    q = PERA.ikine(translation,'mask',[1 1 1 0 0 0]);
    lemniscate_trajectory(i,1)=q(1);
    lemniscate_trajectory(i,2)=q(2);
    lemniscate_trajectory(i,3)=q(3);
end

%% Inverse kinematics to generate trajectory: heart
t=0:0.1:15;
a=0.0125;
L1=0.36;
L2=0.48;
r=0.2;
period=15;
x_heart=zeros(length(t),1);
y_heart=zeros(length(t),1);
z_heart=zeros(length(t),1);
heart_trajectory=zeros(length(t),3);
for i=1:length(t)
    x_heart(i)=sqrt(L2^2-r^2);
    y_heart(i)=a*(16*(sin(((2*pi)/period)*(t(i)-7.5)))^3);
    z_heart(i)=a*(13*cos(((2*pi)/period)*(t(i)-7.5))-5*cos(((4*pi)/period)*(t(i)-7.5))...
    -2*cos(((6*pi)/period)*(t(i)-7.5))-cos(((8*pi)/period)*(t(i)-7.5)))-0.4;
    translation=transl(x_heart(i),y_heart(i),z_heart(i));
    q = PERA.ikine(translation,'mask',[1 1 1 0 0 0]);
    heart_trajectory(i,1)=q(1);
    heart_trajectory(i,2)=q(2);
    heart_trajectory(i,3)=q(3);
```

```
end

%% Plot: lemniscate
% PERA.plot(lemniscate_trajectory,'trail',{'r','LineWidth',1})

figure(5)
p_lemniscate1 = polyfit(t',lemniscate_trajectory(:,1),20);
plot(t,lemniscate_trajectory(:,1),'r')
hold on
plot(t, polyval(p_lemniscate1, t),'k')
title('q_1 (lemniscate trajectory)')
grid

figure(6)
p_lemniscate2 = polyfit(t',lemniscate_trajectory(:,2),20);
plot(t,lemniscate_trajectory(:,2),'m')
hold on
plot(t, polyval(p_lemniscate2, t),'k')
title('q_2 (lemniscate trajectory)')
grid

figure(7)
p_lemniscate3 = polyfit(t',lemniscate_trajectory(:,3),20);
plot(t,lemniscate_trajectory(:,3),'b')
hold on
plot(t, polyval(p_lemniscate3, t),'k')
title('q_3 (lemniscate trajectory)')
grid

%% Plot: heart
% PERA.plot(heart_trajectory,'trail',{'r','LineWidth',1})

figure(8)
p_heart1 = polyfit(t',heart_trajectory(:,1),20);
plot(t,heart_trajectory(:,1),'r')
hold on
plot(t, polyval(p_heart1, t),'k')
title('q_1 (heart trajectory)')
grid

figure(9)
p_heart2 = polyfit(t',heart_trajectory(:,2),20);
plot(t,heart_trajectory(:,2),'r')
hold on
plot(t, polyval(p_heart2, t),'k')
title('q_2 (heart trajectory)')
grid

figure(10)
p_heart3 = polyfit(t',heart_trajectory(:,3),20);
plot(t,heart_trajectory(:,3),'r')
hold on
plot(t, polyval(p_heart3, t),'k')
title('q_3 (heart trajectory)')
grid

%% u_d for all shapes
t = sym('t','real');
q_d1_lemniscate=0; q_d2_lemniscate=0; q_d3_lemniscate=0; q_d1_heart=0; ...
    q_d2_heart=0; q_d3_heart=0;
for i=1:21
    q_d1_lemniscate=q_d1_lemniscate + p_lemniscate1(i)*t^{(21-i);
    q_d2_lemniscate=q_d2_lemniscate + p_lemniscate2(i)*t^{(21-i);
    q_d3_lemniscate=q_d3_lemniscate + p_lemniscate3(i)*t^{(21-i);
    q_d1_heart=q_d1_heart + p_heart1(i)*t^{(21-i);
    q_d2_heart=q_d2_heart + p_heart2(i)*t^{(21-i);
    q_d3_heart=q_d3_heart + p_heart3(i)*t^{(21-i);
end
dq_d1_lemniscate = diff(q_d1_lemniscate,t);
dq_d2_lemniscate = diff(q_d2_lemniscate,t);
dq_d3_lemniscate = diff(q_d3_lemniscate,t);
dq_d_lemniscate = [dq_d1_lemniscate; dq_d2_lemniscate; dq_d3_lemniscate];
dq_d1_heart = diff(q_d1_heart,t);
```

```
dq_d2_heart = diff(q_d2_heart,t);
dq_d3_heart = diff(q_d3_heart,t);
dq_d_heart = [dq_d1_heart; dq_d2_heart; dq_d3_heart];

P_d_lemniscate = (subs(T, {q1, q2, q3}, {q_d1_lemniscate, q_d2_lemniscate, ...
    q_d3_lemniscate}))\dq_d_lemniscate;
dP_d_lemniscate = diff(P_d_lemniscate,t);
u_d_lemniscate = ((subs(T, {q1, q2, q3}, {q_d1_lemniscate, q_d2_lemniscate, ...
    q_d3_lemniscate})).')\dP_d_lemniscate;

P_d_heart = (subs(T, {q1, q2, q3}, {q_d1_heart, q_d2_heart, q_d3_heart}))\dq_d_heart;
dP_d_heart = diff(P_d_heart,t);
u_d_heart = ((subs(T, {q1, q2, q3}, {q_d1_heart, q_d2_heart, ...
    q_d3_heart})).')\dP_d_heart;
```

Appendix G

Model of the five degrees of freedom PERA

The elements of the inertia matrix of the five DoF PERA, i.e. $M(q) \in \mathbb{R}^{5\times 5}$, are given by

$$\begin{aligned}
m_{11} =& \mathcal{I}_{1,zz} + \mathcal{I}_{2,zz} + \mathcal{I}_{3,zz} + \mathcal{I}_{4,zz} + \mathcal{I}_{5,zz} + L_1^2 m_1 + L_1^2 m_2 + 2L_1^2 m_3 + 2L_2^2 m_3 - L_1^2 m_1 \cos^2(q_1) \\
& - L_1^2 m_2 \cos^2(q_1) - 2L_1^2 m_3 \cos^2(q_1) - 2L_2^2 m_3 \cos^2(q_2) + 4L_1 L_2 m_3 \cos(q_3) \\
& + 2L_2^2 m_3 \cos^2(q_1)\cos^2(q_2) - 2L_2^2 m_3 \cos^2(q_1)\cos^2(q_3) + 2L_2^2 m_3 \cos^2(q_2)\cos^2(q_3) \\
& - 2L_2^2 m_3 \cos^2(q_1)\cos^2(q_2)\cos^2(q_3) - 4L_1 L_2 m_3 \cos^2(q_1)\cos(q_3) \\
& + 4L_2^2 m_3 \cos(q_1)\cos(q_2)\cos(q_3)\sin(q_1)\sin(q_3) + 4L_1 L_2 m_3 \cos(q_1)\cos(q_2)\sin(q_1)\sin(q_3) \\
m_{12} =& -2L_2 m_3 \sin(q_2)(L_1 \cos(q_1)\sin(q_3) - L_2 \cos(q_2)\sin(q_1) + L_2 \cos(q_1)\cos(q_3)\sin(q_3) \\
& + L_2 \cos(q_2)\cos^2(q_3)\sin(q_1)) \\
m_{13} =& \mathcal{I}_{3,zz}\cos(q_1) + \mathcal{I}_{4,zz}\cos(q_1) + \mathcal{I}_{5,zz}\cos(q_1) + 2L_2^2 m_3 \cos(q_1) - 2L_2^2 m_3 \cos(q_1)\cos^2(q_3) \\
& + 2L_1 L_2 m_3 \cos(q_2)\sin(q_1)\sin(q_3) + 2L_2^2 m_3 \cos(q_2)\cos(q_3)\sin(q_1)\sin(q_3) \\
m_{14} =& \sin(q_1)\sin(q_2)(2m_3 L_2^2 + 2L_1 m_3 \cos(q_3) L_2 + \mathcal{I}_{4,zz} + \mathcal{I}_{5,zz}) \\
m_{15} =& \mathcal{I}_{5,zz}\sin(q_1)\sin(q_2) \\
m_{21} =& -2L_2 m_3 \sin(q_2)(L_1 \cos(q_1)\sin(q_3) - L_2 \cos(q_2)\sin(q_1) + L_2 \cos(q_1)\cos(q_3)\sin(q_3) \\
& + L_2 \cos(q_2)\cos^2(q_3)\sin(q_1)) \\
m_{22} =& \mathcal{I}_{2,zz} + \mathcal{I}_{3,zz} + \mathcal{I}_{4,zz} + \mathcal{I}_{5,zz} + L_1^2 m_1 + L_1^2 m_2 + 2L_1^2 m_3 + 2L_2^2 m_3 \cos^2(q_2) + 2L_2^2 m_3 \cos^2(q_3) \\
& + 4L_1 L_2 m_3 \cos(q_3) - 2L_2^2 m_3 \cos^2(q_2)\cos^2(q_3) \\
m_{23} =& -2L_2 m_3 \sin(q_2)\sin(q_3)(L_1 + L_2\cos(q_3)) \\
m_{24} =& \cos(q_2)(2m_3 L_2^2 + 2L_1 m_3 \cos(q_3) L_2 + \mathcal{I}_{4,zz} + \mathcal{I}_{5,zz}) \\
m_{25} =& \mathcal{I}_{5,zz}\cos(q_2) \\
m_{31} =& \mathcal{I}_{3,zz}\cos(q_1) + \mathcal{I}_{4,zz}\cos(q_1) + \mathcal{I}_{5,zz}\cos(q_1) + 2L_2^2 m_3 \cos(q_1) - 2L_2^2 m_3 \cos(q_1)\cos^2(q_3) \\
& + 2L_1 L_2 m_3 \cos(q_2)\sin(q_1)\sin(q_3) + 2L_2^2 m_3 \cos(q_2)\cos(q_3)\sin(q_1)\sin(q_3) \\
m_{32} =& -2L_2 m_3 \sin(q_2)\sin(q_3)(L_1 + L_2\cos(q_3)) \\
m_{33} =& \mathcal{I}_{3,zz} + \mathcal{I}_{4,zz} + \mathcal{I}_{5,zz} + 2L_2^2 m_3 \sin^2(q_3) \\
m_{34} =& 0 \\
m_{35} =& 0 \\
m_{41} =& \sin(q_1)\sin(q_2)(2m_3 L_2^2 + 2L_1 m_3 \cos(q_3) L_2 + \mathcal{I}_{4,zz} + \mathcal{I}_{5,zz}) \\
m_{42} =& \cos(q_2)(2m_3 L_2^2 + 2L_1 m_3 \cos(q_3) L_2 + \mathcal{I}_{4,zz} + \mathcal{I}_{5,zz}) \\
m_{43} =& 0
\end{aligned}$$

$$m_{44} = 2m_3 L_2^2 + \mathcal{I}_{4,zz} + \mathcal{I}_{5,zz}$$

$$m_{45} = \mathcal{I}_{5,zz}$$

$$m_{51} = \mathcal{I}_{5,zz} \sin(q_1)\sin(q_2)$$

$$m_{52} = \mathcal{I}_{5,zz} \cos(q_2)$$

$$m_{53} = 0$$

$$m_{54} = \mathcal{I}_{5,zz}$$

$$m_{55} = \mathcal{I}_{5,zz}$$

Substitution of parameters yields

$$\begin{aligned}
m_{11} =& 0.072\cos(q_3) - 0.42\cos^2(q_1) - 0.031\cos^2(q_2) - 0.072\cos^2(q_1)\cos(q_3) + 0.031\cos^2(q_1)\cos^2(q_2) \\
&- 0.031\cos^2(q_1)\cos^2(q_3) + 0.031\cos^2(q_2)\cos^2(q_3) - 0.031\cos^2(q_1)\cos^2(q_2)\cos^2(q_3) \\
&+ 0.072\cos^2(q_1)\cos(q_2)\sin(q_1)\sin(q_3) + 0.063\cos(q_1)\cos(q_2)\cos(q_3)\sin(q_1)\sin(q_3) + 0.49
\end{aligned}$$

$$\begin{aligned}
m_{12} =& -4.5 \cdot 10^{-3}\sin(q_2) * (8\cos(q_1)\sin(q_3) - 7\cos(q_2)\sin(q_1) + 7\cos(q_2)\cos^2(q_3)\sin(q_1) \\
&+ 7\cos(q_1)\cos(q_3)\sin(q_3))
\end{aligned}$$

$$\begin{aligned}
m_{13} =& 0.038\cos(q_1) - 0.031\cos(q_1)\cos^2(q_3) + 0.036\cos(q_2)\sin(q_1)\sin(q_3) \\
&+ 0.031\cos(q_2)\cos(q_3)\sin(q_1)\sin(q_3)
\end{aligned}$$

$$m_{14} = 6.9 \cdot 10^{-23}\sin(q_1)\sin(q_2) * (5.2 \cdot 10^{20}\cos(q_3) + 4.7 \cdot 10^{20})$$

$$m_{15} = 7.3 \cdot 10^{-4}\sin(q_1)\sin(q_2)$$

$$\begin{aligned}
m_{21} =& -4.5 \cdot 10^{-3}\sin(q_2) * (8\cos(q_1)\sin(q_3) - 7\cos(q_2)\sin(q_1) + 7\cos(q_2)\cos^2(q_3)\sin(q_1) \\
&+ 7\cos(q_1)\cos(q_3)\sin(q_3))
\end{aligned}$$

$$m_{22} = 0.072\cos(q_3) + 0.031\cos^2(q_2) + 0.031\cos^2(q_3) - 0.031\cos^2(q_2)\cos^2(q_3) + 0.43$$

$$m_{23} = -4.5 \cdot 10^{-3}\sin(q_2)\sin(q_3) * (7\cos(q_3) + 8)$$

$$m_{24} = 6.9 \cdot 10^{-23}\cos(q_2) * (5.2 \cdot 10^{20}\cos(q_3) + 4.7 \cdot 10^{20})$$

$$m_{25} = 7.3 \cdot 10^{-4}\cos(q_2)$$

$$\begin{aligned}
m_{31} =& 0.038\cos(q_1) - 0.031\cos(q_1)\cos^2(q_3) + 0.036\cos(q_2)\sin(q_1)\sin(q_3) \\
&+ 0.031\cos(q_2)\cos(q_3)\sin(q_1)\sin(q_3)
\end{aligned}$$

$$m_{32} = -4.5 \cdot 10^{-3}\sin(q_2)\sin(q_3) * (7\cos(q_3) + 8)$$

$$m_{33} = 0.031\sin^2(q_3) + 6.9 \cdot 10^{-3}$$

$$m_{34} = 0$$

$$m_{35} = 0$$

$$m_{41} = 6.9 \cdot 10^{-23}\sin(q_1)\sin(q_2) * (5.2 \cdot 10^{20}\cos(q_3) + 4.7 \cdot 10^{20})$$

$$m_{42} = 6.9 \cdot 10^{-23}\cos(q_2) * (5.2 \cdot 10^{20}\cos(q_3) + 4.7 \cdot 10^{20})$$

$$m_{43} = 0$$

$$m_{44} = 0.033$$

$$m_{45} = 7.3 \cdot 10^{-4}$$

$$m_{51} = 7.3 \cdot 10^{-4}\sin(q_1)\sin(q_2)$$

$$m_{52} = 7.3 \cdot 10^{-4}\cos(q_2)$$

$$m_{53} = 0$$

$$m_{54} = 7.3 \cdot 10^{-4}$$

$$m_{55} = 7.3 \cdot 10^{-4}$$

The elements of the vector of potential energies of the five DoF PERA, i.e. $\frac{\partial V(q)}{\partial q} \in \mathbb{R}^5$, are given by

$$\begin{aligned}
v_1 =& gm_2(L_1 \sin(q_1) - \frac{1}{3}L_2(-\cos(q_3)\sin(q_1) - \sin(q_3)\cos(q_1)\cos(q_2))) \\
& - gm_3(\frac{1}{3}L_3(\cos(q_5)(\sin(q_4)(\sin(q_3)\sin(q_1) - \cos(q_3)\cos(q_1)\cos(q_2)) + \cos(q_4)(-\cos(q_3)\sin(q_1) \\
& - \sin(q_3)\cos(q_1)\cos(q_2))) + \cos(q_1)\sin(q_2)\sin(q_5)) - L_1\sin(q_1) + L_2(-\cos(q_3)\sin(q_1) \\
& - \sin(q_3)\cos(q_1)\cos(q_2))) + \frac{1}{3}L_1 gm_1 \sin(q_1)
\end{aligned}$$

$$\begin{aligned}
v_2 =& - gm_3(\frac{1}{3}L_3(\cos(q_5)(\sin(q_3)\cos(q_4)\sin(q_1)\sin(q_2) + \cos(q_3)\sin(q_1)\sin(q_2)\sin(q_4)) \\
& + \cos(q_2)\sin(q_1)\sin(q_5)) + L_2\sin(q_3)\sin(q_1)\sin(q_2)) - \frac{1}{3}L_2 gm_2 \sin(q_3)\sin(q_1)\sin(q_2)
\end{aligned}$$

$$\begin{aligned}
v_3 =& gm_3(L_2(\sin(q_3)\cos(q_1) + \cos(q_3)\cos(q_2)\sin(q_1)) - \frac{1}{3}L_3\cos(q_5)(\sin(q_4)(-\cos(q_3)\cos(q_1) \\
& + \sin(q_3)\cos(q_2)\sin(q_1)) - \cos(q_4)(\sin(q_3)\cos(q_1) + \cos(q_3)\cos(q_2)\sin(q_1)))) \\
& + \frac{1}{3}L_2 gm_2(\sin(q_3)\cos(q_1) + \cos(q_3)\cos(q_2)\sin(q_1))
\end{aligned}$$

$$\begin{aligned}
v_4 =& - \frac{1}{3}L_3 gm_3 \cos(q_5)(\sin(q_4)(-\cos(q_3)\cos(q_1) + \sin(q_3)\cos(q_2)\sin(q_1)) - \cos(q_4)(\sin(q_3)\cos(q_1) \\
& + \cos(q_3)\cos(q_2)\sin(q_1)))
\end{aligned}$$

$$\begin{aligned}
v_5 =& - \frac{1}{3}L_3 gm_3(\sin(q_5)(\cos(q_4)(-\cos(q_3)\cos(q_1) + \sin(q_3)\cos(q_2)\sin(q_1)) + \sin(q_4)(\sin(q_3)\cos(q_1) \\
& + \cos(q_3)\cos(q_2)\sin(q_1))) + \cos(q_5)\sin(q_1)\sin(q_2))
\end{aligned}$$

Substitution of parameters yields

$$\begin{aligned}
v_1 =& 6.2\sin(q_1) - 0.13\cos(q_5)(\sin(q_4)(\sin(q_3)\sin(q_1) - \cos(q_3)\cos(q_1)\cos(q_2)) \\
& + \cos(q_4)(-\cos(q_3)\sin(q_1) - \sin(q_3)\cos(q_1)\cos(q_2))) - 1.3 - \cos(q_3)\sin(q_1) \\
& + 1.3\sin(q_3)\cos(q_1)\cos(q_2) - 0.13\cos(q_1)\sin(q_2)\sin(q_5)
\end{aligned}$$

$$\begin{aligned}
v_2 =& - 0.13\cos(q_5)(\sin(q_3)\cos(q_4)\sin(q_1)\sin(q_2) + \cos(q_3)\sin(q_1)\sin(q_2)\sin(q_4)) \\
& - 1.3\sin(q_3)\sin(q_1)\sin(q_2) - 0.13\cos(q_2)\sin(q_1)\sin(q_5)
\end{aligned}$$

$$\begin{aligned}
v_3 =& 1.3\sin(q_3)\cos(q_1) - 0.13\cos(q_5)(\sin(q_4)(-\cos(q_3)\cos(q_1) + \sin(q_3)\cos(q_2)\sin(q_1)) \\
& - \cos(q_4)(\sin(q_3)\cos(q_1) + \cos(q_3)\cos(q_2)\sin(q_1))) - 1.3 - \cos(q_3)\cos(q_2)\sin(q_1)
\end{aligned}$$

$$\begin{aligned}
v_4 =& - 0.13\cos(q_5)(\sin(q_4)(-\cos(q_3)\cos(q_1) + \sin(q_3)\cos(q_2)\sin(q_1)) - \cos(q_4)(\sin(q_3)\cos(q_1) \\
& + \cos(q_3)\cos(q_2)\sin(q_1)))
\end{aligned}$$

$$\begin{aligned}
v_5 =& - 0.13\sin(q_5)(\cos(q_4)(-\cos(q_3)\cos(q_1) + \sin(q_3)\cos(q_2)\sin(q_1)) + \sin(q_4)(\sin(q_3)\cos(q_1) \\
& + \cos(q_3)\cos(q_2)\sin(q_1))) - 0.13\cos(q_5)\sin(q_1)\sin(q_2)
\end{aligned}$$